CHAPTER 1

THESIS OVERVIEW

1.1 Background to the Research

Interaction of light with metal has been widely studied by scientists for many decades. Metal is recognized as a good conductor of heat and electricity due to the delocalization of valence electrons in metal. However, it could be a different story when the size of metal is reduced to less than or equal to the wavelength of light *(Matthew R. Jones et al., 2011; Stockman, 2011)*. In the 1800s, Michael Faraday initiated the first scientific investigation into the gold particle with a size less than the wavelength of light. He found that nano-sized gold particle was red in color, unlike the yellow color of bulk gold. Furthermore, color of the gold colloid can be changed when the size of particle is varied. In 1908, Gustav Mie took a step forward. He established an analytical solution to the equations for the metal sphere of arbitrary size. In this way, he could calculate the optical extinction spectra for metal colloid containing spherical particles of any size and unravel the red color mystery of Faraday's gold colloid. In particular, as the bulk metal is scaled down to *nano* dimensions, confinement effect of charge carrier and enhancement of surface to volume ratio is observed. A dramatic change in optical properties is resulted from the collective oscillation of the conduction electrons in nanosized metal *(A. Maier and A. Atwater 2005; Armelao et al., 2006)*. This phenomenon is called surface plasmon resonance (SPR) effect which can lead to the highest absorption of incident light at certain wavelength as a function of size, size distribution, and shape of metal nanoparticles (NPs). By tailoring these physical properties, position and intensity of SPR signal can be controlled in order to meet the needs of technological application. The details of the SPR phenomenon will be discussed in the next section.

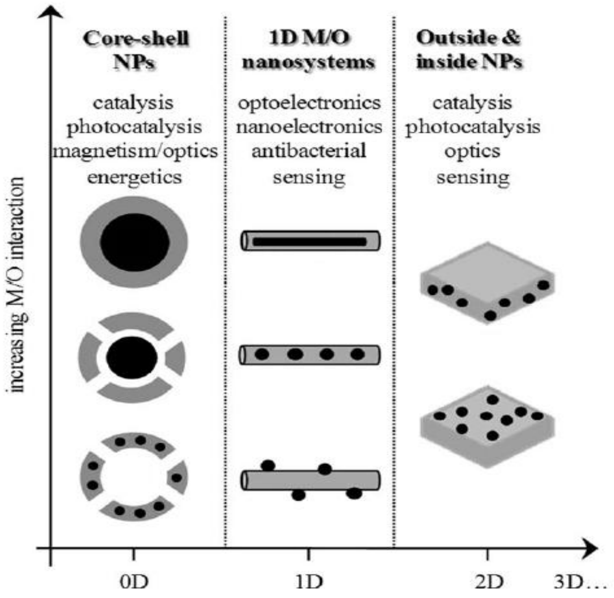

Figure 1.1: Schematic illustration of metal/oxide-based dielectric matrices in different dimension *(Davide Barreca et al. 2011).*

In recent years, there has been an exponential growth of scientific investigation on nanocomposite materials consisting of metal dispersed ON or embedded IN dielectric matrices *(Davide Barreca et al., 2011).* These materials can come in various geometries ranging from 0D- to 1D-, 2D- and 3D-structures as illustrated in Figure 1.1. Due to their fascinating and anomalous characteristics, different targeted functions have been aimed from metal/dielectric nanoscomposite materials such as catalysis, gas sensing, electronic devices, data storage, plasmonic solar cell and so on. This idea can be realized by carefully designing the experimental technique. For instance, nowadays, bottom-up chemical techniques are most widely utilized to prepare accurate size or shape of metal NPs dispersed ON or embedded IN dielectric matrices. Among various dielectric matrices, oxides matrices such as SiO_2, TiO_2 and Al_2O_3 are most favorable *(Armelao et al., 2006).* Thanks to their insulating character, thermal stability and weak interaction with the metal particles, many thorough investigations on these materials have been undertaken.

1.2 Research Problem and Motivations

In recent years, great interest has been focused on precise control of structural properties of metal NPs such as size, shape and size distribution. As mentioned above, chemical techniques such as electrochemical methods *(Yu-Ying Yu et al., 1997)*, self-assembling by metal NPs colloidal solutions *(Hammond, 2004)* and sol-gel method *(Innocenzi et al. 1996)* have been widely adopted to prepare arrays of accurate size metal NPs dispersed on dielectric matrices. Controlling the size or shape is usually done by adjusting the ratio of the concentration of the chemicals making the NPs to that of the selected capping materials *(El-Sayed , 2004)*. Such metal NPs with accurate size can be used as catalysts for the growth of nanowires or nanotubes with the desired diameter. The capping molecules or stabilizing ligands actually are the materials used to stabilize the surface of chemically prepared metal NPs in order to prevent the agglomeration of NPs *(Dae-Gun Kim et al., 2008)*. However, the disadvantages of stabilizers include the great impact on crystallographic phase, electronic structure, and optical properties of the NPs (*Balamurugan and Maruyama, 2005)*. The shape and peak position of SPR absorption peak induced by metal NPs can also be influenced. Even though the uses of chemically prepared metal NPs in important applications like biomolecular recognition and thiol-based bio-sensors in DNA chips cannot be denied *(Tokareva and Hutter, 2004),* it is important to understand the underlying physical significance of metal NPs without capping molecules and their implementation in other potential applications.

Therefore, the vapor deposition techniques such as chemical vapor deposition (CVD) and physical vapour deposition (PVD) technologies become the alternative way to prepare metal NPs with pure surface even though they have the limitation of small NPs size and spacing control. Examples of vapor deposition techniques include thermal evaporation, sputtering *(Xiuli Zhou et al., 2009)*, laser ablation *(Seung H. Ko et al., 2006)* and lithography *(Prashant K. Jain et al., 2007).* Among the advantages of this techniques include cost effective, simple to use and dry process compatible with most of the device technologies nowadays. Therefore, in this work, PVD and CVD techniques are adopted as the preparation methods for metal NPs dispersed on and embedded IN dielectric matrices. In addition, improvement on the size control of metal NPs by combining both techniques has become the motivation and challenge for this study.

1.3 Significance and Implications of the Research

The research presented in this thesis has significant implications for future practical applications. As highlighted by Harry Atwater (2011) in the *MRS Bulletin (Atwater, 2011)*, further advances in interdisciplinary research will rely on the interplay of fundamental insights about the physics of innovative materials synthesis. Therefore, there is a clear need for research on the precise control of the structural properties of metal NPs. To date, many researchers have studied the means to control the size and shape of metal NPs using bottom-up techniques since the SPR signal is greatly dependent on these structural properties of metal. However, further improvement on the synthesis techniques is always required. Even though this thesis does not give any results on the practical application part, it is hoped that this study will provide better insights into the means to control the structural properties of metal NPs. This can surely benefit those researchers who intend to further investigate NPs technology.

1.4 Structure of Thesis

A brief overview of the chapters follows the present chapter is given next.

Chapter 2

Chapter 2 outlines the literature review of this research. It starts with the background of the metal/dielectric nanocomposite film. The reason as to why the Au and SiO_x are selected as the candidate materials in this work will be discussed. Surface plasmon resonance (SPR) effects induced by the metal NPs will be introduced in terms of qualitative approach. Lastly, the potential industrial application of the Au/SiO_x film is presented as a conclusion to this chapter.

Chapter 3

In this chapter, preparation techniques of Au/SiO_x films will be divided into two parts, i.e. PVD and CVD techniques. First, RF magnetron co-sputtering method (PVD techniques) is used to prepare Au/SiO_x film with “supported ON” and “embedded IN” structure. Next, RF plasma enhanced chemical vapour deposition method (CVD) is used to prepare SiO_x film. For the preparation of Au, two different techniques are introduced - DC sputtering technique and hot wire evaporation technique. For the post-deposition process, thermal annealing technique is necessary in this work. Analytical techniques are carried out using FESEM, FTIR, XRD and UV-VIS-NIR spectrophotometer. Their operation mechanism and provided information will be discussed.

Chapter 4

This chapter presents the important results of this work, which is basically illustrated based on four different analytical techniques as mentioned in the preceding chapter. For PVD grown Au/SiO_x films, effect of annealing temperature on the growth of Au NPs is studied. As for the CVD grown Au/SiO_x film, effect of flow rate ratio of N_2O/SiH_4 on the growth of Au NPs is investigated. With the optimal annealing temperature and flow rate ratio of N_2O/SiH_4, role of SiO_x film in the growth of Au NPs and effect of heated SiO_x film on the growth of Au NPs are studied in detail.

Chapter 5

This chapter expresses a conclusion by covering reviews on the objectives of this work. The objectives have been achieved and correlated with the results shown in the previous chapter. In addition, simple and brief description about this work is made, pointing out its influence on the scientific community.

CHAPTER 2

LITERATURE REVIEW

2.1 Introduction

In this chapter, research background of this study will be introduced. It starts with the introduction to the purpose of studying metal-dielectric film with regarding to its important uses in technology nowadays. Secondly, the reason for choosing gold (Au) and silicon suboxide (SiO_x) as the candidate for metal and dielectric material respectively in this study will be illustrated in more detail. Some similar research carried out by other researchers will also be discussed here. It is generally known that an intriguing phenomenon, called the surface Plasmon resonance (SPR), can be induced by the metal NPs. Without ignoring its importance, the physics behind this phenomenon and its practical uses in many fields of application will be briefly discussed. Finally, the potential application of Au/SiO_x film and the value of this research to industrial applications such as solar cell technology and memory devices will be discussed.

2.2 Metal-Dielectric Nanocomposite Films

Metal-dielectric nanocomposite films are known to consist of metal (Au, Al, Pt, Cu, Ag etc.) and dielectric matrices (SiO_2, Si_3N_4, ZnO, TiO_2 etc.) *(Armelao et al., 2006; Yu et al., 2005)*. Due to their possibilities for functional application and economic impact, these materials have attracted widespread and great technological interest in the development of optical, photonic and electronic devices *(Armelao et al., 2006)*. Therefore, this phenomenon requires scientists and researchers to fully understand the behavior of metal-dielectric nanocomposites and their characteristics including structure, chemical composition and morphology.

Basically, there are two categories of metal in nature - base metal and noble metal. In general, base metals are considered as metal that oxidizes or corrodes relatively easily. They are common and inexpensive. Examples of base metals are aluminum (Al), copper (Cu), iron (Fe), nickel (Ni), lead (Pb) and zinc (Zn). On the other hand, noble metals tend to resist corrosion and oxidation in moist air. Metals like ruthenium (Ru), palladium (Pd), silver (Ag), iridium (Ir), platinum (Pt), and gold (Au) are categorized in this group. Furthermore, noble metal can be defined more strictly by requiring that the d-bands of the electronic structure are filled and do not cross the Fermi level. In this way, only gold (Au), silver (Ag) and copper (Cu) fulfill the requirement as a noble metal. By far, it can be seen that copper (Cu) has an ambiguous role in both categories and has remained fascinating like other metals to many researchers for centuries *(Ghodselahi et al., 2010; Yeshchenko et al., 2007).*

As a matter of fact, metal in the nanocomposite can be found in the form of particles, clusters, granular films, percolation films and continuous films *(Barreca et al., 2004).* In recent years, however, *nano*-dimensional regimes have attracted significant attention by researchers worldwide because metal particles at the nanoscale are observed to be able to exhibit intriguing characteristic properties that are distinctively different from their corresponding bulk materials *(Guerrero-Mart ńez et al., 2010; Sau et al., 2010).* This phenomenon arises from the scaling factors and confinement of charge carrier. As metal particles are confined to the size in nanoscale, surface to volume ratio has been enhanced resulting in a dramatic change in the spectrum with corresponding to the size- and shape-dependent properties. One of the best known examples is the Lycurgus cup in Roman times, as shown in Figure 2.1.

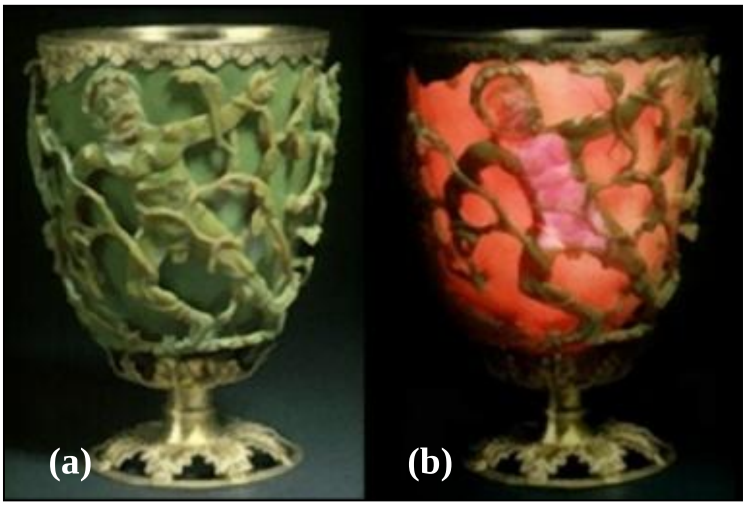

Figure 2.1: Lycurgus Cup (a Roman goblet dating from the 4th century A.D) in (a) reflected and (b) transmitted light.

The cup appears to be green in daylight due to reflected light, but turns into red when the light is transmitted from the inside of the vessel. Answer to this mysterious red colour in the Lycurgus cup is due to the light scattering effect exhibited by nano-sized silver and gold particles *(A. Maier and A. Atwater, 2005).* In fact, different size of metal NPs can produce different colours and this is fascinating. Besides that, nanosized metal particles can also exhibit many of the other interesting properties such as surface plasmon resonance (SPR) effect. In general, SPR can be defined as the collective electron oscillation induced by the interaction of the electromagnetic radiation with a metal surface. This phenomenon can lead to higher absorption of light in visible region. The tunable SPR absorption peak is found to be highly sensitive to the structural properties of metal NPs, which in turn change the frequency and intensity of SPR peak *(Barnes et al., 2003; Liz-Marzán, 2005; Su et al., 2003).* The detailed mechanism of SPR effects will be discussed in the next part.

The importance of nanotechnology research, for instance, in terms of NPs can be more clearly seen from the talk presented by Prof. Richard Feynman in 1959, “There is plenty of room at the bottom”...*“When we get the very, very small world - say circuits of seven atoms - we have a lot of new things that would happen that represent* *completely new opportunities for design. Atoms on a small scale behave like nothing on a large scale, for they satisfy the laws of quantum mechanics. So, as we go down and fiddle around with the atoms down there, we are working with different laws, and we can expect to do different things ….”(Feynman, 1992).* Feynman has pointed out that there are a lot of challenges remain unsolved as we play around with *nano*-dimensional regimes. Hence, it is a great motivation for scientists to move forward.

Another important component in metal-dielectric nanocomposites is the dielectric materials. Dielectric matrices, like SiO_2 and Si_3N_4, have been well-known with their indispensable role in fabrication of components essential to circuit functionality such as capacitors and MOS transistors *(DiMaria and Arienzo, 1987; Doughty et al., 1999; Fuhrer et al., 2002).* In particular, the oxide matrices like SiO_2, Al_2O_3 and TiO_2 have been extensively studied and used as supporting or embedding host for metal NPs in the preparation of nanocomposite *(Armelao et al., 2006; Barreca et al., 2008).* It has been reported by Atwater’s group that the use of an oxide buffer layer can confine the metal growth on a patterned surface and localize the metal island *(Kayes et al., 2007).* It is a very important feature for the study of metal NPs and its interesting optical properties of SPR. Besides that, other properties that most of the oxide matrices possess include insulating character, optical transparency in visible range, structural and thermal stability and most importantly, weak interaction with metal NPs *(Armelao et al., 2006; De Marchi et al., 2002; Vittadini and Selloni, 2002)*

Metal-dielectric nanocomposite film can be prepared in different structures such as core-shell, single layer and multilayer structure. For single layer and multilayer structure, metal can be either embedded IN or supported ON the dielectric matrices, as shown in Figure 2.2. In order to fully exploit the potential uses of these structures, it is mandatory to develop a low cost and effective preparation technique that can produce large amounts of metal NPs or nanoclusters with well-controlled size and shape.

Nowadays, the available preparation technique can basically be divided into two categories, which are physical technique and chemical technique. Example of physical technique includes the sputtering method (DC, RF and reactive) *(Barreca et al., 2004)*, evaporation method (thermal and electron beam) *(Ferrari et al., 1995)*, ion implantation *(Mohapatra et al., 2007)*, ion beam assisted method *(Mohapatra and et al., 2007)*, laser ablation *(Videla et al., 2010)*, pulsed laser deposition (PLD) method *(Jin et al., 2006)* and hybrid method combining the sputtering and plasma enhanced chemical vapor deposition (PECVD) *(Barreca et al., 2008)*. As for chemical methods, they include sol-gel *(Innocenzi et al., 1996)*, impregnation *(C.-y. Wang et al., 1997)*, hydrothermal *(Yoshimura and Byrappa, 2008)* and co-precipitation *(Zheng and Stucky, 2006)*. All the methods mentioned above are bottom–up approaches which involve building up the materials by using small atoms or molecular levels as basic building blocks. This is complementary to the traditional material processing technique called top-down approach. Lithography technique for semiconductor processing is one of the examples with this approach *(Bullen and Garrett, 2002; Thompson L, 1983)*. It is strongly dependent on the wavelength of the light source. The smaller the wavelength of the light source, the smaller the devices can be fabricated. However, eventually there will be a limit. Therefore, in this work, a low cost, novel and modified bottom-up technique has been developed to prepare metal-dielectric nanocomposite film. The experimental setup of this technique will be discussed in detail in Chapter 3.

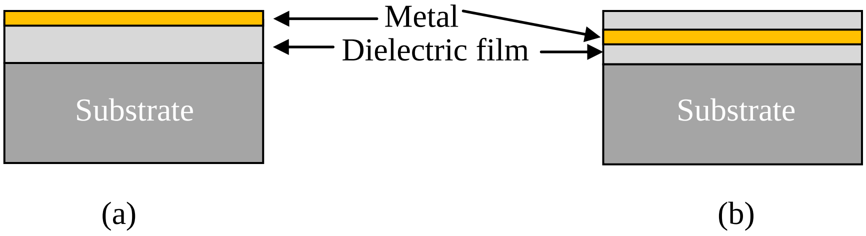

Figure 2.2: Supported ON (a) and embedded IN (b) structure of metal/dielectric nanocomposite films

2.3 Au/SiO$_x$ Nanocomposite Film

In this work, gold (Au) was used as metal source in the preparation of nanocomposite film. Gold, like other metals, generally is malleable and ductile, conducts electricity and heat, and has a metallic luster. As we know, the gold forms a strong metallic bond which is non-directional and strong due to the positively charged metal atoms in fixed positions surrounded by delocalized electrons. The delocalized electrons are said to be "free" and ready to move throughout the metal, which in turn contributes to high electrical and thermal conductivities and luster. Besides that, Au is known to be inert. For instance, it is not a good catalyst for oxidation or hydrogenation process which requires adsorption of the reactants. Reactive molecules like O_2 and H_2 do not adsorb on gold surfaces *(Mavrikakis et al., 2000)*. However, recently, there is report about the nanosized Au particles on oxide medium that can be a very efficient catalyst in CO oxidation process at low temperature *(Grunwaldt and Baiker, 1999)*. This can be attributed to the fact that the interesting properties of nanoscaled Au particles can be developed due to the lack of symmetry at the interface or electron confinements that do not scale linearly with size *(Eustis and El-Sayed, 2006)*. These size-dependent properties of Au NPs are really different with their corresponding bulk materials, which result in many material scientists researching on nanosized material in recent years. This phenomenon mainly results from the additional energetic term of $\gamma_o A$ where γ_o is surface excess free energy and A is the surface area *(Ruffino et al., 2008)*. Due to the large surface/volume ratio of nanosized particles, this term has become important in changing the physical and chemical properties of NPs with respect to its bulk materials. For example, Takagi in 1954 observed that the ultrafine metallic NPs melt below their corresponding melting temperature *(Takagi, 1954)*.

With these intriguing properties exhibited by nanosize Au particles, it is believed that Au NPs have the potential as a fundamental component of future nanoelectronic devices. For the past few decades, Au has been one of the most crucial deep level impurities or contacts and interconnects widely used in many Si-based electronic devices *(Eustis and El-Sayed, 2006).* However, in other cases, Au can degrade the performance of devices since Au produces acceptor and donor levels in silicon which can act as a trap to allow recombination of opposite charges and thus poison device performance *(Hyung-Seok et al., 2011).* Therefore, it is essential to have thorough understanding of Au-Si interaction especially near the surfaces and interfaces.

Furthermore, as we know, Au NPs are well-known to spontaneously agglomerate, making it very difficult to study interesting properties of individual particles *(Bjørnholm, 2009).* Therefore, it is essential to inhibit the agglomeration by stabilizing the surface atoms of Au NPs using suitable chemicals. In this way, for the fabrication or preparation of stable and non-aggregated Au nanoparticles (Au NPs), the most popular synthesis method is by adopting chemical methods *(Sardar et al., 2009).* This includes dispersing Au NPs homogeneously in the solutions as colloidal suspensions. These colloidal suspensions are then spread on a solid substrate or onto the surface of water before it is transferred to a solid surface. Be aware that the latter technique is used for hydrophobic particles. With chemical method, ordered and densely-packed NPs arrays on solid surface are believed to be more easily obtained *(Daniel and Astruc, 2003; Santhanam et al., 2003).* However, the chemical method for fabrication of metal NPs (Au NPs) is not usually environmentally clean since it needs special laboratory conditions *(Videla et al., 2010).* On the other hand, purity of NPs surface is also expected to affect the electronic structure, optical properties and crystallographic phase of NPs. It has been reported that the stabilizer surrounding Au NPs' surface can influence the shape and peak position of the SPR peak of Au NPs *(Boyen et al., 2001).* Besides that, thiol-capped Au NPs have also been reported to undergo a transition from metal to insulator on the basic of an absence of the SPR peak in optical absorption spectra *(Zhang and Sham, 2003).* In fact, some biological applications also require pure nanosystems. In this way, the importance of studying properties of individual particles without the influence of capping chemical or stabilizing agents is highly appreciated *(Balamurugan and Maruyama, 2005).* This can help scientists to distinguish the effect of chemical surfactants and structural properties of NPs (size, shape, etc.) on the electrical and optical properties of NPs. By doing so, NPs can be employed for device fabrication with better efficiency.

To fulfill this requirement, the physical method can be used to prepare NPs with open surface. In this case, silicon dioxide (SiO_2) matrix is the best candidate to replace chemical stabilizers in preventing agglomeration of Au NPs. For the past few decades, SiO_2 matrices have been widely used in electronic devices because of its insulating character, structural and thermal stability and adjustable refractive index in a very broad range, which makes it very useful in wideband antireflection coating or mirrors. However, in this work, the novelty of SiO_2 is that it has weak interaction with metal particles besides having ability to block the agglomeration of metal NPs *(Armelao et al., 2006).* It has been reported that the formation energy of particles decreases as surface tension decreases. Also, the surface tension of Si (0.78 J/m^2) is known to be lower than that of SiO_2 (1.5 J/m^2), indicating that higher formation energy of particles is required on SiO_2 than c-Si *(Bruno et al., 2010; Carel, 1995).* Thus, further agglomeration of Au NPs on SiO_2 can be inhibited more efficiently compared to that on c-Si which allows the formation of Au-Si alloy. The alloy formation can be attributed to the gold diffusion into the substrate at much lower temperature since the Au/Si phase diagram has a eutectic point at 636 K, making it easy to form Au/Si alloy or droplets *(Adachi, 2002).*

In fact, there are two general preparation strategies that have been used to prepare Au/SiO_2 nanocomposite films. They are top-down and bottom-up approach, as mentioned in previous sub-chapter. One of the examples of top-down approach is lithography technique such as photo-lithography and E-beam lithography. They can be used to prepare Au NPs on silica with highly ordered array. However, this expensive approach has limitations in preparation of nano-scaled samples. Therefore, bottom-up approach is a well-known option in addressing this problem. In general, bottom-up approach can be divided into two techniques which are chemical and physical techniques. For chemical techniques, there are impregnation, co-precipitation or deposition-precipitation method, colloidal deposition, sol gel, wet chemical and layer-by-layer assembly *(Innocenzi et al., 1996; Lau et al., 2011; Wang et al., 1997; Zheng and Stucky, 2006).* As for physical techniques, they include ion beam assisted techniques, ion beam implantation, atom beam sputtering, sequential sputtering, evaporation, RF magnetron sputtering techniques and hybrid technique combining DC sputtering and RF plasma enhanced chemical vapor deposition (RF-PECVD) method *(Barreca et al., 2004; Barreca et al., 2008; Bruno et al., 2010; De Marchi et al., 2002; Ferrari et al., 1995; Mohapatra and et al., 2007; Yu et al., 2005).* It can be said that each of these different techniques has its own different advantages and disadvantages. Therefore, it is a critical task to obtain the optimal process parameter in order to produce the desired results. In this work, for the first step the researcher used the RF magnetron sputtering technique to prepare Au/SiO_x films. Next, the researcher used both DC sputtering and RF-PECVD to prepare the samples. In the final step, the experiment setup was modified to be hot wire assisted PECVD technique for obtaining desired results. The details of this experimental set up will be discussed in the next chapter.

Undeniably, metal-dielectric films have become one of major focuses in nanotechnology, especially the research about Au/SiO_2 nanocomposite films. For instance, Ruffino *et al.* studied the normal and abnormal grain growth besides kinetic roughening in nanostructured Au film on SiO_2 *(Ruffino et al., 2009)*; B. Balamurugan *et* *al.* showed how the contamination-free NPs surface is essential to observe the size-dependent optical and electronic properties *(Balamurugan and Maruyama, 2005)*; Dan Dalacu *et al.* investigated the temperature dependence of the surface Plasmon resonance of Au/SiO_2 nanocomposite films *(Dalacu and Martinu, 2000)*; Davide Barreca *et al.* developed an innovative synthetic route to SiO_2- sandwiched AuNPs arrays *(Barreca et al., 2008)*; Hirasawa *et al.* studied the growth mechanism of sputtered Au film on SiO_2 as a function of the sputtering time *(Hirasawa et al., 1997)*. From the examples stated above, it is highly recognized that nanotechnology, especially the research about metal-dielectric nanocomposite film, will become increasingly important in future and affect every part of our lives.

2.4 Surface Plasmon Resonance in Au nanoparticles

Miniaturization of optical components to size dimensions of their electronic counterparts involves interesting physical processes such as light localization and guiding for electromagnetic (EM) radiation *(A. Maier and A. Atwater, 2005)*. To study such processes, an interdisciplinary field known as *plasmonics* was proposed and has become one of the important research fields regarding modern optics in recent years *(Halas, 2010; Maier et al., 2001; Morton et al., 2011; Murray and Barnes, 2007)*. Back in 1908, Gustav Mie published an important paper about the contributions to the optics of turbid media, particularly solution of colloidal metals *(Mie 1908)*. His work for interaction of light with small metal particles has attracted many researchers to investigate this growing field. At the core of the plasmonics field, deep understanding about the interaction of light with metals on nanoscale size is urgently required.

In fact, the interaction between very small metal NPs and light was already observed in Byzantine Empire, 4th century A. D. It can be observed from the Lycurgus cup which is now on display in the British Museum [Figure 2.1]. The interesting phenomenon shown by this glass goblet has been discussed briefly in sub chapter 2.2. However, the main point here is that the different color change by the Lycurgus cup is the result of the surface Plasmon resonance (SPR) phenomenon exhibited by metal NPs embedded IN the glass, resulting in the strong optical absorption of light at certain wavelength in visible spectrum. In this case, it is the green part of the optical spectrum. In general, there are two types of SPR which are surface plasmon polaritons (SPPs) and localized surface plasmon resonance (LSPR) *(Halas et al., 2011; Jones et al., 2011)*. The former phenomenon originates from the propagating wave along metal surface or metal-dielectric film boundaries. As for LSPR, it can be attributed to the localized plasmon in the metallic NPs having dimensions smaller than the wavelength of incident light, λ. However, SPR is a general term for both cases to describe confined plasma oscillations.

For a clearer understanding of SPR, it can be compared to the mechanical oscillator like a simple harmonic oscillator *(Jones et al., 2011)*. It is known that a restoring force will bring the oscillator back to the initial position as the oscillator is displaced out of its position by an external force. The oscillator can undergo a sinusoidal oscillation which will come to a stop with the damping effect or external force. If a sinusoidal external force is applied on the oscillator, it will reach maximum amplitude at certain frequency by absorbing maximum amount of energy from the driving external force. This specific frequency is called resonant frequency where the frequency of the sinusoidal external force is in phase with the natural frequency of the oscillator *(A. Maier and A. Atwater, 2005)*. On the other hand, it can be said that higher frequency or energy is not a must to induce the highest amplitude of oscillation. So, the same principle can be applied to the SPR phenomenon.

In metal NPs, conduction electrons at the surface of NPs with diameter, $d << \lambda$ can be confined to the small particle volume resulting in the in-phase movement during plane wave excitation with EM radiation of wavelength, λ *(Kreibig and Vollmer, 1995).* Here, the conduction electrons with coherent oscillation around the positively charged nuclei can be regarded as an oscillator. Each of the incident EM radiations possesses oscillating electric fields which move perpendicularly to the magnetic fields. The metal NPs' conduction electrons will be disturbed by the oscillating field, resulting in the build-up of charge polarization as the EM radiations incident on the surface of metal NPs, as represented in Figure 2.3. However, the charge polarization is short-lived as heavy positively charged nuclei will pull the conduction electrons back to their initial position due to the coulomb attractive force. Here, the oscillating field of EM waves acts as a driving external force while the coulomb attractive force is the restoring force for the conduction electrons.

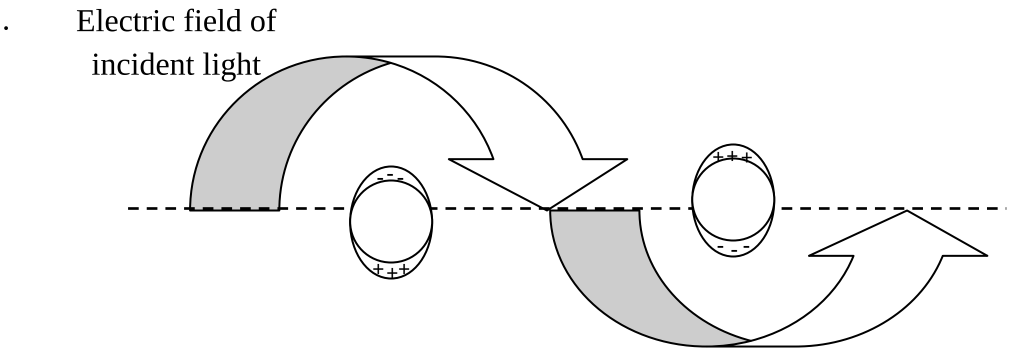

Figure 2.3: Schematic diagram showing the charge polarization resulting from the interaction between electromagnetic waves and conduction electrons in metal NPs.

Like simple harmonic oscillator, resonance will be achieved as the frequency of incident EM waves is in phase with the natural frequency of the plasmon oscillation of conduction electrons. This resonance is called surface plasmon resonance. At this SPR frequency, the response of electrons shows a $\pi/2$ phase lag with respect to the driving field, leading to a resonantly enhanced field build up inside the particle homogeneously throughout its volume, producing a dipolar field outside the field *(A. Maier and A. Atwater, 2005).* In this case, metal NPs will absorb the maximum amount of photon energy from EM waves, resulting in the largest charge displacement and enhancement in absorption and scattering cross sections for EM waves. SPR phenomenon can also generate higher local electric field enhancement which is around 100 to 10,000 times higher than the incident field due to confinement effect of surface plasmon in a small volume *(Jones et al., 2011)*. If the coupling between the surface plasmons can be well controlled, extremely high local electric field can even be obtained. The optical absorption spectrum for the metal NPs can be obtained by addressing the Maxwell equations for small spherical particles interacting with an EM field and retain the only dipolar term. The dipolar term is suitable for NPs with a diameter $d << \lambda$, where λ is the wavelength of EM wave as stated above.

2.5 Potential Application of Au/SiO$_x$

From the previous sub-chapter, it is clearly seen that Au/SiO$_x$ films can exhibit a lot of interesting properties, which can be useful to be applied in the optoelectronic industry. There have been many reports about the potential application of Au/SiO$_x$ films for the past decades. For instance, blue luminescence of Au nanoclusters (< 10 nm) embedded IN SiO$_2$ matrix has been reported in 3.1 and 3.4 eV *(Dhara et al., 2004).* This has widely explored its application in nano- and optoelectronic device. In case of multilayer stacks of Au/SiO$_x$ films, photonic structure with high transparency in the visible and near UV region can be obtained with proper controlled thickness of Au and SiO$_x$ film. In contrast, single metal film of the same total thickness is opaque in the same spectral interval (Z. Wang et al., 2006). By tuning the thickness of metal or dielectric film, different properties of photonic devices can be exhibited.

In addition, ability of Au NPs to exhibit SPR phenomenon and nonlinear optical response enables them to be fully utilized in linear and nonlinear optical devices like optical switch, molecular detectors and biosensors *(Haes et al., 2004; Maier et al., 2001; Reinhard et al., 2005; Sardar et al., 2009).* Beyond the optical devices, Au/SiO$_x$

films also have potential to be employed in plasmonic solar cell *(Barnes et al., 2003; Rosa et al., 2011)* . It has been reported that photocurrent enhancement of up to 20x over a narrow frequency range can be realized by preparing the plasmonic NPs, such as Au NPs, on top of a photovoltaic device *(Hall, 1998).* Furthermore, plasmonic NPs are believed to be able to enhance charge carrier generation and photocurrent generation in the dye-sensitized solar cell (DSSC) such as dye monolayer on flat dielectric film *(Spyropoulos et al., 2011).* Conventionally, it is thought that the photovoltaic absorbers must be thick enough to complete the light absorption and charge carrier collection. However, it becomes unnecessary since the emergence of plasmonic NPs. These NPs have greatly enhanced the photocurrent efficiency and reduced the cost per watt of thin film solar cell. On the other hand, Au/SiO$_x$ film can be applied in the field of memory devices where Au NPs are placed between the tunneling layer and blocking layer *(Baker et al., 2011; Leong et al., 2007; Tseng and Tao, 2009).* These NPs can be regarded as a potential replacement for the poly-silicon floating gate. Even though the price of Au is higher than the existing Si technology, but in terms of efficiency, the use of NPs as storage charges can help to reduce the programming voltage and the effective oxide thickness. This solution can help to address the bottleneck expected from Moore’s law which state that the number of transistors that can be placed on an integrated circuit doubles approximately every two years.

With all the above-mentioned potential applications of Au/SiO$_x$ films, it can be deduced that Au/SiO$_x$ film is indeed a very interesting and challenging topic to enroll into it. Furthermore, the plasmonics has become a hot topic in recent years. Therefore, by carefully and properly design of experiment parameters, current study is prospected to contribute to the research of this material significantly.

CHAPTER 3

EXPERIMENTAL AND ANALYTICAL TECHNIQUES

3.1 Introduction

Physical vapor deposition (PVD) and chemical vapor deposition (CVD) techniques are the most commonly used deposition methods to deposit thin films onto silicon or other substrates. The processes of both techniques are quite similar except for the precursors adopted. For PVD method, the material is deposited in the solid form initially. However, for the CVD method, the precursors are introduced to the reaction chamber in the gaseous state. Examples of the PVD method are evaporation *(Murali et al., 2004)*, RF sputtering *(Armelao et al., 2005; Sangpour et al., 2007)*, ion beam implantation *(Yu et al., 2005)*, electron beam deposition *(Maiti et al., 2010)*, etc. These methods provide the advantage of highly directional deposition, high uniformity and almost any type of inorganic material can be used as well as some kinds of organic materials. However, PVD technique has the disadvantages of high cost and low deposition rate. On the other hand, thin-film deposition prepared by the CVD method is the result of reactions between various gaseous phases and the heated surface of substrates within the CVD reactor chamber. The carrier gases involved in the CVD method include N_2O, SiH_4, He, N_2, O_2, CH_4, etc. The CVD method can be enhanced to produce high efficiency deposition. Plasma-enhanced CVD (PE-CVD) *(Barreca et al., 2008; Dao et al., 2009)*, hot wire CVD (HW-CVD) *(Gallagher, 2001)* and low pressure CVD (LP-CVD) *(Modreanu et al., 2004)* are examples of enhanced CVD methods. Advantages of CVD include uniform distribution over large area and no compositional gradients across the substrate. However, safety and contamination are the main concerns when using the CVD technique since most of the gases like SiH_4 are toxic and ignite spontaneously in air. In this work, SiO_x films were prepared by PVD (RF magnetron sputtering) and CVD (RF Plasma-enhanced CVD) methods while the Au layer was prepared by the PVD method only, which included DC sputtering and evaporation. Later on, hybrid technique combining CVD (PE-CVD) and PVD (evaporation) was proposed to fabricate Au on SiO_x films to better tailor the structural properties of Au NPs.

The first part of this chapter describes the samples preparation and substrate cleaning procedure. This is followed by the description of the PVD technique using RF magnetron sputtering system. Here, two ways to produce different structures of Au/SiO_x film which is “supported ON” and “embedded IN” structure will be clearly shown. The third part of this chapter presents the CVD technique (RF-PECVD). Since the “supported ON” structure will be discussed in detail later on, two ways of preparing Au layer on surface of SiO_x films will be discussed here. They are DC sputtering technique using sputter coater and evaporation technique using hot wire. Modification on hot wire technique to meet the desired parameters in this work will be presented. This will be followed by a presentation of the post-deposition process, i.e. thermal annealing technique, which is used to induce the growth of Au NPs. The final part of this chapter includes analytical techniques utilized in characterizing the films besides the characterization procedures and calculation techniques used to analyze the results obtained from the measurements. These characterization techniques include field emission scanning electron microscopy (FESEM), Fourier transform infrared (FTIR) spectroscopy, X-Ray Diffraction (XRD) and optical transmission spectroscopy.

3.2 Sample Preparation

There are two kinds of substrates used in this work to prepare the Au/SiO$_x$ films. The first is one side polish p-type crystal silicon <111> wafer (c-Si) with resistivity, thickness and diameter of around 1-10 Ohm-cm, 625 ± 25 µm and 150 mm respectively. The second is the quartz slide with dimensions of 3 x 1 x 1 mm. The substrates will be cut into pieces with dimensions of 20 x 20 mm to be placed onto the substrate holder. A substrate holder can fit 4 pieces of substrates in this dimension. Prior to the sample preparation in the vacuum chamber, the substrate cleaning process is of utmost importance to ensure that the contaminants on the substrate, which may affect the properties of the film deposited on the substrate, can be removed since the effective cleaning of the substrates has a strong effect on the adhesion properties of deposited films. Residues from manufacturing and packaging, lint, fingerprints, oil and airborne particulate matter are examples of frequently encountered contaminants. The cleaning process adopted in this work is similar to the Radio Corporation of America (RCA) cleaning process, which involves the removal of organic contaminants, thin oxide layer and ionic contamination. This RCA cleaning process was developed by Werner Kern in 1965 while working for RCA (Radio Corporation of America) *(Mattox, 1998; Clark & Wagener, 2008).*

The cleaning process for the c-Si substrates begins with rinsing the substrates in the deionized water and then rinsing it again in a beaker containing deionized water, hydrochloric acid (37 %, 36.46 g/mol) and hydrogen peroxide (30 %, 34.01 g/mol) solution with the ratio of H_2O: HCl: H_2O_2 is 6:1:1 for 7 minutes. This process is to remove the metallic and ionic residues. After that, the substrates are rinsed once more in deionized water for 5 minutes. The next step is to rinse the substrates in a mixture solution of deionized water, hydrogen peroxide (30%, 34.01 g/mol) and ammonia solution (25 %, 17.03 g/mol) with the ratio of H_2O: H_2O_2: NH_3 being 5:1:1 for 7 minutes, followed by rinsing it again in deionized water. The purpose of this step is to remove the organic residues. Finally, thin oxide film removal is carried out by rinsing the substrates in a mixture solution of deionized water and hydrofluoric acid (48-50%, 20.01 g/mol) with the ratio H_2O to HF of 10:1 for 5 minutes and followed by rinsing the substrates in deionized water for 5 minutes. For safety reasons, chemically resistant gloves should be worn throughout the cleaning procedure since some solutions like HF are very toxic and corrosive. The final step in the cleaning process is to dry the substrates using industrial nitrogen gas (N_2, 99.9 %) gun blower. Following the drying, the substrates are ready for the next step in the process. The clean substrates are placed in the reaction chamber which is immediately evacuated to vacuum condition. It is important that this next step need to be performed immediately to ensure that the substrates are as clean as possible. The vacuum in the reaction chamber will ensure minimum oxide formation on the c-Si substrates.

As for the cleaning process of quartz substrates, it begins with immersing the substrates in a beaker containing soap solution, a mixture of Decon 90 and deionized water, prior to putting the whole beaker into an ultrasonic bath for ultrasonic cleaning process, which lasts for 20 minutes at a temperature of 70 ^{o}C. In ultrasonic cleaning, a high frequency sound wave is used to agitate in reverse osmosis (RO) water which in turn acts on contaminants adhering to substrates. Contaminants can be dust, dirt, oil, grease, polishing compounds, and fingerprints. The quartz substrates are then rinsed in deionized water before being further rinsed in highly flammable acetone, C_3H_6O (99.5 %, 58.08 g/mol) and finally in ethyl alcohol, C_2H_5OH (95 %, 46.07 g/mol) to remove any oil deposits and other contaminants. The next step is to dry the substrates using N_2 gun blower to prevent the formation of water spots. Like the preparation of c-Si substrates, the cleaned quartz substrates are immediately put into the reaction chamber followed by pumping down the chamber to the vacuum level to be ready for the experiment. This procedure is to prevent contamination on the surface of the clean substrates.

The extra clean c-Si and quartz substrates used as a background for characterizations usages are stored in a dry cabinet with humidity of 32 for keeping the substrates clean and free from contaminants.

3.3 Physical Vapor Deposition (PVD) Technique

3.3.1 RF Magnetron Sputtering System

3.3.1.1 Introduction

The PVD system used in this work is Edwards Auto 306 DC and RF Magnetron Sputtering System. It is frequently used to sputter metal and dielectric materials. As mentioned in Part 3.1, sputtering is a physical vapor deposition (PVD) process. To start with, DC or capacitive coupled RF power supply is introduced into target acting as power electrode via the electrical feed through to produce high negative potential. Substrate holder located above target material is regarded as grounded electrode. Plasma will be generated in between two electrodes in the vacuum chamber under low pressure conditions. Electrons emitted from the target material will ionize the reactive gas introduced into the chamber, such as Argon gas, to generate high energy positive ions. These energetic positive ions will be strongly accelerated and attracted to strike the target vigorously, leading to the dislocation and release of the atoms of target material. These deposition sources will then be directed towards the substrates and coat on them to form thin films. Since the system used is called magnetron sputtering system, high strength magnets are incorporated beneath the target. The magnetic field generated can trap and concentrate the electrons emitted from target material besides enhancing the plasma to increase the sputtering rate and its efficiency *(Matsuda et al., 2003)*. In this way, electrons can also be kept away from the substrate to reduce the collision damage on the substrate. The detailed sputtering mechanism is presented in Figure 3.1.

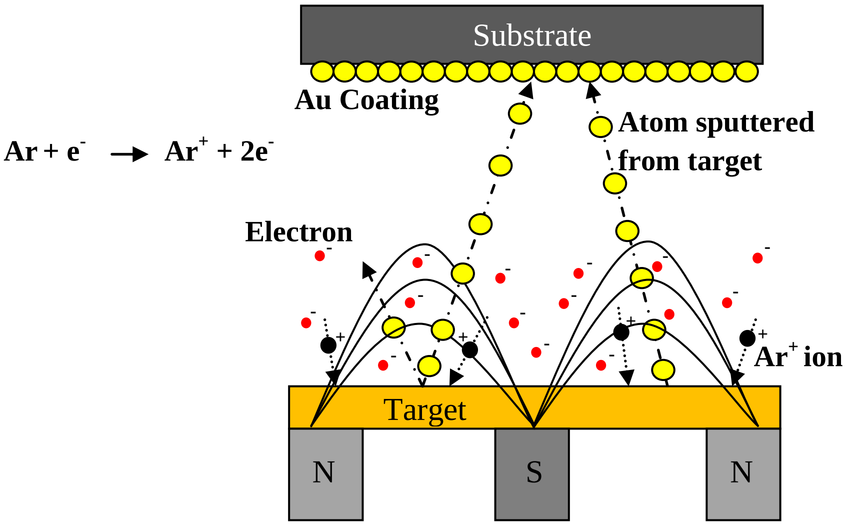

Figure 3.1: Sputtering mechanism of magnetron sputtering.

The main advantages of this technique are deposition of film with constant composition, ease of control and reproducibility. Basically, Edwards Auto 306 DC and RF Magnetron sputtering system consists of a deposition chamber and control cabinet including MFC control panel, pressure control panel, work holder control, DC and RF power supplies. This schematic diagram for the system is clearly presented in Figure 3.2.

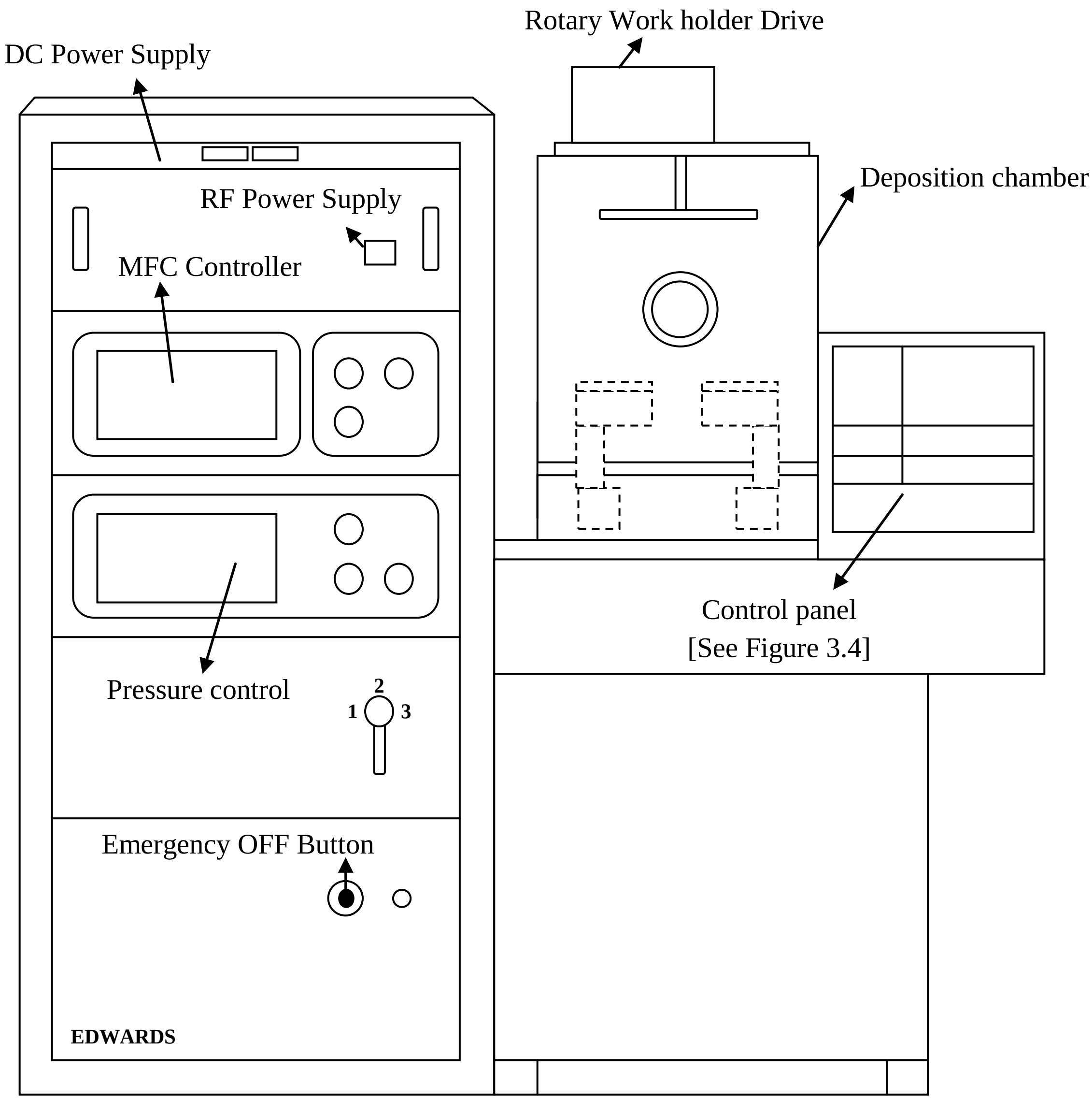

Figure 3.2: Schematic diagram of Edwards Auto 306 DC & RF Magnetron Sputtering System

Inside the deposition chamber, there are two magnetron sources (one for DC, another for RF), a crystal monitor (to determine the sputtering rate by correlating deposited film thickness to the amount of deviation from its original crystal resonant frequency), shutter, rotary substrate holder, and heat lamp. In order to assure a good seal of deposition chamber, the door having a magnetic bearing should be closed gently and without exerting any force. As for the control cabinet, it allows us to vent and pump down the chamber by pressing the appropriate button. We can control the flow rate of the reactive gas introduced, value of DC and RF power for the deposition process, speed of rotary substrate holder, substrate temperature and shutter. Real images of these controllers are presented in Figures. 3.3 and 3.4.

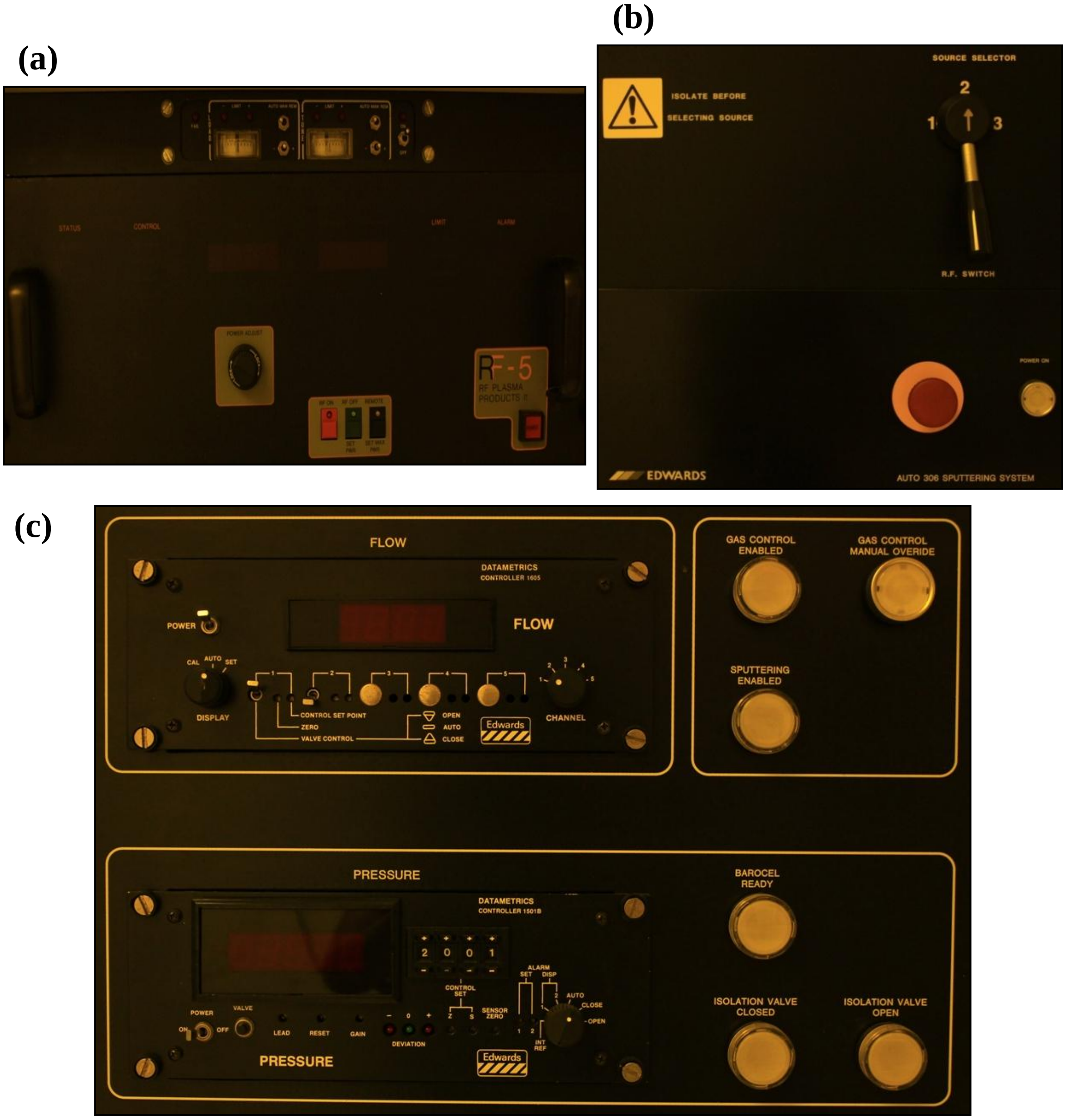

Figure 3.3: Real image of (a) DC and RF power supply, (b) Emergency OFF button and (c) MFC and pressure controller

Figure 3.4: Real images of components on control cabinet

To start the deposition process, we need to ensure that we follow the safety rules by reading all relevant instructions before operating any accessories. One of the rules that we must follow is to wear clean lint-free gloves when handling components in the chamber. This can help to prevent contamination of the evaporation materials and the accessories. Thus, the handling components can be cleaned using some acetone now. After that, we can open the shutter for appropriate magnetron to place the dielectric target (SiO_2, 99.995%) with diameter of 100 mm by using the control unit to the right of the chamber (SS1 or SS2). The target shield cylinder surrounding the magnetron is lifted and the copper ring on top of the target is unscrewed. Then, the SiO_2 target is placed in the center of the top surface by inserting a copper plate beneath it in between SiO_2 target and magnet. This is because the SiO_2 target, unlike copper plate, is not a conducting material. The copper ring is placed back in place and screwed down in a diagonal pattern. The cylinder is put back around the magnetron; the shutter is closed once the target is in place. After that, the substrates are placed on the substrate holder and checked to make sure the holder can rotate freely. The chamber door is closed gently and the PROCESS button is pressed to evacuate the chamber to reach the base pressure and the process interlock will be enabled within 10 minutes.

After that, gas flow controller and DC and RF power supplies are enabled. The flow rates of Argon gas and oxygen gas are set to 15.2 and 4.4 sccm, respectively. Since RF power supply is more efficient to sputter the dielectric matrices as compared to DC power, only RF power is introduced in this work. The RF power is fixed at 120 W. The base pressure achieved before deposition reads 9.0×10^{-5} mbar. During the deposition process, the pressure increases to 2.3×10^{-2} mbar. The deposition time for the entire process is kept at 4 hours. To prepare “supported ON” and “embedded IN” structure, different target preparation is required and the detail will be expressed in the next part.

3.3.1.2 "Supported ON" Structures

For the fabrication of "supported ON" structure, only silicon dioxide target with diameter of 100 mm will be sputtered in the presence of argon and oxygen gas. The preparation of SiO_2 target is shown in Figure 3.5. Thus, only SiO_x film will be formed on the surface of c-Si and quartz substrates. These as-prepared SiO_x films will then be coated with a very thin layer of gold using sputter coater (see part 3.5.1) to form Au ON SiO_x films as illustrated in Figure 3.6.

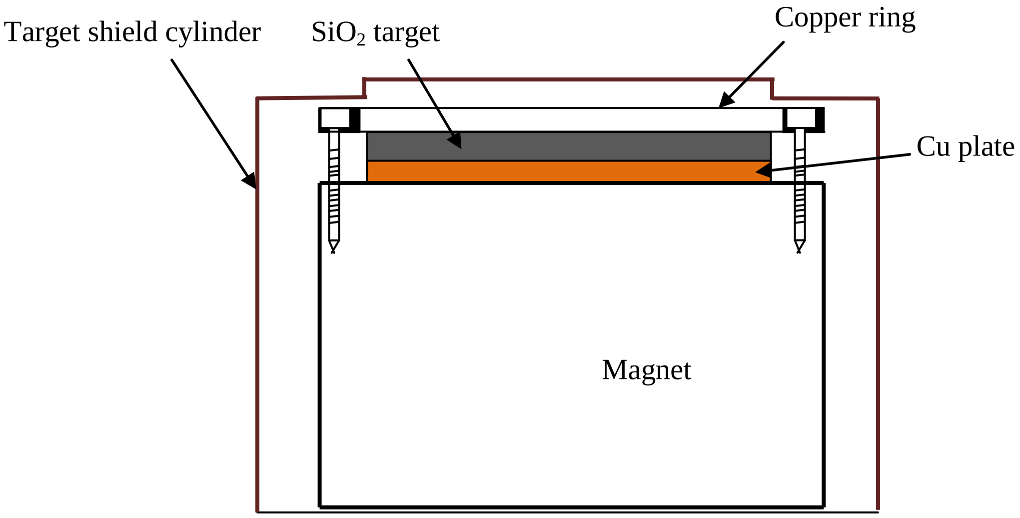

Figure 3.5: Preparation of SiO_2 target

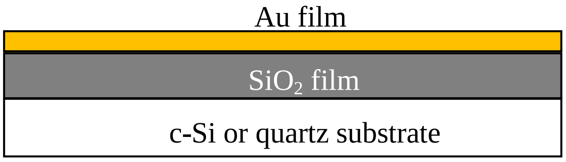

Figure 3.6: "Supported ON" structure of Au/SiO_x film

3.3.1.3 "Embedded IN" Structures

The fabrication of "embedded IN" structure is prepared in different ways. Sputter coater is not required to coat a thin layer of Au onto the surface of SiO_2 films. Au wire and SiO_2 target will be co-sputtered in the deposition chamber to prepare SiO_2 film embedded with Au. 1 cm Au wire with diameter of 1 mm will be cut into 4 pieces of Au wires of 2.5 mm in length. They will be placed symmetrically onto the surface of SiO_2 target with diameter of 100 mm prior to the sputtering process in the presence of argon and oxygen gas. The preparation of Au wire and SiO_2 target is shown in Figure 3.7. Thus, Au IN SiO_x film, as illustrated in Figure 3.8, will be formed on the surface of c-Si and quartz substrates in this one-step process.

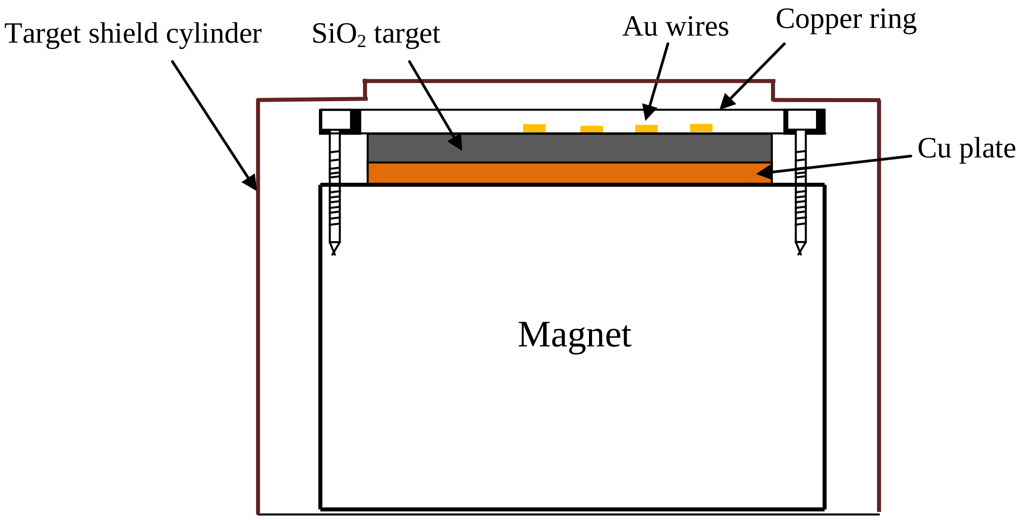

Figure 3.7: Preparation of Au wire and SiO_2 target

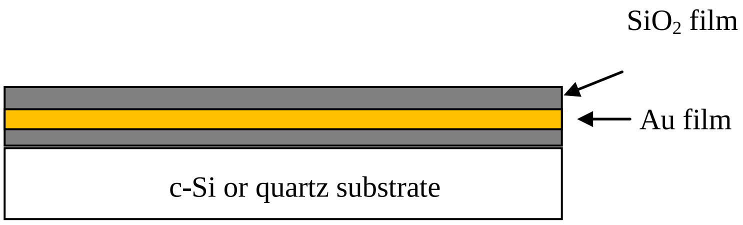

Figure 3.8: "Embedded IN" structure of Au/SiO_x film

3.4 Chemical Vapor Deposition (CVD) Technique

3.4.1 Radio Frequency Plasma Enhanced Chemical vapor Deposition (RF-PECVD)

The CVD technique used in this work is homebuilt RF-PECVD system. The schematic diagram of this system is shown in Figure 3.9. It can be observed that there are several major parts in this system. The main part is the deposition chamber consisting of 3 components which are top plate, body chamber, and bottom plate. These components are made of stainless steel (SS) since it is resistant to corrosive gases like silane (SiH_4) gas besides not having any reaction with other process gases. The dimensions for the body chamber are 300 mm in height, 150 mm in diameter and 6 mm in wall thickness. It is attached with one glass viewport used to observe the condition inside the chamber during deposition. In addition, the middle part of the top plate is assembled with a stainless steel rotary shaft feed through, with ¼" SS tubing, for use as a gas inlet. The feed through is used to support the inside Teflon (insulator) and showerhead (power electrode) connected with RF power supply. Besides that, two electrodes, which are used for hot filament connection, are introduced into the chamber via electrical feed through.

As for the bottom plate, it is connected directly to a turbo molecular pump and a rotary vane pump via NW 40 SS flexible hose. Also, heater, thermocouple and grounded electrode contact are introduced into the chambers using electrical feed through. For the pressure detection, vacuum gauges like pirani and penning gauge are also attached to the bottom plate with an NW 16 connector. The substrate holder stands on three insulators used to isolate holder from chamber. The heater rod, thermocouple and grounded wire are attached to the substrate holder as shown in Figure 3.11. The distance between showerhead and substrate holder is kept at 30 mm.

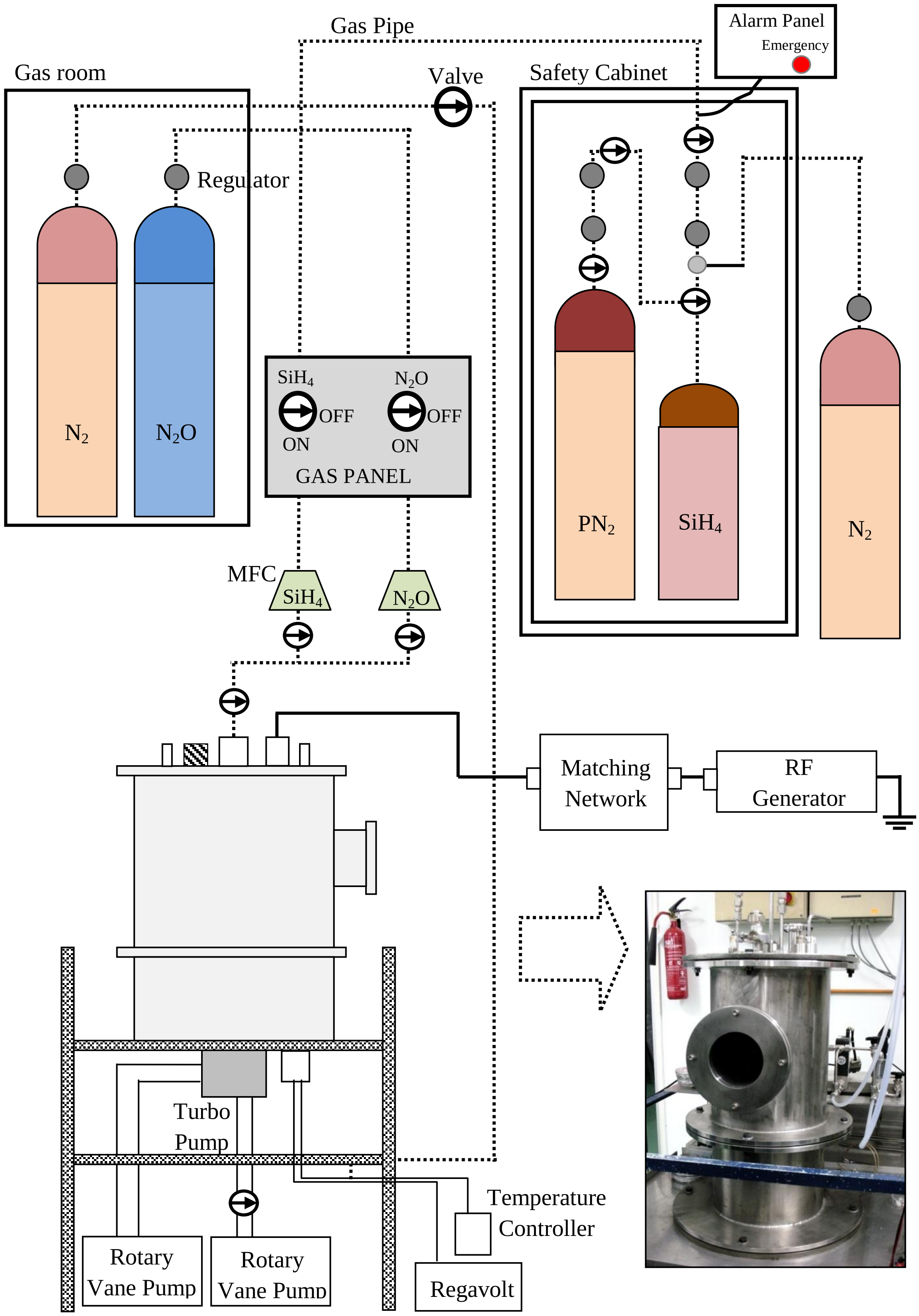

Figure 3.9: Schematic diagram of homebuilt RF-PECVD System and real image of deposition chamber

The substrates are placed onto the top of the substrate holder consisting of four grooves with dimensions of 20 mm x 20 mm each and their measured depth is 5 mm.

A stainless steel plate is used as a mask to fix the position and expose only the deposited area of the substrates. After that, the thermocouple is inserted into a tiny hole located at the edge of holder and touched exactly to the quartz substrate for measuring the substrate temperature. The, the RF supply and showerhead, heater rod and regavolt and grounded contact of substrate holder are properly connected. Next, the deposition chamber is tightly sealed prior to the pumping process.

The pumping system constitutes another major part in the RF-PECVD system. First, a rotary-vane pump (model EDWARDS E2M28) is used to evacuate the deposition chamber to a pressure around 10^{-3} mbar. Then, gas line cleaning process is carried out to ensure there are no gases left in the gas line. After that, the deposition chamber is further pumped down to high vacuum condition until vacuum level of 10^{-5} mbar is obtained by using turbo molecular pump (model TURBOVAC TW 70 H). The minimum pressure recorded is regarded as base pressure achieved in the experiment. In this work, two different pressure gauges are used to determine the pressure level inside the chamber for different vacuum levels. For low and medium vacuum, TTR 90S Leybold Thermovac Pirani Gauge is used. On the other hand, Leybold Penningvac PTR 225 is used for high vacuum levels. It is important to note that the valve of the rotary-vane pump connected to the chamber must be closed before opening the valve of the turbo molecular pump. The otary-vane pump and turbo molecular pump cannot be used simultaneously to evacuate the chamber since their pumping speeds are different, and operating them simultaneously will result in the deterioration of vacuum performance. Besides that, these two pumps are connected to a 10 kVA Uninterruptible Power Supply (UPS) to avoid sudden power shut down. It is important to ensure that SiH_4 gas can continuously flow under pumping and vacuum condition since UPS can sustain the power supply for 2 hours at least if there is interruption in the main power supply.

For deposition of SiO_x film, only two process gases are used – silane (SiH_4, 99.9995 %) and nitrous oxide (N_2O) gas. First, they are distributed from the gas tank inside the gas room to the gas distribution panel via ¼” SS tubing. The Gas regulator near the outlet of the gas tank is used to control the pressure of gas inside the tubing. The gases then will flow towards the deposition chamber by controlling the ball valve on the panel and near the chamber. Before entering the deposition chamber, the gases will flow through the mass flow controller (MFC), with model of Aalborg, GFC 17, which is used to monitor the flow rate of gases. The flow rate of gases is controlled by a metering valve (Swagelok, SS-4MG) before the MFC. In this work, the flow rate of SiH_4 gas is kept at 2 sccm while flow rate of N_2O is varied from 10 to 80 sccm. It must be remembered that the valve should be opened slowly to prevent sudden flow of high pressure gas into the MFC since it can cause damage to it. A bypass line is assembled beside the MFC of SiH_4 gas to allow the removal of SiH_4 gas in higher flow rate if blockage occurs at the entrance of MFC, besides allowing excess SiH_4 gas to be pumped out to the rotary pump at a faster rate during the cleaning process. After MFC, a check valve (Swagelok, SS-CHS4-1/3) is used to allow the gas flow in one direction without any back flow. Here, N_2O and SiH_4 gases will mix and flow together into the chamber via the gas inlet assembled on the top plate.

For safety precaution, SiH_4 gas must be treated sparingly. Thus, the SiH_4 gas tank is stored in a safety cabinet with an exhaust system attached. The exhaust system can be used to remove SiH_4 gas if there is a leakage in the cabinet. A special regulator, with model AP1510S, of SiH_4 gas tank is connected to an N_2 gas tank which acts as a purging system. The pneumatic valve inside the regulator only allows the SiH_4 flow through when the pressure of N_2 reaches about 50 psi. This precaution can prevent dangerous SiH_4 gas from flowing into the chamber vigorously in an emergency.

Industrial nitrogen (N_2) gas is introduced directly into the rotary-vane pump oil compartment instead of the chamber to avoid the SiH_4 gas from condensing in the pump as the SiH_4 starts flowing into the chamber. Also, N_2 gas is used to dilute the SiH_4 gas before excess SiH_4 gas is transferred to a detoxification tank via an exhaust pipe. The excess SiH_4 gas will be directed eventually and deeply to the bottom part of the detoxification tank containing a solution of potassium permanganate ($KMnO_4$, M= 158.04 g/mol). This solution in the detoxification tank will convert or neutralize the excess SiH_4 gas to non-toxic form with chemical reaction shown as shown below *(Lickiss and Lucas, 1996),*

$$8KMnO_4 + 3SiH_4 \rightarrow 8MnO_2 + 3SiO_2 + 8KOH + 2H_2O$$

This process is critical due to the fact that SiH_4 gas is highly toxic and flammable when exposed to air. For safety reasons, the $KMnO_4$ solution must be changed as its color changes, indicating that the chemical reaction is becoming less efficient.

After the introduction of process gases into the chamber, RF power generated by 13.56 MHz RF power supply (ENI, 600 W) is initiated. In this work, RF power is kept at 100 W. Prior to the deposition process, the substrates have been heated up to 300^oC using a heater rod (Watlow firerod cartridge heater, 400 W). IBC regavolt (0 to 240 V AC, 1kVA) and temperature controller (Taishio TS501) are used to supply the voltage to the heater rod and control the temperature of substrates, respectively. The substrate temperature is measured by chromel-alumel k-type thermocouple. On the whole, the parameters used in my work to prepare SiO_x film can be summarized as in Table 3.1 below.

Table 3.1 Parameters for the preparation of SiO_x film

Parameter	**Value**
Flow rate of SiH_4 gas	2 sccm
Flow rate of N_2O gas	10 sccm, 40 sccm, 60 sccm, 80 sccm
Substrate temperature	300^oC
RF power	100 W
Deposition pressure	1.0 mbar
Deposition time	60 min
Gap between powered electrode and substrates	30 mm

3.5 Gold Preparation Technique

3.5.1 DC Sputtering Technique

In this work, SPI- Module Sputter Coater was used to prepare Au film supported ON SiO_x matrix. The schematic diagram is shown in Figure 3.10. Sputter coater provides the advantage of having uniform coating on all shapes or sizes of film since thickness monitor is generally not needed. Also, its compact design allows easy transport from lab to lab besides fast coating (up to 200A gold in 20 seconds) process being achieved easily.

In order to start the coating process, the as-prepared SiO_x films are mounted onto the stub holder which can hold up to five samples with dimensions of 20 mm x 20 mm. The position of the holder stage is adjusted so that the samples are approximately 50 mm from the bottom of sputter head. The glass work chamber is replaced and the gold sputter head is placed on top of the chamber. After that, the timer is set to 20 seconds and make sure the leak valve is fully closed. As the “POWER” switch in the vacuum control base is switched on, the rotary pump will start to evacuate the chamber and the vacuum level will be indicated on the pressure indicator. The gas leak valve in the vacuum control base is partially opened to flush the work chamber with air for about 10 to 15 seconds when the pressure falls to around 8 x 10^{-1} mbar. After that, the leak valve is closed immediately to allow the work chamber to pump down to around 1 x 10^{-1} mbar.

The gas leak valve is then opened until the pressure just begins to rise before pressing the test button intermittently. The gas leak valve is adjusted to control the plasma current to around 18 mA. At the same time, visible plasma discharge can be observed in the chamber. The START button is pressed immediately and the sputtering process will run for the set time (20 s). After 20 s, plasma will automatically disappear. The “POWER” button is switched off and the air is admitted into the chamber by using the leak valve located on the top of the sputter head.

After that, the glass work chamber can be taken off and the sputtered samples can be collected. The glass chamber is then cleaned with acetone for the next user before ending the experiment. The thickness of Au film is around 20 nm as measured by TENCO Profiler. The sputtering rate is closely related to the cleanliness of the sputtering system and the target used.

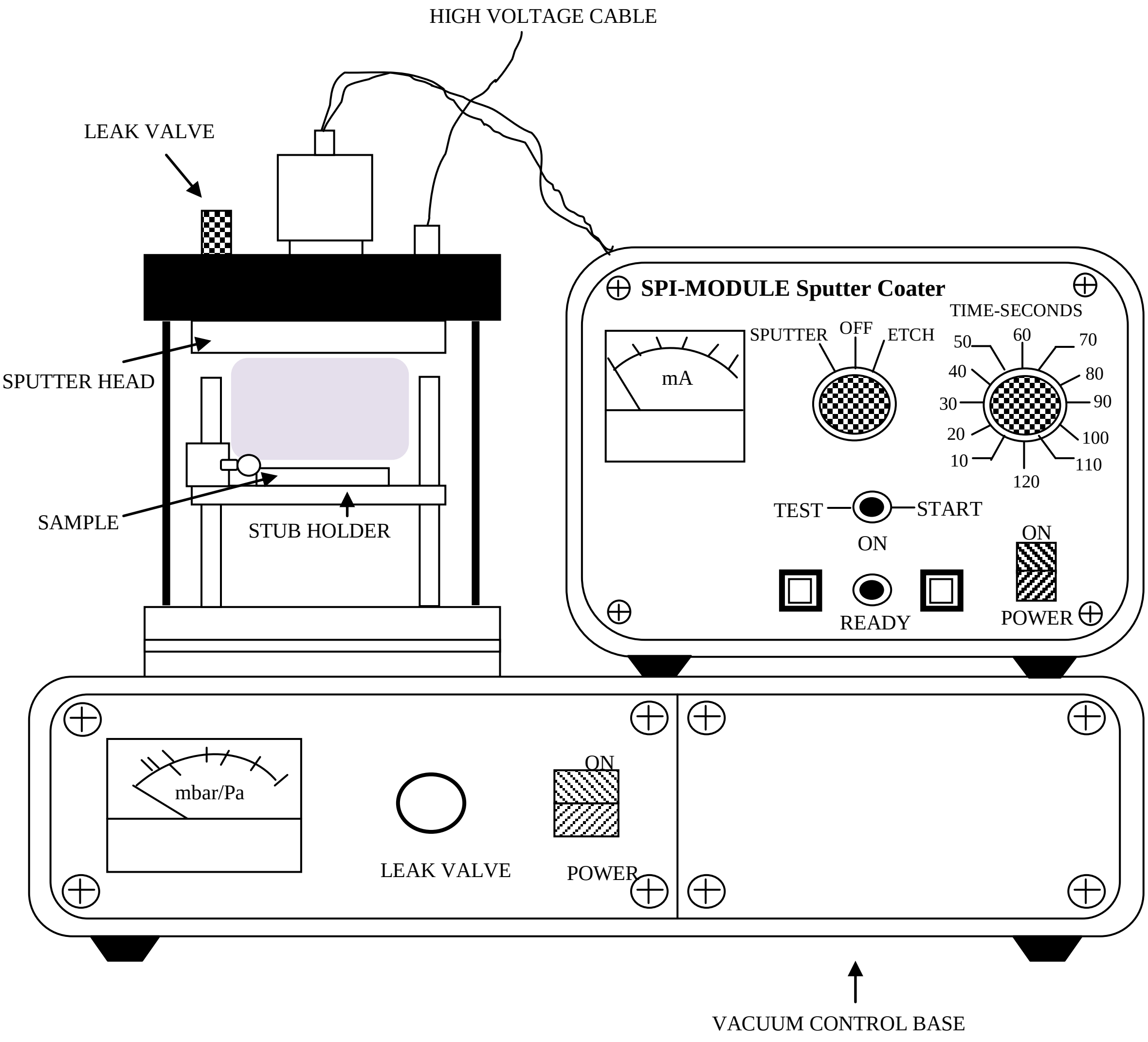

Figure 3.10: SPI-MODULE Sputter Coater

3.5.2 Hot Wire Evaporation Technique

In this work, thermal evaporation deposition technique using resistive element is adopted as an alternate method to prepare Au film. Helices tungsten wire (Edwards, A10 25) is used as a resistive element to evaporate the metal. Gold wire (99.999 %) is hung onto the middle part of the tungsten wire. High current is then passed through the tungsten wire, making it hot enough to evaporate Au. After that, the evaporated Au vapor will condense in the form of a thin film on the substrate surface and on the vacuum chamber walls. To achieve a more effective evaporation by avoiding reaction between the Au vapor and atmosphere, the process is carried out in low pressure conditions (10^{-3} mbar). In this way, the mean free path of Au vapor atoms is in the same order as the vacuum chamber dimensions, so these particles travel in straight lines from the evaporation source towards the substrate without any excess collision with contaminants *(Park & Rhee 2004)*. Most importantly, average energy of Au vapor atoms reaching the substrate surface is generally low (tenths of eV), leading to lesser or negligible damage on surface of substrates compared to DC sputtering technique which possesses highly energetic ions. For the Au preparation in this work, some parameters were fixed throughout the work. First, the distance between the tungsten wire and substrates is kept at around 15 mm. Second, the diameter and length of Au wire is fixed at 0.5 mm and 2 mm respectively. Third, the DC current is constantly set at 30 A.

The configuration of the thermal evaporation technique used in this work is shown in Figure 3.11 and Figure 3.12 with different settings. The substrates are placed below the tungsten filament, leading to the top-down configuration.

(a) Without Shutter

To begin the Au evaporation, the system is set up as shown in Figure 3.12. Then, the chamber is sealed and pumped down to around 10^{-3} mbar. The current to be supplied to the tungsten wire via two electrodes to around 30 A is set by controlling the voltage supplied from an IBC regavolt (0 to 240 V AC, 1kVA). The Au evaporation starts and runs for 5 minutes until the Au wire hung onto the tungsten wire is fully evaporated. The results obtained using this technique will be discussed in detail in Chapter 4.

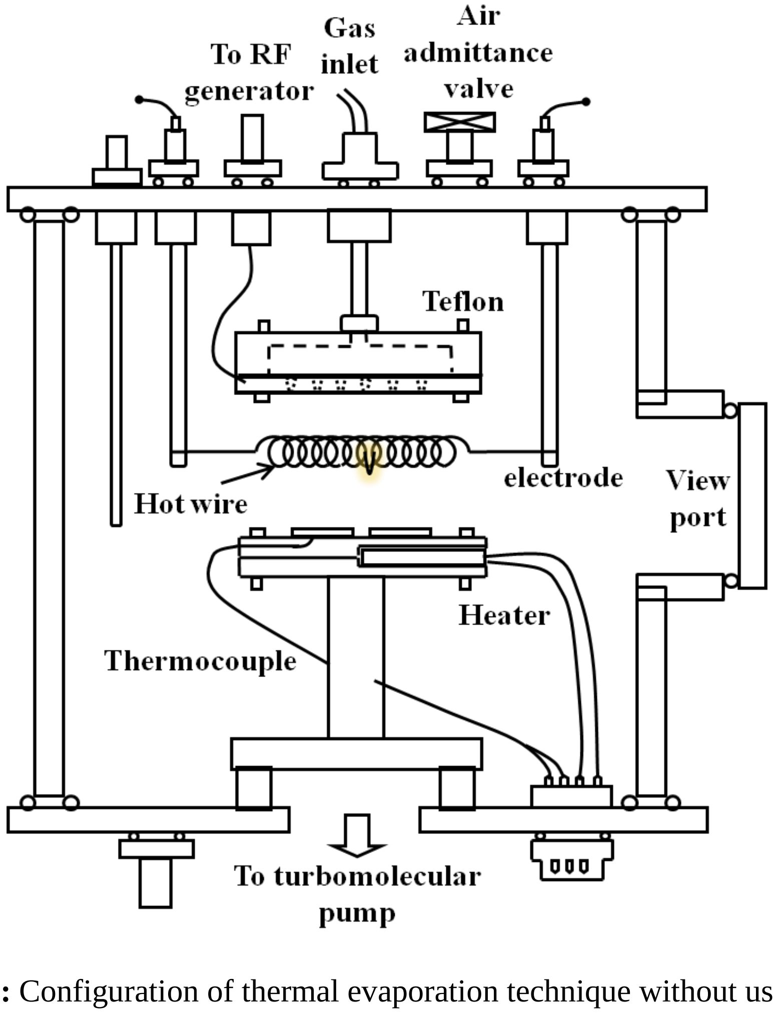

Figure 3.11: Configuration of thermal evaporation technique without using shutter

(b) With Shutter

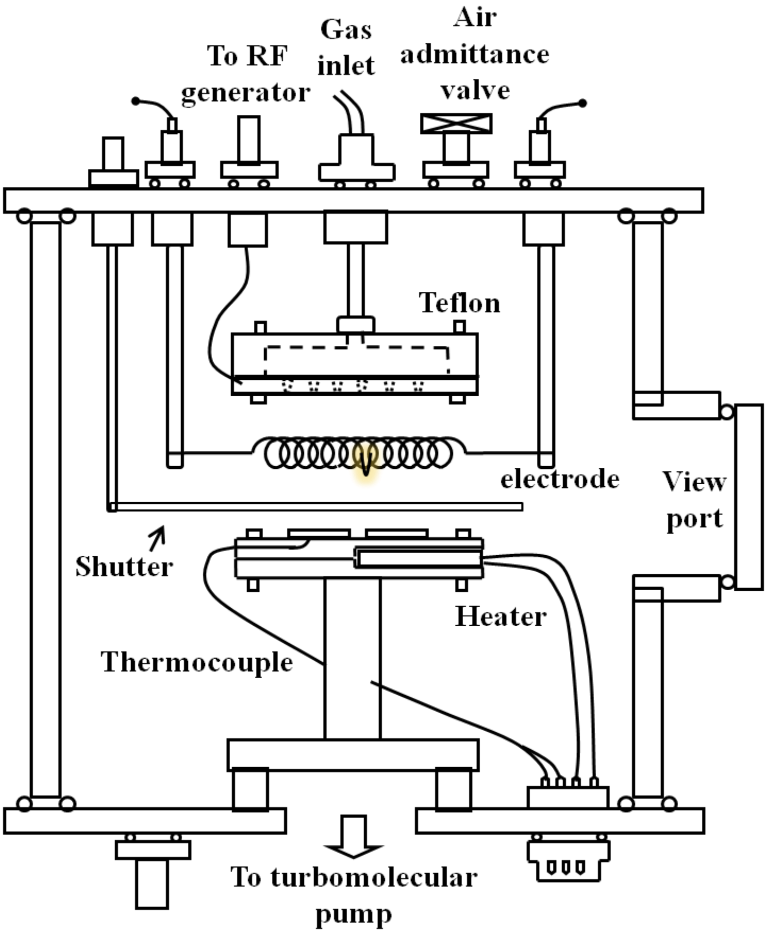

Figure 3.12: Configuration of thermal evaporation technique using shutter

To have a better control on the thickness of Au film and thus the morphological properties of Au particles, we modified the chamber by adding a shutter between the hot filament and substrates as shown in Figure 3.12. As the pressure reaches around 10^{-3} mbar, the current supplied to the tungsten wire to around 30 A is slowly increased and the timer for the evaporation process is started. The control of current can be done by varying the voltage supplied. Normally, bigger and heavier Au vapor droplets will fall downwards in the beginning of the evaporation process. Thus, shutter is closed in advance for 13 s. Then, shutter is opened for 3 s to allow the Au coating on the substrates. Shutter is closed immediately after 3 s of evaporation time. Then, tungsten wire is further heated for one minute to evaporate the

Au completely, making the tungsten wire clean. The evaporation time can be varied in order to yield Au film with different thicknesses. However, in my work, the evaporation time with using shutter is kept at 3 s. Au film with thickness of around 20 nm is measured using TENCOR profiler. The results obtained using this technique will be discussed in detail in Chapter 4.

3.6 Thermal Annealing Technique

Thermal annealing technique is used to heat up the as-prepared Au/SiO_x film to the desired temperature in order to induce the growth of Au NPs. In this way, the effect of morphological properties (size and shape) of Au NPs on the structural and optical properties of Au/SiO_x film can be studied thoroughly.

In this work, CARBOLITE Combustion Tube Furnace (model of CFM 12/1) is used to anneal the samples. The quartz tube is heated by resistance wire wound on a ceramic former. The schematic diagram of this furnace can be clearly shown in Figure 3.13. To start the process, a different position in the quartz tube is calibrated using a thermocouple to obtain the heat zone length before putting in the samples. For this CARBOLITE tube furnace, the length of the heat zone is around 50 mm in the middle of the quartz tube. Then, the samples are put on a crucible and inserted into the middle of the quartz tube by using a long k-type thermocouple connected to a thermometer. Flow the purified nitrogen gas with a flow rate of 50 sccm into the tube. The annealing process now is ready to start. Turn on the “POWER” switch and set to the desired annealing temperature. The temperature will increase gradually as displayed on the temperature indicator. As the desired temperature is achieved, 10 minutes heating is carried out to make sure the temperature inside the tube furnace is stable. After 10 minutes, annealing process starts. At the same time, press the “START” button of timer to determine the annealing time which can be varied for different work. However, the annealing time in this work is kept at 60 minutes. After 60 minutes, set the temperature to around room temperature (~ 34°C) and wait for it to cool down naturally. Samples and valve of nitrogen gas tank can be taken out and closed respectively when room temperature is achieved.

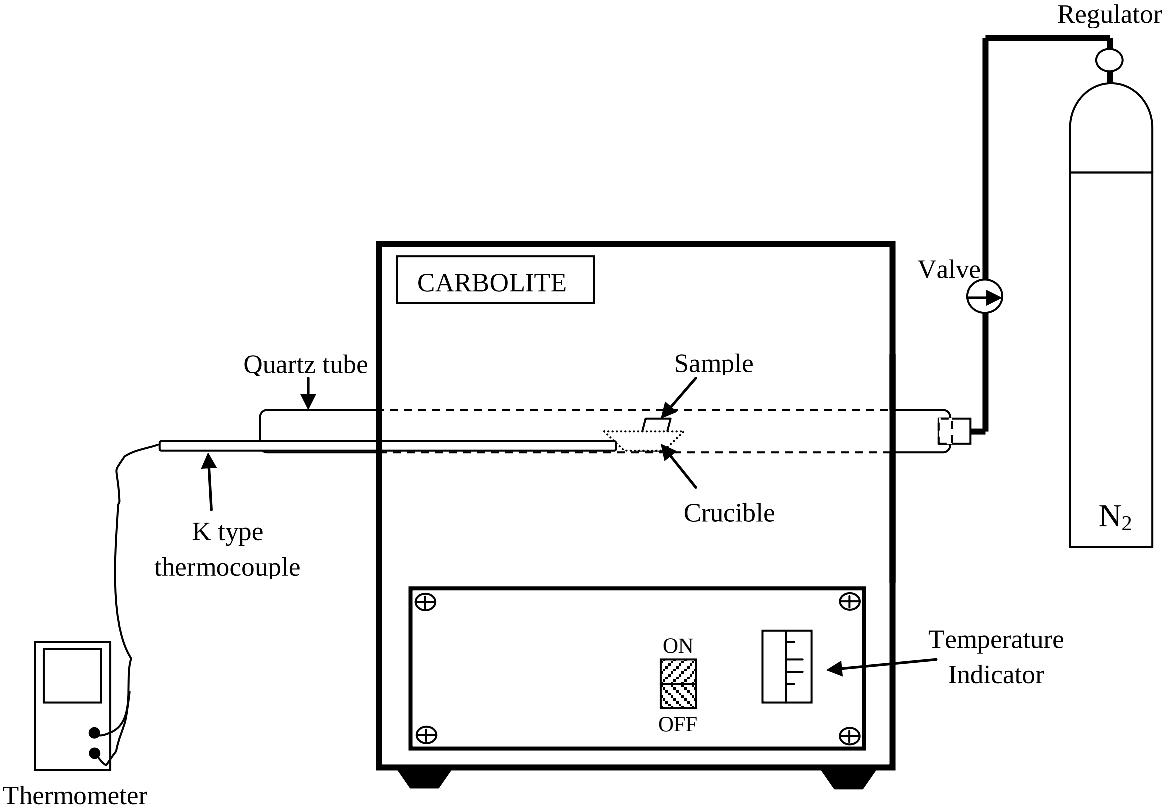

Figure 3.13: Schematic diagram of CARBOLITE Tube Furnace

3.7 Analytical Techniques

With the experimental technique to prepare the Au/SiO$_x$ films with different structure, we need an analytical technique to characterize the optical and structural properties of the samples in order to investigate into more detail towards their potential application in a certain field. In my work, there are four characterization instruments adopted which include field emission scanning emission microscopy (FESEM), Fourier transform infra-red (FTIR), X-ray diffractometry (XRD) and ultraviolet-visible-near infrared optical spectroscopy (UV-VIS-NIR). Besides the data obtained directly from these instruments, some calculation techniques are required to analyze these data more efficiently.

As mentioned in Chapter 3, Part 3.2, there are two different substrates deposited with Au/SiO$_x$ film in this work. They are *p*-type c-Si (111) and plain quartz substrates. Generally, it is known that the photons of light will be transmitted through the sample if the sample is irradiated with low energy photons which have not enough energy to break the covalent bonds. As the photon energy is increased above the band gap energy of the sample, the number of transmitted photons decreases due to the absorption of light in the bond-breaking process. Thus, the c-Si (111) substrate is only transparent to infrared light but opaque to visible light since the band gap energy of silicon is known to be 1.1 eV. On the other hand, quartz substrate is not only transparent to infrared light but also visible and ultraviolet light as quartz substrate has higher band gap energy closer to silicon dioxide. So, the films on quartz substrates are only used for optical analysis using UV-VIS-NIR spectroscopy. However, *p*-type c-Si (111) substrates are used for FTIR, FESEM and XRD analysis.

3.7.1 Field Emission Scanning Emission Microscopy (FESEM)

Field emission scanning emission microscopy (FESEM) is generally used to study the morphological properties of the thin films. It can capture very high resolution image at very high magnification, showing the particle in nanometer size. It is different with light microscope (LM) in terms of source used. LM uses light as a source whereas FESEM uses electrons as source. FESEM can be classified as a high vacuum instrument since it requires high vacuum condition (~10^{-7} Pa) during the measurement process in order to prevent discharge inside the instrument by reducing the mean free path of electrons and allowing electron movement along the column without scattering. The simplified internal structure of FESEM is clearly displayed in Figure 3.14.

Electrons in the form of a steady beam are liberated from an electron gun, which typically consists of one of two types. First one is the thermionic gun, which is very commonly used to apply electrical current to heat up the filament (e.g. tungsten). When the heat is high enough, the electron can escape from the filament material. However, thermionic gun has the disadvantage of low brightness and thermal drift during operation. Thus, another type of electron gun called field emission gun or cold cathode field emitter can be used to avoid these problems without heating up the filament. The field emission gun is usually a filament sharpened to a point or small tip. This sharp point can make the electric field concentrate to a very high level. In this way, a huge electrical potential gradient can exist which in turn pulls the electrons away from the filament material and accelerates it. On the other hand, the difference between the conventional SEM and FESEM is dependent on the type of electron gun used. FESEM is better than SEM as it provides a clearer image, improved spatial resolution and less electrostatic distortions and damage.

The electrons from filament material are then further accelerated and focused by two anodes. The first anode is used to limit the current while the second anode focuses and accelerates the electron beam. The accelerated electron beams are then condensed by the lenses made of magnets instead of glasses to produce a narrow scan beam that bombards the samples (Au/SiO$_x$) put in the sample chamber. It is believed that the narrower the beam, the higher the resolution can be achieved for FESEM. As the sample is bombarded with these energetic electron beams in both elastic and inelastic form, different electrons will be emitted such as X-rays, Auger electrons, secondary electrons, and backscattered electrons. Secondary electrons emitted from 200 Å within the sample are the most common signal detected by the electron detector. Image of the samples will then be constructed and displayed on a pc monitor.

For the sample preparation, make sure that the samples are clean, dried and properly mounted on a sample holder before loading them on to the specimen stage. It should be noted that the samples must be electrically grounded to the sample holder by using a conductive tape in order to minimize the discharge on the samples. If the sample studied is a poor or non-conductor, it must be coated with a thin conducting layer such as metal film prior to the FESEM measurement. In this work, FESEM with model of FEI Quanta 200 is used. The real image of this system is shown in Figure 3.15.

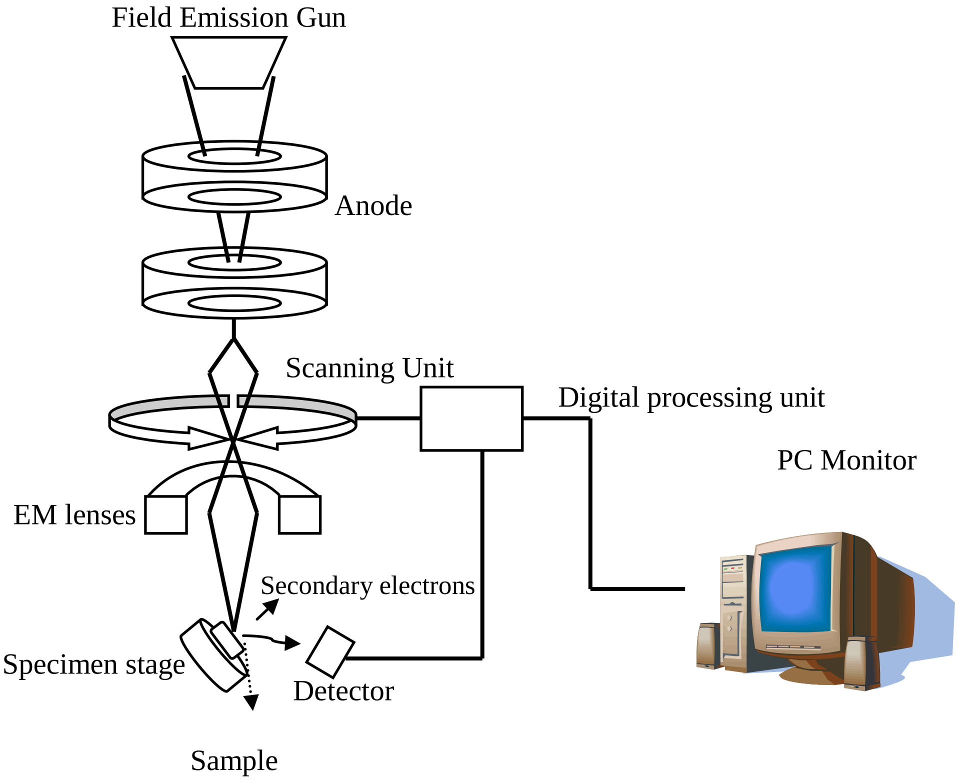

Figure 3.14: Simplified internal structure of FESEM

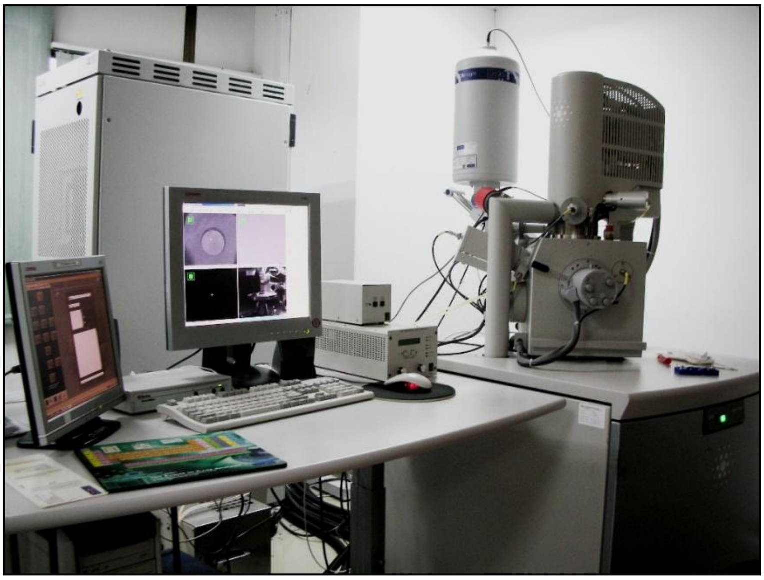

Figure 3.15: Real image of FESEM with model of FEI Quanta 200

3.7.2 Fourier Transform Infrared (FTIR)

Fourier transform infrared (FTIR) spectroscopy is a preferred non-destructive method of infrared spectroscopy. It can be used to identify the molecular structure in the deposited films and determine the local bonding environment of the constituent atoms. According to the equation of $E = hc/\lambda$ where E is energy of photon, h is Planck constant, c is the speed of light and λ is the wavelength of incident light, we can know that photons emitted from the infrared source carry lower energy compared to those photons that are emitted from visible and ultraviolet source. In infrared spectroscopy, the unit of measurement called wavenumber (cm^{-1}) is used. It represents the number of waves in one centimeter. Since the wavenumber is inversely proportional to the wavelength, it is directly proportional to the frequency and energy which make it more convenient to be used. Basically, the IR region can be divided into three regions: near IR, mid IR and far IR. The region most frequently used for chemical analysis is the mid-IR region range from 4000 to 400 cm^{-1}.

As we know, all molecules vibrate even at absolute zero temperature. If the frequency of specific vibration is equal to the frequency of incident electromagnetic radiation, the molecule will absorb the radiation, creating a molecular fingerprint of the sample. It means that no two unique molecular structures can have vibration at the same frequency like the characteristic of fingerprint. Determining these frequencies of vibrations between the bonds of the atoms making up the material can allow us to determine the bond that exists in the molecule. Normally, these frequencies lie within the region of infrared which is a region of lower energy than visible light. A higher energy of radiation will induce a molecular electronic transition instead of molecular vibration. In general, there are two types of vibrations called stretching and bending *(Kirk, 1988*). Stretching vibration involves the change in inter-atomic distance along bond axis. However, bending vibration involves the change in angle between two bonds. Generally, bending vibration can have different types of vibration consisting of rocking, scissoring, wagging and twisting vibration. Both the stretching and bending vibration of molecules are illustrated in Figure 3.16 as shown below.

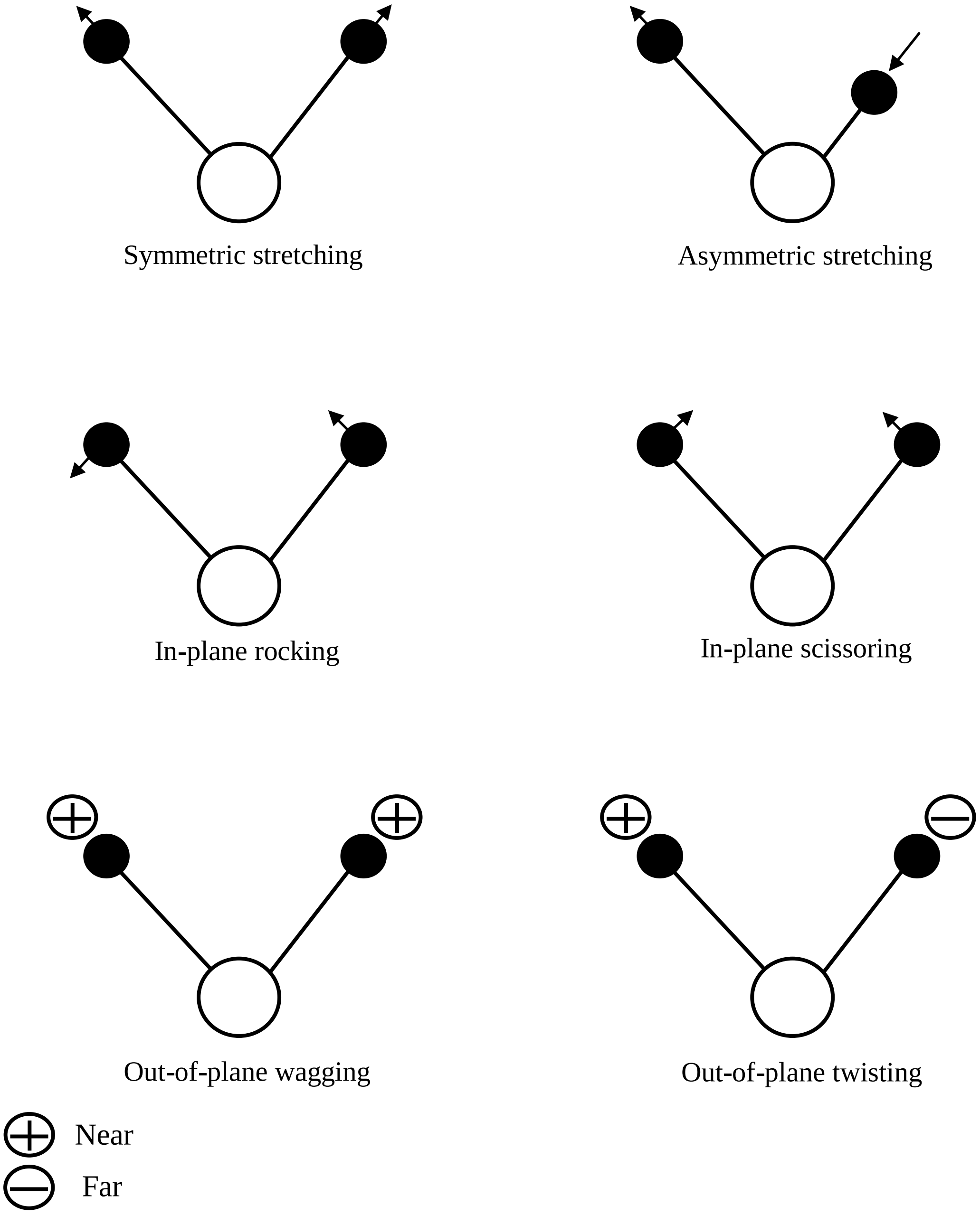
Symmetric stretching

Asymmetric stretching

In-plane rocking

In-plane scissoring

Out-of-plane wagging

Out-of-plane twisting

Figure 3.16: Stretching and bending vibration of molecules

An IR spectrum with wavenumber as x-axis and transmittance percentage as y-axis is used to present the IR absorption information. Transmittance, *T*, is the ratio of radiant power transmitted by the sample (*I*) to the radiant power incident on the sample

(I_o). Absorption band of molecular vibration is therefore represented by a “trough” in the curve. Band intensities can also be expressed as absorbance (A). Absorbance (A) is the logarithm to the base 10 of the reciprocal of transmittance (T) where $A = \log_{10}(1/T) = -\log_{10} T = -\log_{10}(I/I_o)$. However, transmittance is a better indicator by providing better contrast between intensities of strong and weak bands. The reason for this is the transmittance range from 0 to 100%, whereas absorbance can even range from infinity to zero. It should be noted that if the molecule consists of two identical atoms such as O_2 and N_2, there will not be any absorption band existing. It can be explained by the fact that the intensity of the absorption band is dependent on the change in dipole moment of bond and number of specific bonds exists. Also, charge difference is believed to affect the dipole moment of bond. Therefore, identical atoms having no charge difference can result in no photons being absorbed and thus no excited vibrational state being reached for absorption.

Furthermore, during the measurement process, a background spectrum must be measured prior to measurement of sample since there needs to be a relative scale for the absorption intensity. This is normally a measurement with bare substrate in the beam. In my work, the bare substrate is c-Si (111). This can be compared to the measurement with sample in the beam to determine the percentage transmittance. This process is important for removing the entire instrumental characteristic in order to make sure the spectra features only come from the samples.

Fourier transform infrared spectroscopy (FTIR) system used in this work is the model of Perkin-Elmer System 2000. Samples were scanned in the range of 4000 to 400 cm^{-1} with resolution and interval of 4 cm^{-1} and 0.5 cm^{-1} respectively. The number of scans varies from 10 to 50. The real image of the system is shown in Figure 3.17.

Figure 3.17: Real image of Fourier transform infrared (FTIR) spectroscopy system 2000

3.7.3 X-ray Diffraction (XRD)

X-ray diffraction (XRD), which can be observed as the incident beams of X-rays, is about the same wavelength as the inter-atomic distance, which interferes with one another when they leave the atomic planes of a crystal. Thus, X-ray crystallography, a non-destructive technique using XRD phenomenon, is commonly used to determine the average spacing, d between layers or rows of atoms, orientation of a single crystal or grains, crystal structure of an unknown material, size, shape and internal stress of small crystalline regions *(Coscia et al., 2003; Zhao et al., 2005)*. The schematic diagram of incidence and reflection of X-ray beam by the atomic planes of a crystal is presented in Figure 3.18. It should be noted that diffraction only occurs when Bragg's law is satisfied, meaning that diffraction of waves only occurs at certain angles called Bragg angles, where the wave patterns of the beam leaving the atomic planes are in phase (constructive interference). Bragg's law was developed by Bragg in 1914 and can be expressed as $n\lambda = 2d\sin\theta$, where n is an integer in order of diffraction, λ is the wavelength of incident X-ray beam, d is the spacing between atomic layers in crystal and θ is the angle of incidence and reflection of incident ray *(North 2010)*. In most cases, the first order of diffraction, where $n = 1$ is used. Therefore, the spacing in the crystal planes of Miller Indices (*hkl*) can now be determined using Bragg's law.

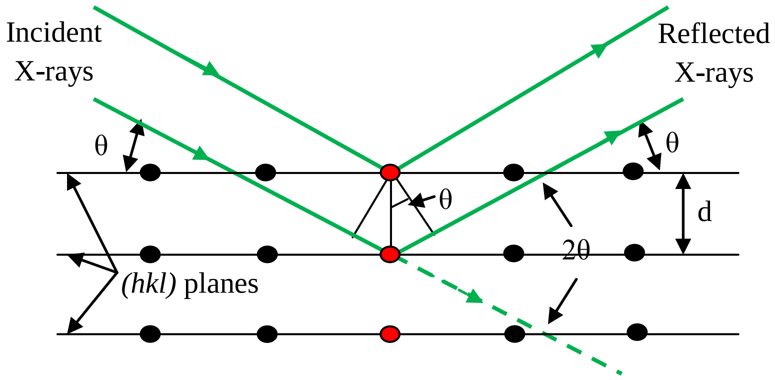

Figure 3.18: Schematic of incidence and reflection of X-ray beam by the atomic planes of a crystal.

With the known spacing between two closest parallel planes with the same Miller Indices, the lattice constant between two unit cells in cubic crystal structure can be determined using equation of $a_o = d_{hkl}/(h^2 + k^2 + l^2)^{½}$. This equation can be used together with XRD data to determine if a sample is face-centered cubic (FCC) or body-centered cubic (BCC) structure. It is important to know that, for BCC structure, diffraction occurs only on crystal planes where Miller Indices when added together (h+ k+ l) total an even number. For FCC structure, the Miller Indices must be either all even or all odd (zero is considered even) for the diffraction peaks to appear in the XRD pattern. For example, Au has the FCC structure with diffraction peak of Au on the orientation plane of (111), (200), (220), (311) and (222).

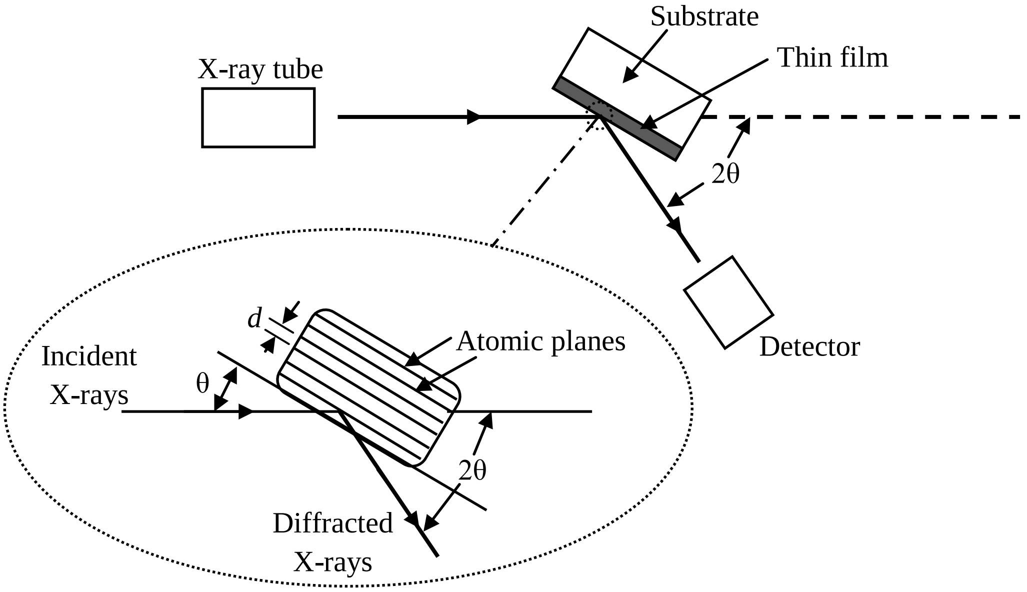

Figure 3.19: Basic features of typical X- ray diffractometer

The basic features of a typical X-ray diffractometer are shown in Figure 3.19. XRD pattern of the sample is detected by a detector and displayed in PC monitor. Different diffraction peaks can be observed in XRD pattern if the sample is crystal structure. The diffraction peak will show broadening because of particle size and strain. Thus, the average size of crystallites can be estimated from the observed line broadening as shown in Figure 3.20. According to Scherrer's equation *(Devadason & Muhamad, 2007)*, crystallite or grain size can be easily estimated using the expression of $D = 0.9\,\lambda / B \cos\theta$ where λ is the X-ray wavelength, θ is the Bragg diffraction angle and B is the full-width at half-maximum (FWHM) in unit of radian. The Scherrer's equation is normally adopted when crystallite size is smaller than 100 to 200 nm as the appreciable broadening in x-ray diffraction lines will occur.

In this work, Siemens Diffractometer D5000 is used. The real image of this characterization instrument is shown in Figure 3.21. This high precision diffractometer is useful for both powder and bulk materials. Data collection is performed under computer control using the "Diffrac Plus" software application. The step time and step size can be varied in XRD measurement to obtain more accurate data.

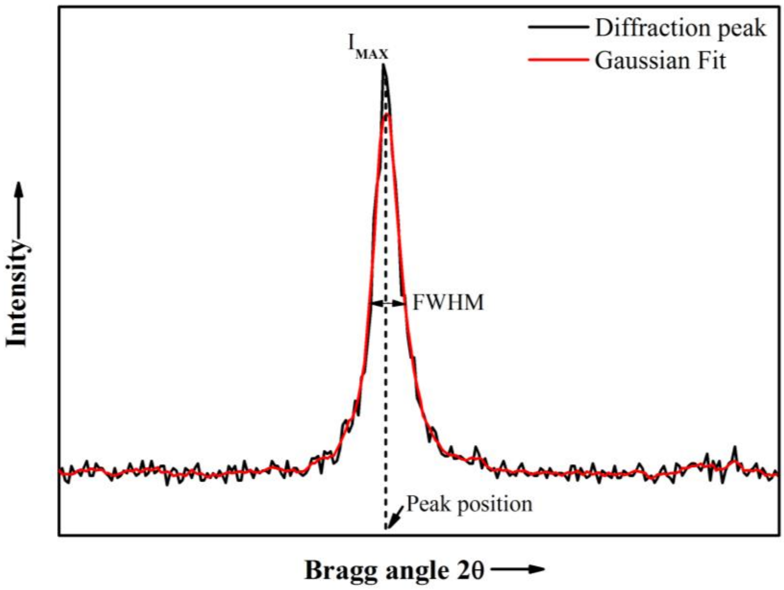

Figure 3.20: Analysis of peak shape in XRD (peak position, peak width and peak intensity)

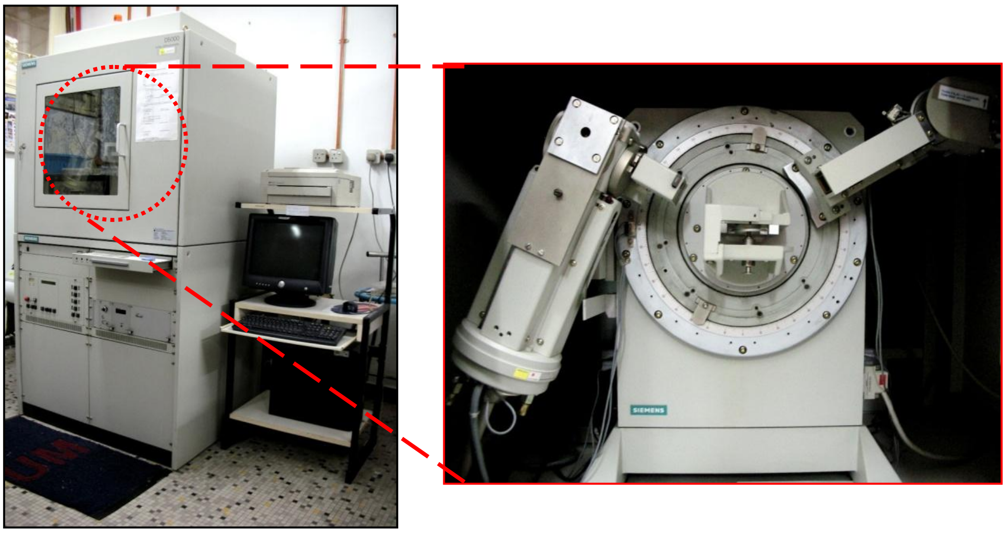

Figure 3.21: Real image of Siemens Diffractometer D5000

3.7.4 Ultraviolet-Visible-Near Infrared (UV-VIS-NIR)

Ultraviolet-visible-near infrared (UV-VIS-NIR) spectroscopy is an important analytical technique for the qualitative and quantitative study of optical properties of thin films. UV-VIS-NIR spectrophotometer is widely employed as it is simple, versatile, fast, accurate, and cost-effective. The operation mechanism of this technique is based on the interaction between light and matter. It is well known that EM radiation with different energy emitted at any particular wavelength is dependent on the temperature of the sample. It can be well explained with blackbody radiation, which indicates that the wavelength of maximum energy shift to lower wavelength as emitted energy increases with temperature. Therefore, more recently, it has become common to use tungsten halogen lamp and deuterium discharge tube as sources for visible-near infrared and ultraviolet region, respectively.

By using this spectrophotometer, interesting region in electromagnetic (EM) spectrum range from 190 to 2500 nm (UV-VIS-NIR region) can be fully investigated. Unlike IR region which possesses lower energy due to the longer wavelength, shorter wavelength region detected by spectrophotometer induces the electronic transition to higher energy level of bonding and non-bonding electrons of the ions and molecules. This in turn results in the absorption of EM radiation by the samples. Theoretically, it should be expected that absorption spectrum of a sample should show a few very sharp lines since the absorption is known to occur when the incident photon having energy, exactly match the energy required to excite an electronic transition. However, absorption spectrum of sample is experimentally observed to consist of a few humps rather than sharp lines, showing the absorption occurs over a wide range of wavelengths. This phenomenon can be attributed to the fact that an electronic transition is usually accompanied by a simultaneous change between other vibrational and rotational energy states. It means that no pure electronic transition can occur in reality.

In this work, JASCO UV-VIS-NIR double beam spectrophotometer with model of V-570 is used. It provides the wavelength range from 190 to 2500 nm. Wavelength scanning speed can be varied from 10 to 4000 nm/min. The optical system of model V-570 is shown in Figure 3.22.

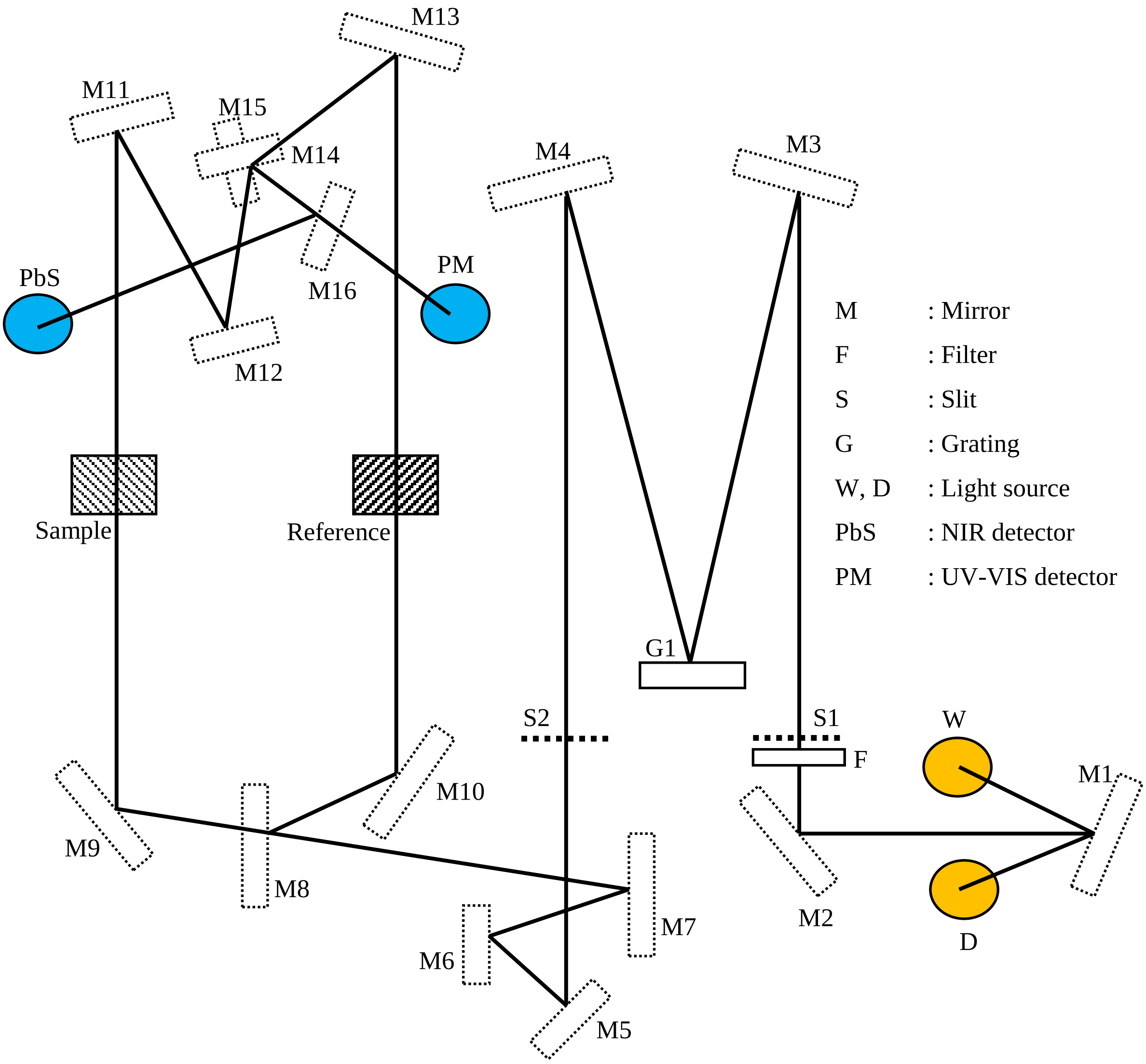

Figure 3.22: Optical system of JASCO UV-VIS-NIR spectrophotometer with model of V-570

As shown in Figure 3.22, it is clearly observed that the light from light source of UV or VIS/NIR region is converged and enters the monochromator. The grating in the monochromator then will disperse the light to pass through the exit slit. This monochromatic light is split into two light paths by a sector mirror, one incident on the sample to be measured while another on the reference sample. The light that has passed through both sample and reference is incident on the photomultiplier tube or PbS photoconductive cell. Then, the detected light will be converted into an electrical signal in digital form after being synchronously rectified. The signal finally will be displayed as spectrum in PC monitor. The real image of JASCO UV-VIS-NIR V-570 spectrophotometer used in this work is shown in Figure 3.23.

Figure 3.23: Real image of JASCO UV-VIS-NIR V-570 spectrophotometer

For the analysis of data obtained from the optical spectrum, first we can choose the photometric mode that we want for the spectrum displayed. It can be Abs, T% or R%. T% is the transmittance expressed in percentage by dividing the intensity of light passing through a sample I to the intensity of light before it passes through the sample I_o. Abs is absorbance based on the transmittance where $A = -log\frac{T\%}{100\%}$. R% is the reflectance in percentage obtained from the ratio of intensity of light reflected from a sample to the intensity of light reflected from a reference material.

Then, the absorption coefficient, α of the films can be determined from both the transmittance and reflection spectra using the equation of *(Al-Kuhaili,2008)* $T = (1-R)e^{-\alpha d}$, where $\alpha = \frac{1}{d} ln\left(\frac{1-R}{T}\right)$ and d is the thicknesses of the samples which can be determined by the depth proofing using TENCOR Profiler. The calculated absorption coefficient is very important in this work to determine the existence of surface Plasmon resonance (SPR) peak exhibited by the sample (Au/SiO$_x$). From here, the optical energy gap, E_G of the samples can be evaluated from the absorption coefficient based on the Tauc relation *(Tauc 1972),* $\alpha E = B(E - E_G)^{\varphi}$, where B is a constant, E is photon energy, φ = ½ for direct allowed transition and φ = 2 for indirect allowed transition.

CHAPTER 4

RESULTS AND DISCUSSION

4.1 Introduction

As mentioned earlier, in this study, samples were prepared using two different techniques i.e. physical vapor deposition (PVD) technique and chemical vapor deposition (CVD) technique. In the first part, samples prepared by PVD technique will be discussed. Two different structures i.e. “supported ON” structure and “embedded IN” structures will be studied. The “supported ON” structures will be emphasized and samples preparation will be focused on CVD technique. The detailed explanation will be discussed later. For gold (Au) film deposition, DC sputter coater is a conventional method to prepare a very thin Au layer. In this work, hot wire evaporation technique was proposed to prepare Au layer. However, Au NPs formed without shutter attached below the hot wire were observed to be of non-uniform size and distribution. The situation is improved with the shutter attachment. The results obtained were very interesting to be observed which will be discussed in detail later. In this way, a better control on size of Au NPs can be achieved. The detailed flow chart of the work can be observed in Figure 4.1.

The results will be illustrated based on four different characterization instruments, i.e. Fourier transform infrared (FTIR) spectroscopy, field emission scanning emission microscopy (FESEM), X-ray diffractometry (XRD) and ultraviolet-visible-near infrared (UV-VIS-NIR) spectrophotometer. The structural properties of the Au/SiO$_x$ films were determined from the FTIR spectra and morphological images of FESEM while XRD spectra were used to study the crystalline nature of the samples. The optical properties of the samples were studied from the transmittance and reflectance spectra. Position and intensity of surface Plasmon resonance (SPR) peak induced by Au NPs can thus be determined from these spectra.

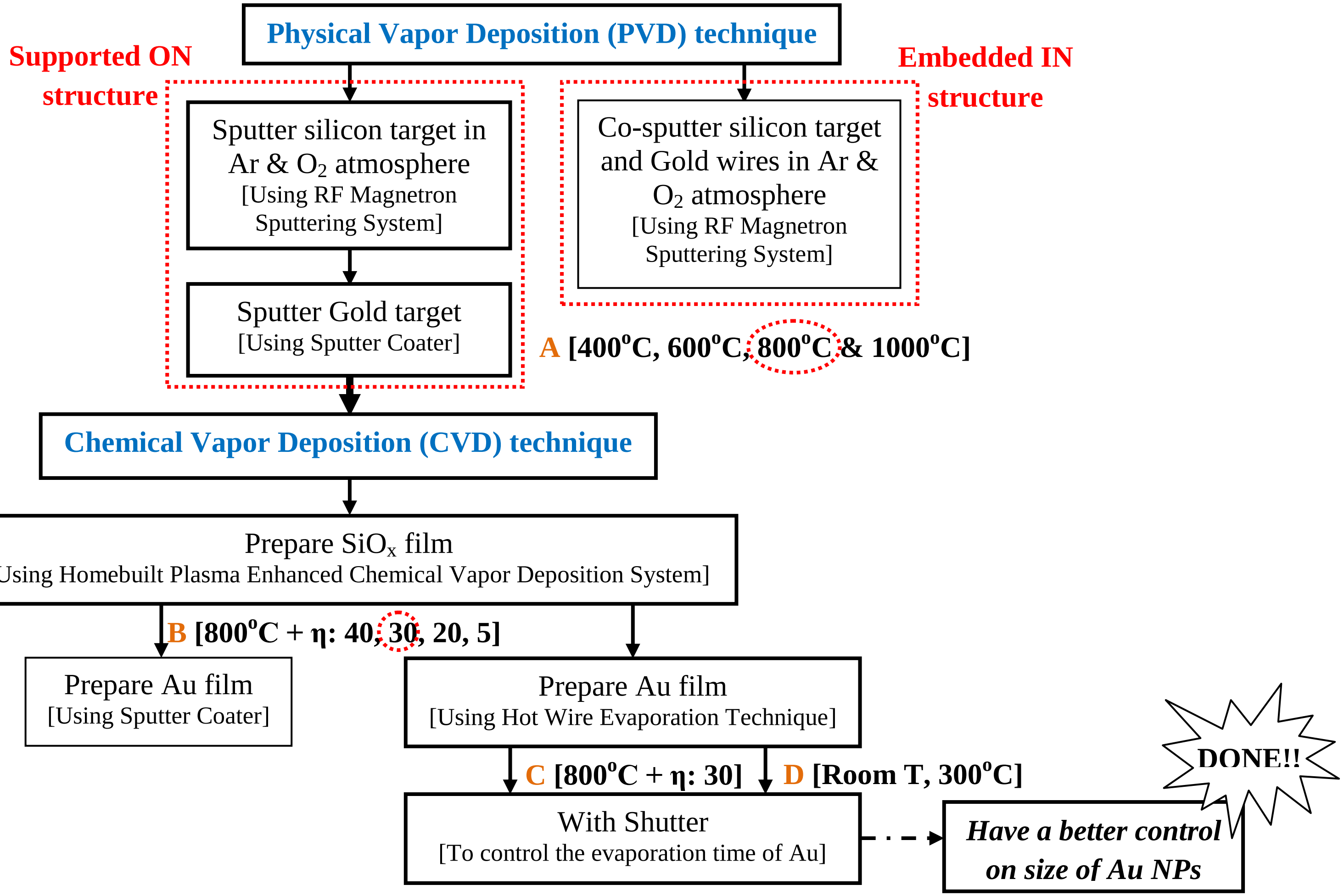

Figure 4.1: Flow chart of my experimental work

A. Study the effect of annealing temperature on growth of Au NPs

B. Study the effect of flow rate ratio of N_2O/SiH_4 (η) on the growth of Au NPs

C. Study the role of SiO_x to the growth of Au NPs

D. Study the Au NPs evaporated on heated SiO_x film

4.2 Physical Vapor Deposition (PVD) Method

4.2.1 Introduction

In this sub-chapter, samples will be prepared using physical vapor deposition (PVD) technique. Two different structures of Au/SiO_x film will be investigated. First, SiO_x film will be prepared by using RF magnetron sputtering system prior to the Au preparation using DC sputter coater to produce "supported ON" (Au ON SiO_x film) structure. Second, silicon and gold target will be co-sputtered using the RF magnetron sputtering system with the presence of argon and oxygen gases to produce "embedded IN" (Au IN SiO_x film) structure. The as-deposited samples prepared by both techniques will be post-thermal annealed at different annealing temperatures for 1 hour in N_2 ambient. The effect of annealing temperature on the growth of Au NPs will be studied for the samples prepared by both methods.

4.2.2 Supported ON Structures

(a) ***Field Emission Scanning Emission Microscopy (FESEM)***

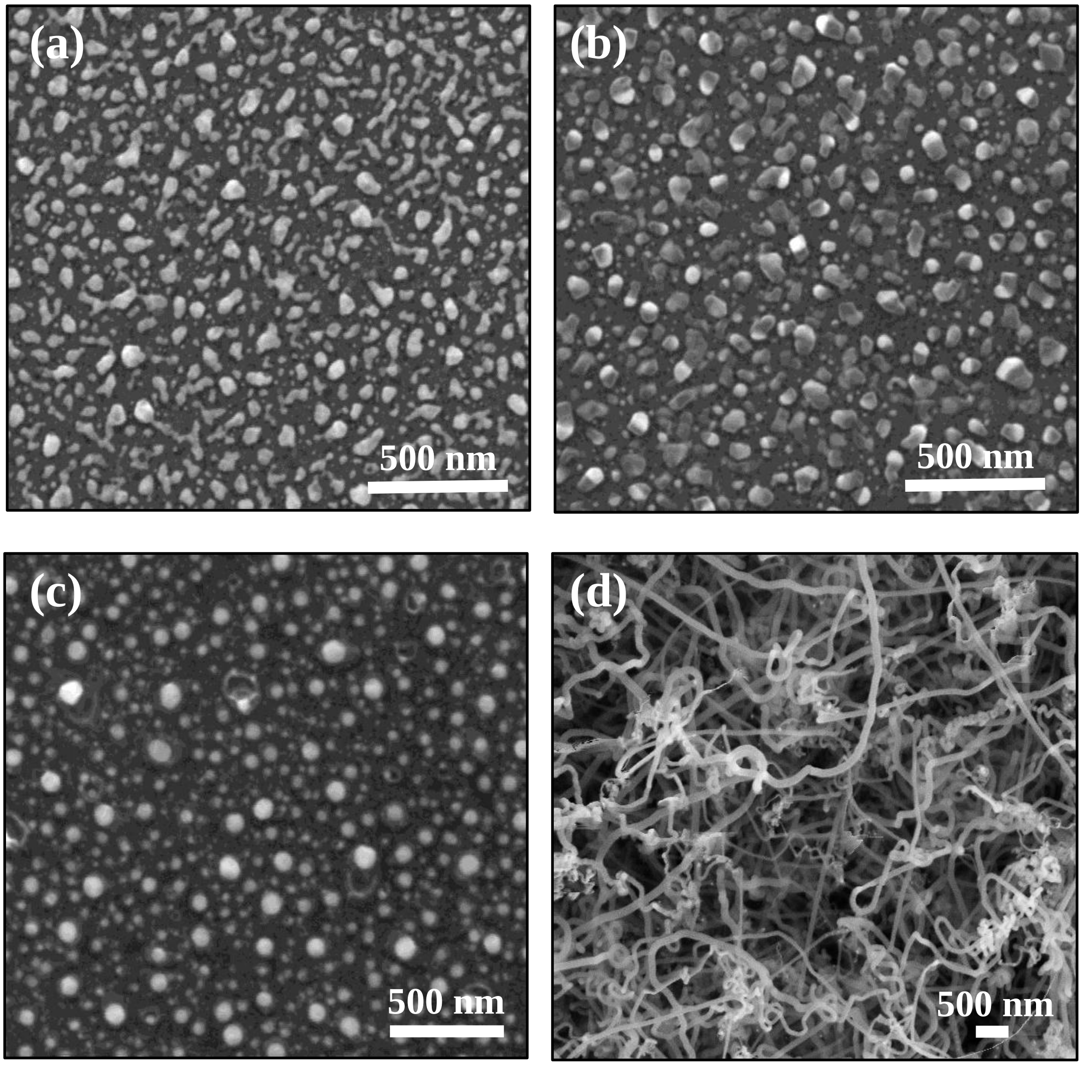

Figure 4.2: SEM images of the samples annealed at different temperatures: (a) 400 ℃, (b) 600 ℃, (c) 800 ℃ and (d) 1000 ℃

Figure 4.2 presents the FESEM images of the samples deposited on c-Si substrates and annealed at different annealing temperatures. These annealed samples consist of Au particles (white dots) and an amorphous SiO_x matrix (dark gray) for the samples annealed at temperatures below and equal to 1000 ℃. In the figure labeled (a), the sample demonstrates that a uniform dispersion of elongated and island-like Au particles agglomerate within the SiO_x matrix at an annealing temperature of 400 ℃. Generally, the Au particles form because of the small amount of kinetic energy is gained by sputtered Au atoms at low temperature, leading to a slow diffusion rate and mobility *(Yu et al., 2005).* The average diameter of the Au particles is about 60 nm. It is apparent that in most of the cases, Au particles start to melt at this temperature due to the lower melting point (363 ℃) of the Si/Au alloy eutectic point. However, at an annealing temperature of 600 ℃, agglomeration of Au particles lessens, and some of the Au particles have enough kinetic energy and mobility to aggregate with each other, forming Au particles with non-uniform size and irregular shape, as shown in Fig 4.2(b). The average diameter of these Au particles is still about 60 nm. With further increment of the annealing temperature to 800 ^{o}C, spherical-like Au particles with uniform distribution appear on the sample surface as observed in Figure 4.2(c), as a result of excessive kinetic energy was supplied to the Au NPs.

In addition, it is interesting to observe that the sample produces nanowires when the annealing temperature reaches 1000 ℃, as displayed in Fig 4.2(d). These nanowires are closely packed together, and all of the nanowires are non-aligned with an average length and diameter of around 5 μm and 160 nm, respectively. Energy-dispersive X-ray spectroscopy (EDX) results show that the composition of these nanowires consist of silicon (43 atomic %) and oxygen (57 atomic %) content, with a small amount of gold (0.08 atomic %) present on the tip of the nanowires. The composition percentage of silicon, oxygen and gold are slightly different at different spot of nanowire. The Au particles have played the role as metal catalysts for the growth of nanowires. However, the nanowires formation mechanism is rather different from the vapor-liquid-solid (VLS) processes, which require a source material and an evaporation technique (Th and et al., 2006). In this work, it is deduced that the possible source for the formation of nanowires could be due to the presence of the c-Si substrate, indicating the formation mechanism of NWs follows the SLS process. In general, the melting point of pure Au and Si are 1063 ℃ and 1414 ℃, respectively, whereas the eutectic point of the Si/Au alloy has a melting point of only 363 ℃. This lower temperature has indicated that the formation of nanowires can be grown easily from films annealed at 1000 ℃.

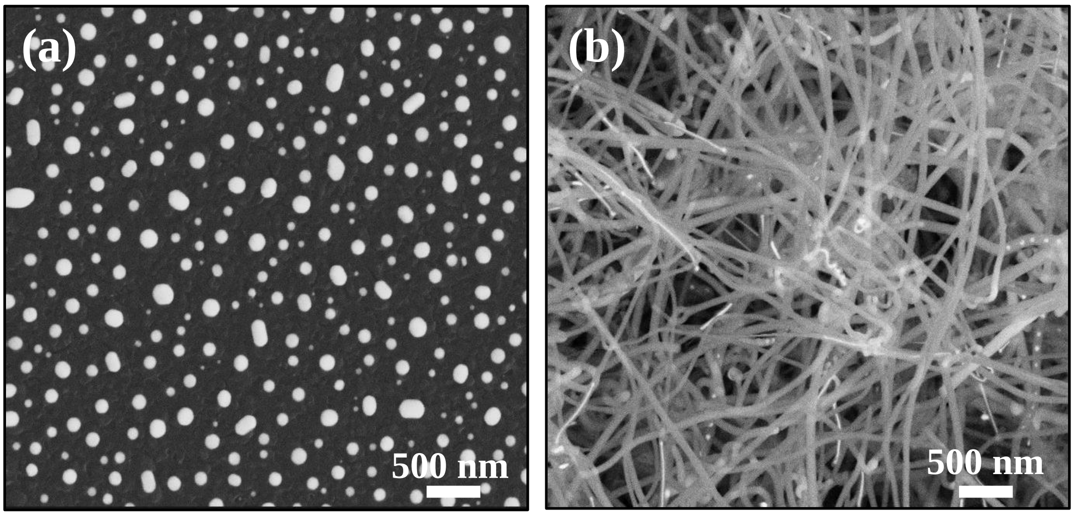

Figure 4.3: SEM images of the samples annealed at different temperatures: (a) 900 ℃, (b) 1100 ℃

In order to study the growth of NWs in details, the as-prepared Au/SiO$_x$ films were annealed at temperature of 900 ^{o}C and 1100 ^{o}C with identical process parameter and condition. The results are presented in Figure 4.3. At 900 ^{o}C, more uniform and larger size of spherical Au particles is found to disperse uniformly on the surface of SiO$_x$ film without any nanowires being formed yet. Nevertheless, more close-packed and aligned nanowires are observed on the film as the annealing temperature is further increased beyond 1000 ^{o}C up to 1100 ^{o}C, as shown in Figure 4.3(b). In addition to the increase of oxygen concentration, the increase of the temperature to 1100 ^{o}C also introduces well-aligned and longer nanowires. Furthermore, these phenomena suggest that nanowires interact actively with oxygen atoms in the SiO$_x$ film in order to form silica nanowires.

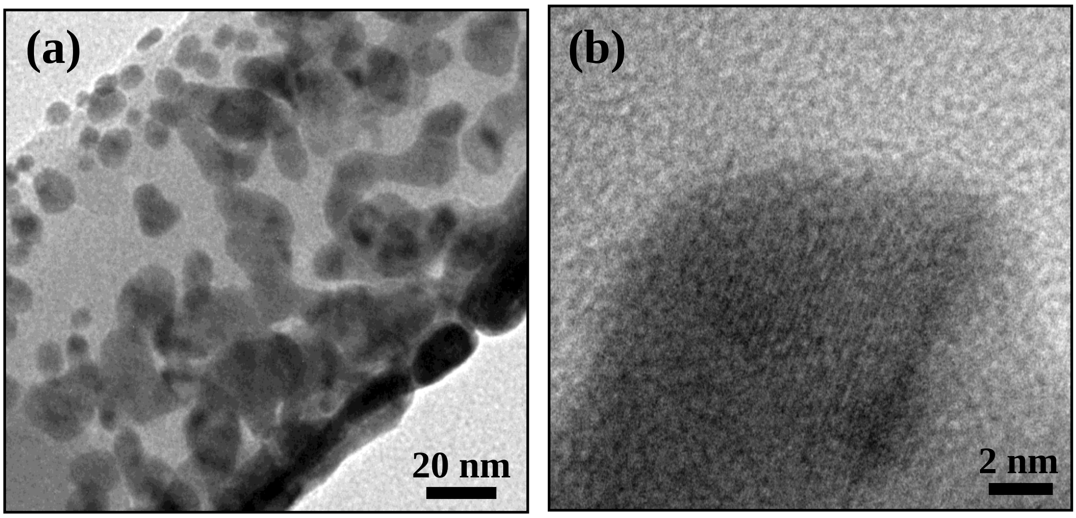

Figure 4.4: Plane-view (a) TEM and (b) HRTEM images showing the nanostructures of samples annealed at 1000 ℃.

For TEM inspection, samples were prepared by transferring some of the thin film structures onto TEM grids with a lacey carbon film (Agar scientific, S166N4 - 400 mesh). Figure 4.4 shows TEM and HRTEM images of the sample annealed at temperature of 1000 ℃. Figure 4.4(a) shows a typical TEM image of a single nanowire. The surface of nanowire is covered with different particles and nanostructure shapes, which may be of Au. These NPs and nanostructures indicate a non-uniform distribution over the entire nanowire surface, and some of the NPs and nanostructures overlap and accumulate at the side of the nanowire. The HRTEM image taken from a small part of the single nanowire for the sample annealed at 1000 ℃ is shown in Figure 4.4(b). As shown in the figure, a clear lattice plane of embedded Au NPs in the amorphous matrix of silicon oxide can be clearly observed which indicates that the Au catalysts in the growth of nanowires at 1000 ℃ are in the crystalline structure.

(b) Fourier Transform Infrared (FTIR)

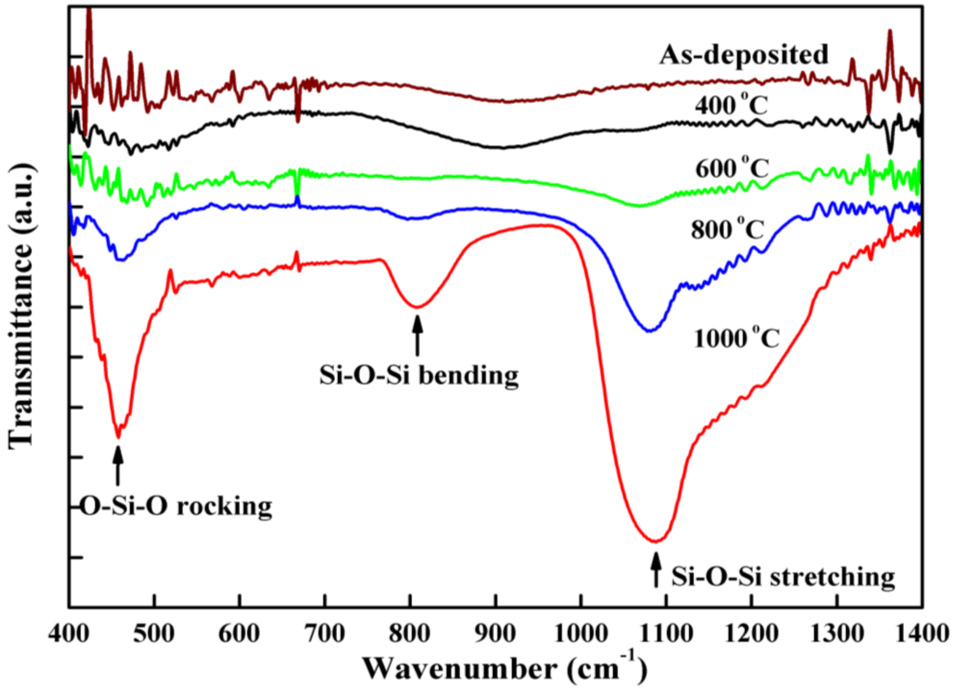

Figure 4.5: FTIR spectra of samples annealed at different temperatures

The IR transmittance spectra of the samples were analyzed by introducing the disorder-induced mechanical coupling between the optically active oxygen asymmetric stretch (AS) and the inactive oxygen asymmetric stretch (I-AS) modes in terms of the transverse-optic (TO) and longitudinal-optic (LO) vibrational modes, as indicated by Kirk *(Kirk 1988)*. The FTIR spectra of the samples annealed at different temperatures can be seen in Figure 4.5. In the spectra, there are three regions of absorption bands, located at 460 cm^{-1}, 816 cm^{-1} and 1080 cm^{-1}, which correspond to the rocking, bending and stretching vibrational modes of Si-O-Si bands, respectively.

All of the absorption peaks are TO modes that can be characterized in terms of particular vibrational modes of the oxygen atoms with respect to the silicon atoms pairs to which they are bonded *(Kirk 1988)*. LO mode is paired with each TO mode, and the frequency of the LO mode is, in general, higher than that of the TO mode. However, LO modes such as 507 cm^{-1}, 820 cm^{-1}, 1160 cm^{-1} and 1256 cm^{-1} are not observed in these spectra because they do not interact directly with light unless being observed in oblique-incidence absorption spectra using p-polarized light, due to the Berreman effect *(Berreman, 1963)*. In the figure, the spectra clearly demonstrates that the TO absorption peaks are significantly dependent on the annealing temperature. The bending absorption peaks start to appear at annealing temperatures above 600 ℃. The stretching absorption peak also becomes narrower and increases in intensity as the annealing temperature is increased to 800 ℃. The absorption peak somewhat shifts to 1088 cm^{-1} and increases in intensity when the annealing temperature is further increased to 1000 ℃. The relatively lower concentration of SiO_x in the samples at lower annealing temperature arise from the fact that the characteristics of the silicon oxide layer on the samples have been suppressed by the elongated and larger island-like Au particles. Increasing the annealing temperature up to 800 ℃ or above induces the formation of nanostructures or nanowires on the samples by supplying more heat and energy to the particles. Therefore, lack of suppression by the elongated and larger particles contributes to the introduction of oxide bonded to silicon atoms at higher annealing temperatures, even from SiO_x or from air.

The presence of broad shoulders in the stretching absorption peak centered at 1200 cm^{-1} can be observed in Figure 4.6 for the samples annealed at 1000 ℃. The broad shoulders are attributed to the AS motion in which O atoms move back and forth along a line parallel to the axis through the two Si atoms, giving rise to two vibrational modes *(Kirk, 1988; Niu et al., 2007)*. The 1088 cm^{-1} peak is regarded as a contribution of AS modes in which the adjacent O atoms execute the AS motion in-phase with each other. However, I-AS mode in which adjacent O atoms execute the AS motion 180° out-of-phase with each other attributes to the 1200 cm^{-1} peak. This can be clearly seen in Figure 4.7 after curve fitting is carried out. The TO AS and TO I-AS absorption peaks of 1088 cm^{-1} and 1200 cm^{-1} are consistent with the results obtained by Kirk, which is about the study of the oxide layer on a silicon wafer *(Kirk, 1988)*. These demonstrate that the outer oxide layer on the nanowires grown in this work is similar to that of the oxide layer on a silicon wafer, indicating that the nanowires grown at 1000 ℃ contain an outer oxide layer on the surface.

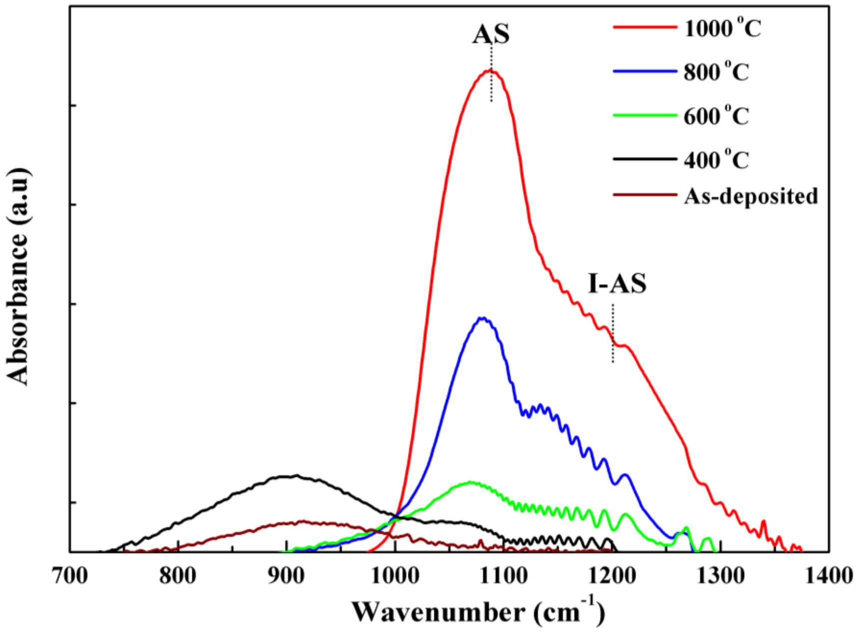

Figure 4.6: Si-O-Si stretching peak with absorption mode at different temperatures: 400 ℃, 600 ℃, 800 ℃ and 1000 ℃

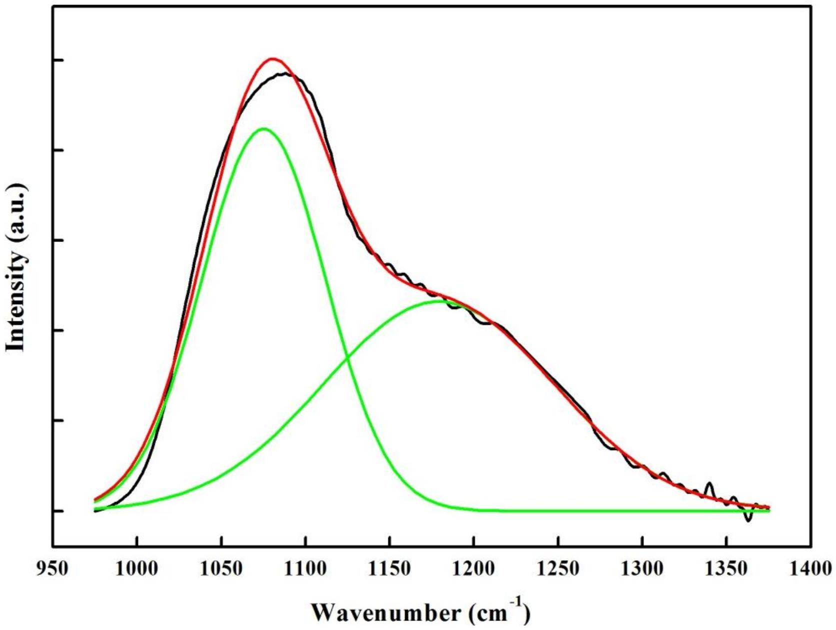

Figure 4.7: Curve fitting on the Si-O-Si stretching peak with absorption mode at annealing temperatures of 1000 ℃.

In addition, by applying the central force model *(Niu et al., 2007; Sen & Thorpe, 1977)*, the Si-O-Si bond angle for the various oxides in films annealed at different temperatures can be derived from the equation

$$V_s^2=\left(\frac{1}{2000\pi c}\right)^2\left[\left(\frac{\alpha}{m}\right)(1-cos\,\theta)+\left(\frac{4\alpha}{3M}\right)\right] \tag{1}$$

where c is the speed of light (m/s), m and M are the mass (in kg) of the O and Si atoms, respectively, α is the force constant (in N/m) of the Si-O bonds, θ is the Si-O-Si bond angle and V_s is the stretching frequency. The Si-O-Si bond angles for the various oxides in films annealed at 400 ℃, 600 ℃, 800 ℃ and 1000 ℃ are 136 °, 139 °, 145 ° and 148 °, respectively. It should be noted that the bond angle increases with annealing temperature. It is apparent that atoms gain more energy from higher temperature, resulting in more vigorous AS motion in which O atoms move back and forth along a line parallel to the axis through the two Si atoms.

(c) X-ray Diffractometry (XRD)

The XRD spectra of the Au/SiO_x films annealed at different temperatures is demonstrated in Figure 4.8. A relatively sharp diffraction peak appears at around 38.2 ° which corresponds to crystalline Au plane with orientation of (111). The size of Au crystallites was estimated from Scherrer's equation *(Devadason & Muhamad, 2007)*,

$D = (0.9\,\lambda)/\,(B\cos\theta)$

where λ is the X-ray wavelength, θ is the Bragg diffraction angle and B is the full-width at half-maximum (FWHM).

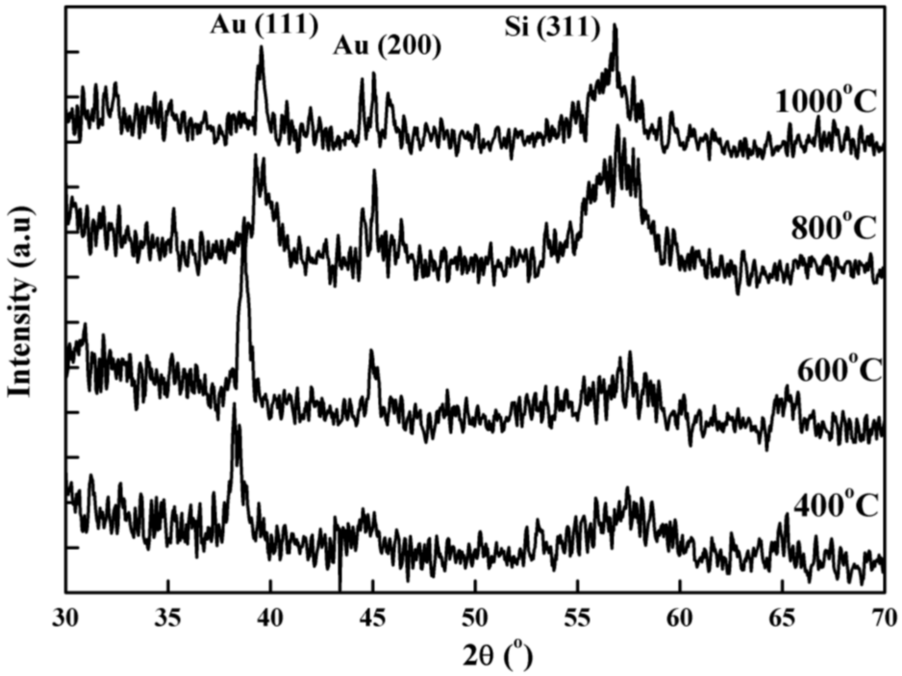

Figure 4.8: XRD spectra of samples annealed at different temperatures.

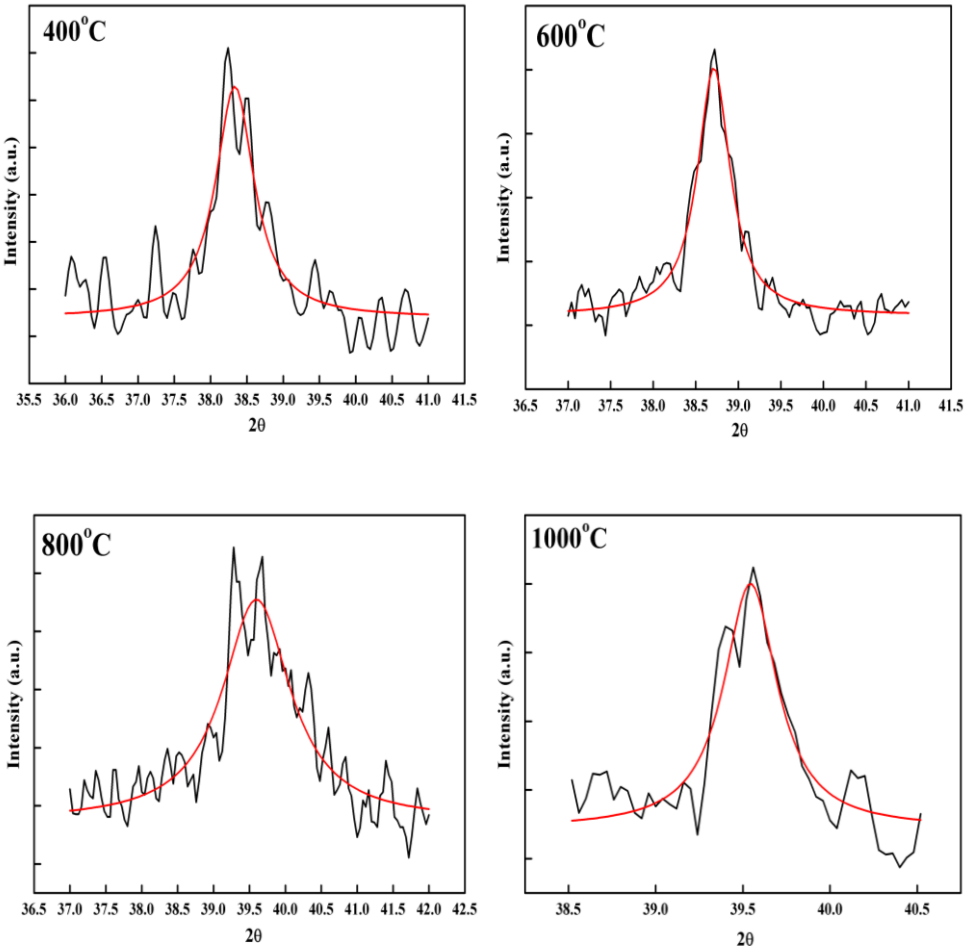

Figure 4.9: Curve fitting on diffraction peak of Au (111) annealed at different temperatures

Peak shifts for Au diffraction peak (111) can be observed as annealing temperature increases. This might result from the effect of stacking faults in the crystalline structure. However, FWHM of the Au diffraction peak can be obtained by fitting the curve, as shown in Figure 4.9. The size of Au crystallites is found in the range of 7 to 23 nm. Crystalline structure of SiO_x is absent since there is no any diffraction peak of SiO_x being observed in the spectra. Nevertheless, a broad peak at around 56 ° which corresponds to the crystalline Si plane with orientation of (311) can be observed. It seems highly probable that this silicon diffraction peak might come from the c-Si substrate. On the whole, this silicon peak becomes narrower as the annealing temperature is increased from 400 ℃ up to 1000 ^{o}C indicating the samples become more crystalline.

(d) Ultraviolet-Visible-Near Infrared (UV-VIS-NIR)

The optical properties of the samples annealed at different annealing temperatures were investigated by optical transmission and reflection spectroscopy for the samples deposited on the quartz substrate. The transmittance, T, and reflectance, R, spectra of the samples annealed at different temperatures are shown in Figure 4.10. It is observed that the samples are very transparent in the near-infrared region. This transparency increases with annealing temperature until 800 ^{o}C. It appears that a very low reflection spectrum, besides the sharp reduction of transmission in the absorption region, was observed at the higher annealing temperature of 1000 ^{o}C. To study the effect of surface plasmon resonance (SPR) attributed by Au particles with varying annealing temperatures, the absorption coefficient of the annealed samples has been plotted against wavelength, as shown in Figure 4.11. The absorption coefficient, α, can be calculated from both transmittance and reflection spectra using the following expression *(Al-Kuhaili, 2008)* $T = (1-R)e^{-\alpha d}$ where $\alpha = \frac{1}{d} ln\left(\frac{1-R}{T}\right)$ and d is the sample thickness, which was determined by the surface profiler. In this case, it should be noted that in order to determine the thickness d of sample annealed at 1000 ^{o}C, the growth of NWs must be assumed to be uniform all over the surface.

In the figure, a very broad SPR peak starts to exhibit at around 735 nm due to the formation of elongated and island-like Au particles on the samples annealed at 400 ℃. As the shape of the Au particles became irregular at 600 ℃, the SPR peak tends to blue-shift to 580 nm and increase in intensity. With further increase in annealing temperature up to 800 ℃, the formation of less concentrated but larger island-like Au particles results in the red-shift of the SPR peak to 635 nm and an increase in its intensity.

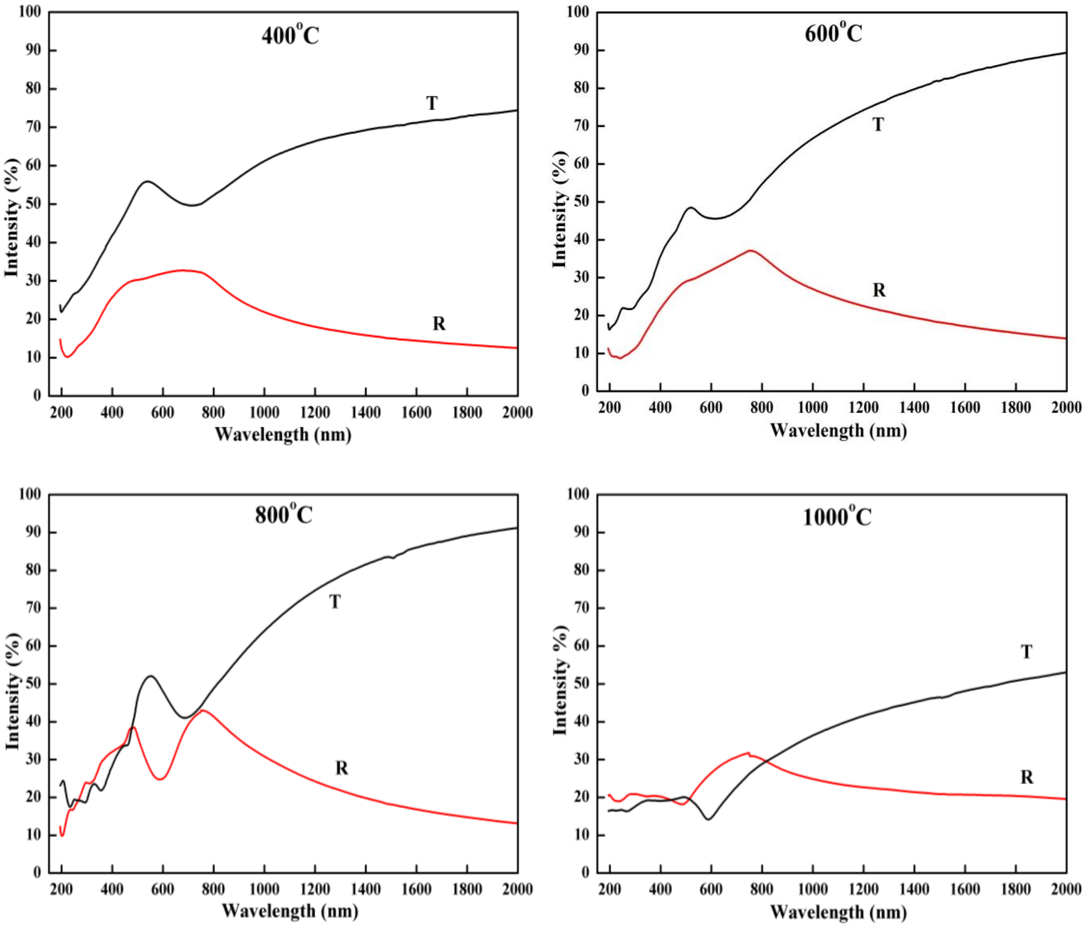

Figure 4.10: Optical transmittance and reflectance spectra of samples annealed at different temperatures.

These results differ from the results reported by other researchers for Au particles prepared by the RF sputtering method, where the SPR peak appears at around 530 nm *(Jung et al., 2008; Sangpour et al., 2007)*. Furthermore, the results shown here demonstrate that the intensity, position and width of the SPR peaks are strongly dependent on the size and shape of the Au particles. Since the growth mechanism of NWs observed on c-Si substrate follows the SLS mechanism, it is expected that there no NWs found on the quartz substrate. This can be proved by the FESEM image shown in the inset in Figure 4.11. In addition, the SPR peak becomes sharper due to the agglomerated Au particles. The increase in inter-particle distance results in the decrease of dipolar interaction. This in turn leads to the blue shift of the SPR peak.

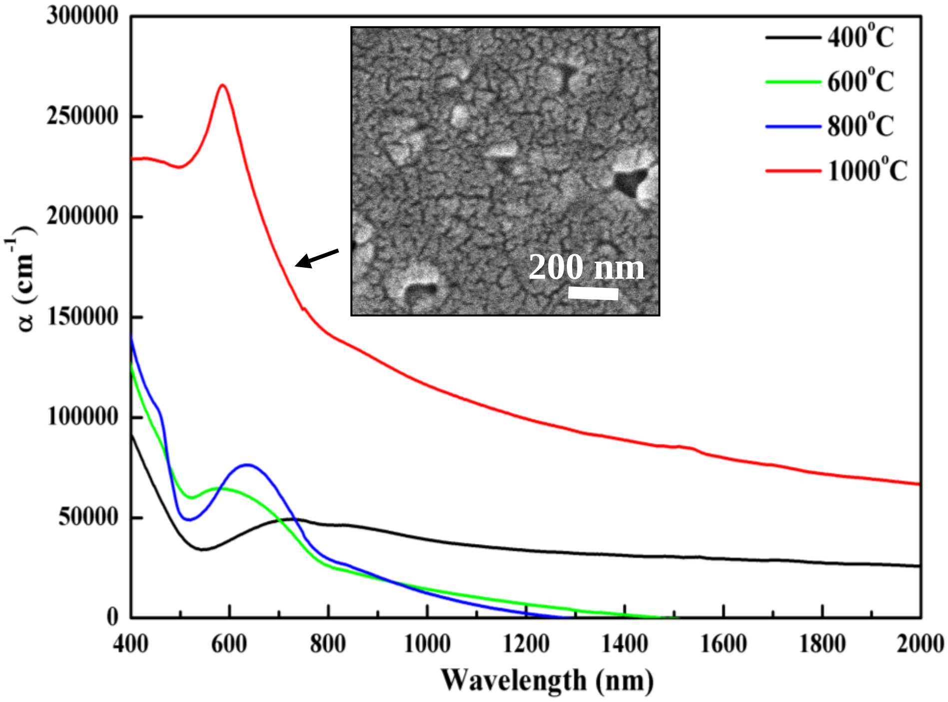

Figure 4.11: Absorption coefficient spectra of samples annealed at different temperatures. Inset shows the FESEM image of Au/SiO$_x$ coated on quartz substrate and annealed at 1000 ^{o}C.

4.2.3 Embedded IN Structures

(a) Field Emission Scanning Emission Microscopy (FESEM)

FESEM images of the SiO_x films embedded with Au NPs are presented in Figure 4.12. Figure 4.12(a) shows the homogenous film observed at an annealing temperature of 400 ℃ without any particles having been found on the surface of the film. At such a relatively lower temperature, the embedded Au atoms sputtered from the Au target have less diffusion ability toward the silicon substrate or the surface of the film, as these Au atoms gain less kinetic energy and, thus, demonstrate a slow mobility *(Sangpour et al. 2007)*. With the increasing of temperature, the Au atoms gain higher kinetic energy and mobility to aggregate with each other to form Au NPs. Those NPs tend to diffuse toward the surface of the film and disperse on it non-uniformly, as shown in Figure 4.12(b). Moreover, these Au NPs also have the ability to diffuse toward the silicon substrate, resulting in the formation of gold silicides (Au_xSi_y) *(Adachi, 2002)*. That could happen, as the eutectic point of Au with silicon is as low as 363 ℃, and the thickness of film is about 60 nm. However, the continuous diffusion of Au NPs into the silicon substrate can be prevented, to some extent, by the SiO_x films that act as an effective barrier layer due to the low diffusion coefficient of Au in SiO_2 *(F. Ruffino, 2008)* This is attributed to the fact that the formation energy of particles decreases as the surface tension decreases. The surface tension of Si (0.78 J/m^2) is known to be lower than that of SiO_2 (1.5 J/m^2), indicating that higher formation energy of particles is required on the SiO_2 than the c-Si substrate *(Bruno et al., 2010b)*. At an annealing temperature of 800 ℃, spherical-shaped Au NPs with an average diameter of about 38 nm are observed to distribute uniformly on the surface of the SiO_x film, as displayed in Figures 4.12(c). Up to now, it is apparent that the diffusion of Au NPs toward the surface of films is temperature dependent *(Grimaldi, 2010; Miotello et al., 2001a)*. Results here show a different morphological phenomenon as compared with the previous work that the “supported ON” structure of Au/SiO_x films was adopted. Therefore, it is recognized that the surrounding medium of Au NPs has a great impact on the growth and distribution of Au NPs in and on the SiO_x films *(F Ruffino et al., 2007)*. Further, it is worthwhile to highlight that the formation of uniformly distributed and spherical-shaped Au NPs on the surface of SiO_x films could only be observed at a temperature as high as 800 ℃ because of the characteristic of gold having low diffusivity *(Grimaldi, 2010)*.

At a higher temperature of 1000 ℃, it is interesting to observe the growth of non-aligned but closely-packed nanowires, with average lengths and diameters of 2 μm and 125 nm, respectively, as shown in Figure 4.12(d). Despite there being a lot of papers dealing with the formation of silica nanowires by high temperature annealing of thin metal film *(Elechiguerra et al., 2004; Sekhar et al., 2006)*, the formation mechanism of nanowires in this work follows the solid-liquid-solid (SLS) mechanism, which requires a silicon source from the substrate *(Cabarrocas, 2009; Kolasinski, 2006)*. This can be confirmed by the non-existence of nanowires on the quartz substrate annealed at the same temperature of 1000 ℃ in the next section. It is reasonable to indicate that more silicon atoms from the substrate have diffused into Au-Si alloy droplets, as the temperature was increased beyond 800 ℃, leading to the super saturation of silicon in droplets at an annealing temperature of 1000 ℃. These silicon atoms are then precipitated into the Au-Si alloy droplets to grow into the nanowires. The EDX elemental analysis shows that the composition of these nanowires consists of 56 atomic % and 44 atomic % of silicon and oxygen, respectively, with Au catalysts (0.7 atomic %) present on the tips of the nanowires. This indicates that the nanowires grown are Au-assisted catalytic growth of silica nanowires (SiO_x NWs).

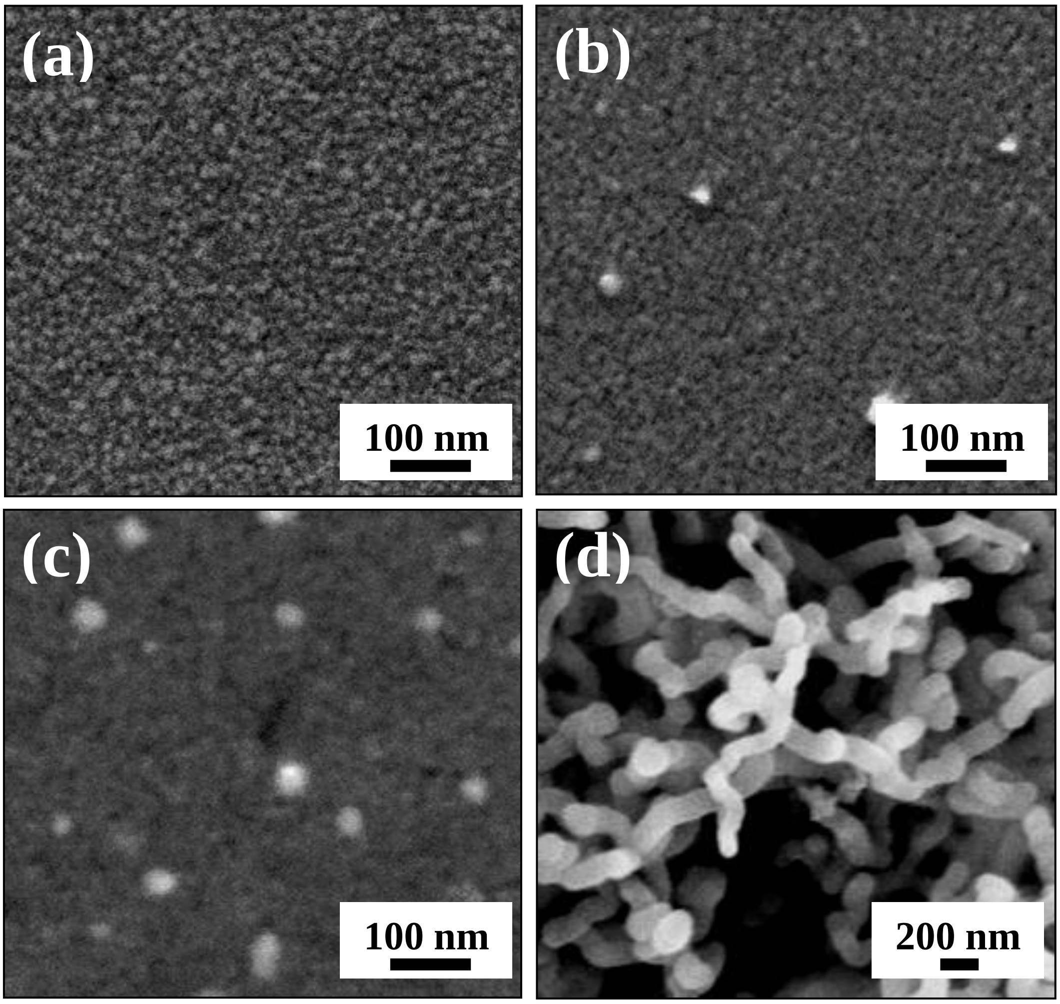

Figure 4.12: FESEM images of Au/SiO$_x$ films annealed at different annealing temperatures of (a) 400 ℃, (b) 600 ℃, (c) 800 ℃, (d) 1000 ℃

For the microstructure investigation, a TEM study of a single nanowire has been carried out. Figure 4.13(a) clearly shows a single nanowire with an Au catalyst at the tip. The SiO$_x$ NWs are amorphous in structure, as confirmed by the HRTEM image taken from the surface of a single nanowire [Figure 4.13(b)]. NWs show no clear lattice plane of silicon besides not being covered with the different size and shape of nanostructures. Moreover, it has been known from previous reports that Au catalysts supported ON or embedded IN SiO$_x$ film can induce the growth of nanowires with a slightly different structure.

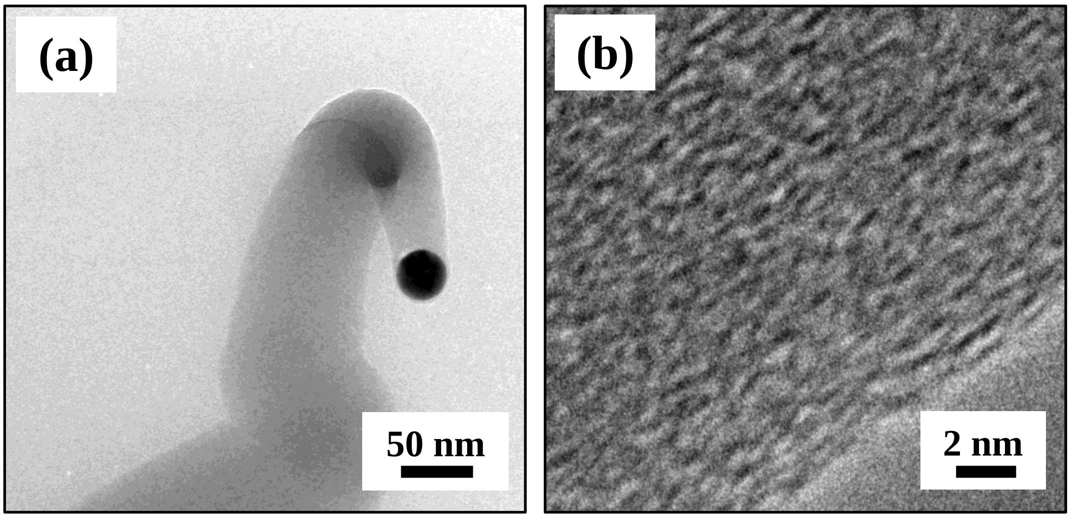

Figure 4.13: Plane-view of (a) TEM and (b) HRTEM images showing the nanostructures of samples annealed at 1000 ℃.

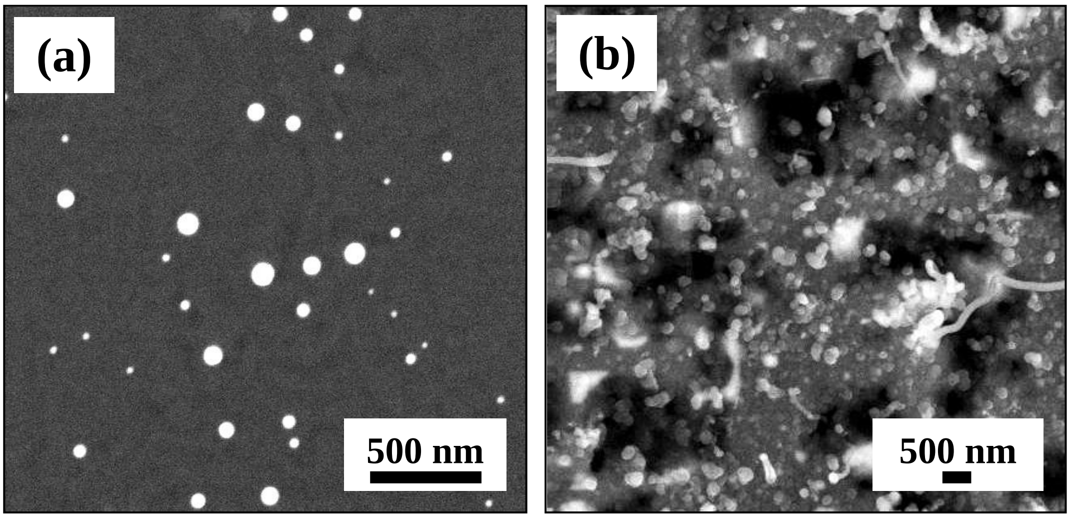

Figure 4.14: SEM images of the samples annealed at different temperatures: (a) 900 ℃, (b) 1100 ℃

In order to investigate the formation of SiO_x nanowires occurred at a critical annealing temperature of 1000 ℃, as-prepared Au/SiO_x films were annealed at temperatures of 900 ℃ and 1100 ℃ in the same condition with other parameters remaining unchanged. These results are shown in Figure 4.14. It is found that the size of the Au NPs becomes even bigger at 900 ℃. The diameter is approximated to be 52 nm, without any formation of nanowires. However, it is observed that the growth of the nanowires has been degraded at higher temperature of 1100 ℃. These nanowires are not closed-packed as compared to that of the nanowires grown at 1000 ℃. Thus, it is logical to predict that 1000 ℃ is the critical temperatures for the growth of SiO_x nanowires in this work.

(b) Fourier Transform Infrared (FTIR)

Figure 4.15 shows the FTIR spectra of the Au/SiO_x films annealed at different temperatures. A typical FTIR spectrum of SiO_x films usually consists of three absorption bands with the position located at around 460 cm^{-1}, 816 cm^{-1}, and 1080 cm^{-1}, which correspond to the rocking, bending, and stretching vibrational modes of the Si-O-Si band, respectively. These three absorption bands can be characterized in terms of the particular vibrational mode of oxygen (O) atoms with regard to the silicon (Si) atom pairs that they bond to, as indicated by Kirk *(1988)*. From the IR spectra shown in the figure, appearance of the absorption band at 920 cm^{-1} can be observed as the films are initially annealed at 400 ^{o}C. This peak is contributed by the well-recognized IR band of porous silicon *(Parkhutik et al,. 2000*). However, the porosity of the film is eliminated as higher energy is supplied from the subsequent annealing process. An absorption band of Si-O-Si bending mode positioned at 816 cm^{-1} does not appear below the temperature of 1000 ^{o}C, indicating a low level of oxidation in the Au/SiO_x films.

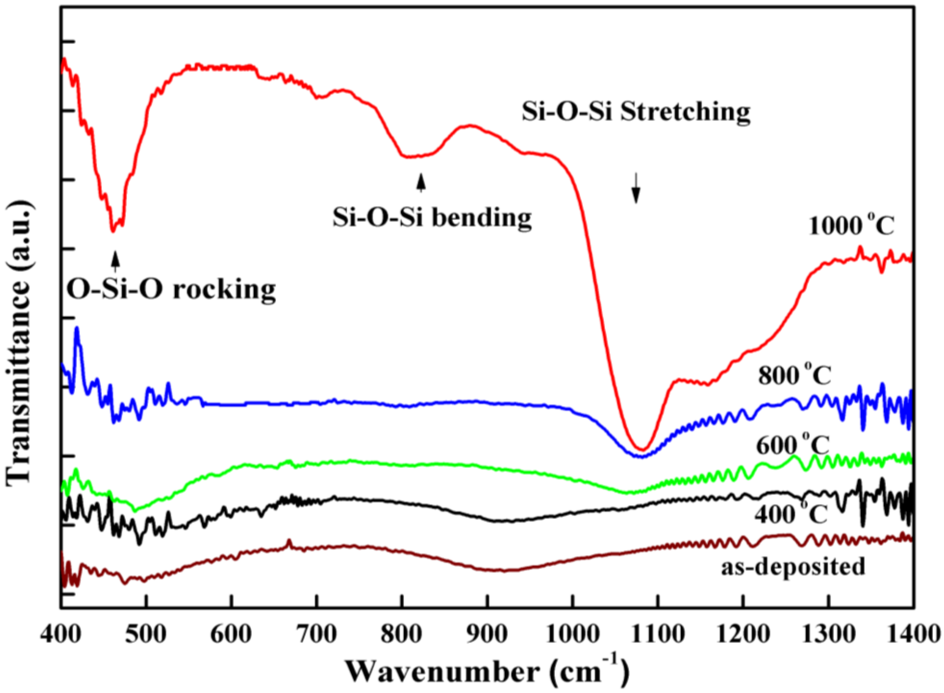

Figure 4.15: Transmission FTIR spectra of the samples annealed at different annealing temperatures.

Compared with the SiO_x films with Au supported ON the surface, the oxide characteristic of SiO_x films embedded with Au encounter much more suppression, leading to the lower concentration of SiO_x in the samples. It has been generally accepted that an interaction between Au and oxygen is not energetically favourable due to the inertness of Au *(Jiang et al., 2010*). Thus, we can expect that Au particles tend to react with silicon atoms near the interface between the silicon substrate and SiO_x films to form Au_xSi_y during the diffusion of Au toward the surface of the film. As the diffusion of Au gets closer to the surface of the film resulting from the higher annealing temperature, a less amount of Au_xSi_y will be formed due to the barrier effect exhibited by the SiO_x films. This barrier effect is greatly enhanced as the gap of the SiO_x film between Au and the silicon substrate becomes larger *(Rath et al., 2011)*. This leads to a relatively easy combination of oxygen and silicon atoms to form silicon oxide. Therefore, it is not surprising to observe the abrupt increase in the intensity of the rocking and bending absorption peaks of the samples at an annealing temperature of 1000 ^{o}C. This phenomenon can also be attributed to the formation of nanowires, which have a large surface area, enhancing the incorporation of oxygen content to the nanowires during the annealing process. In addition, we found that the stretching absorption peak also shifts from a lower frequency to a higher frequency, besides becoming narrower and increasing in intensity as the annealing temperature increases from 400 °C to 1000 °C. These phenomena are due to the fact that a greater amount of oxygen from SiO_x or air has been relatively easy to bond to silicon atoms forming silicon oxide at higher annealing temperatures.

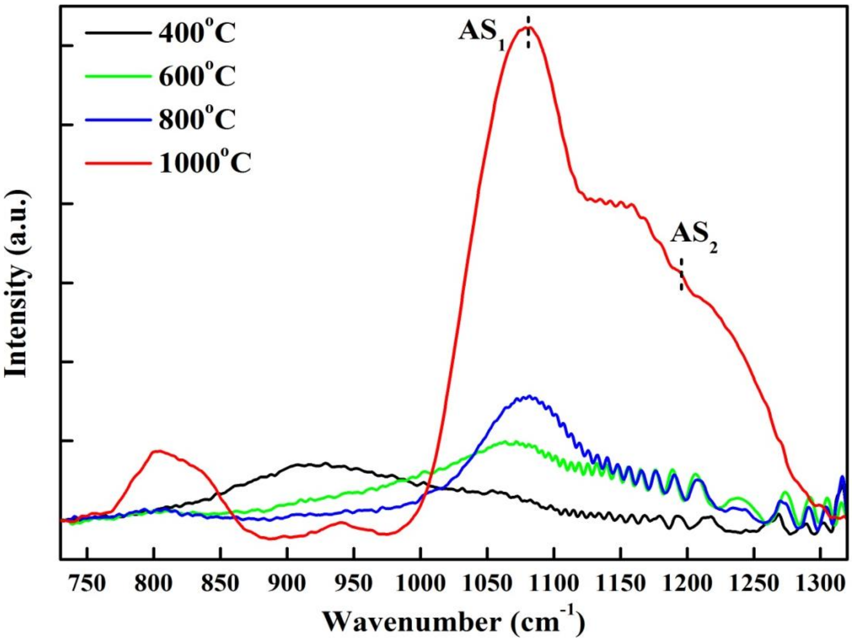

Figure 4.16: The absorption coefficient FTIR spectra of the samples annealed at different annealing temperatures.

Figure 4.16 shows the IR absorbance spectra of the Si-O-Si stretching vibrational mode of the samples annealed at different temperatures. In general, the asymmetrical stretching (AS) motion, which occurs in a high frequency region, can give rise to two vibrational modes *(Kirk, 1988; Niu et al., 2007)*. The main peak located at 1080 cm^{-1} is regarded as a contribution of the AS_1 modes, in which the adjacent O atoms execute the AS motion in phase with each other.

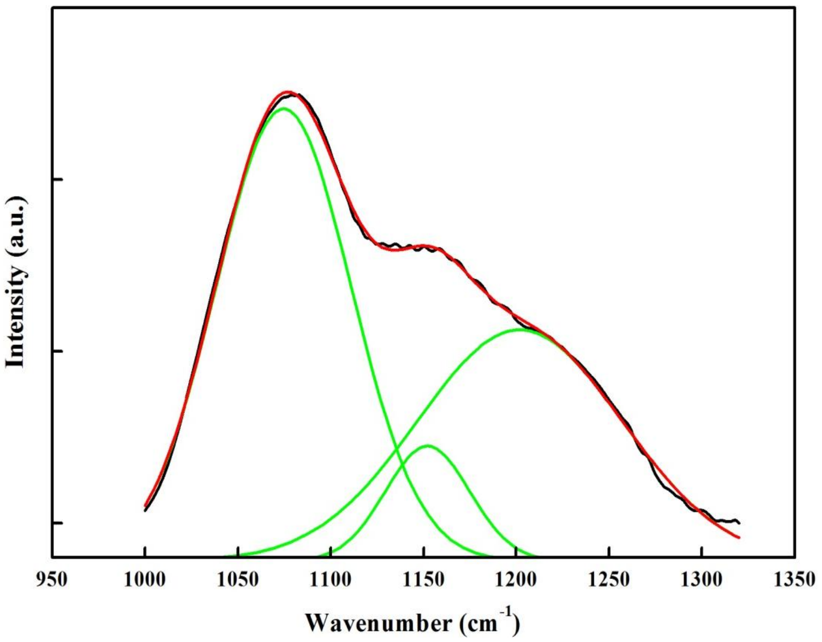

Figure 4.17: Curve fitting on the Si-O-Si stretching peak with absorption mode at annealing temperatures of 1000 ℃.

Figure 4.17 shows that there is a broad shoulder in the absorption peak centred at 1200 cm^{-1} for the sample annealed at 1000 ℃. This can be attributed to the AS_2 mode, in which adjacent O atoms execute the AS motion 180° out of phase with each other. The AS_1 and AS_2 absorption peaks of 1080 and 1200 cm^{-1}, respectively, are consistent with the results shown by Kirk, who investigated the oxide layer on a silicon wafer *(Kirk, 1988)*. Thus, this supports the EDX results by indicating that nanowires grown at 1000 ℃ contain an oxide layer on the surface, thereby forming SiO_x nanowires.

(c) X-ray Diffractometry (XRD)

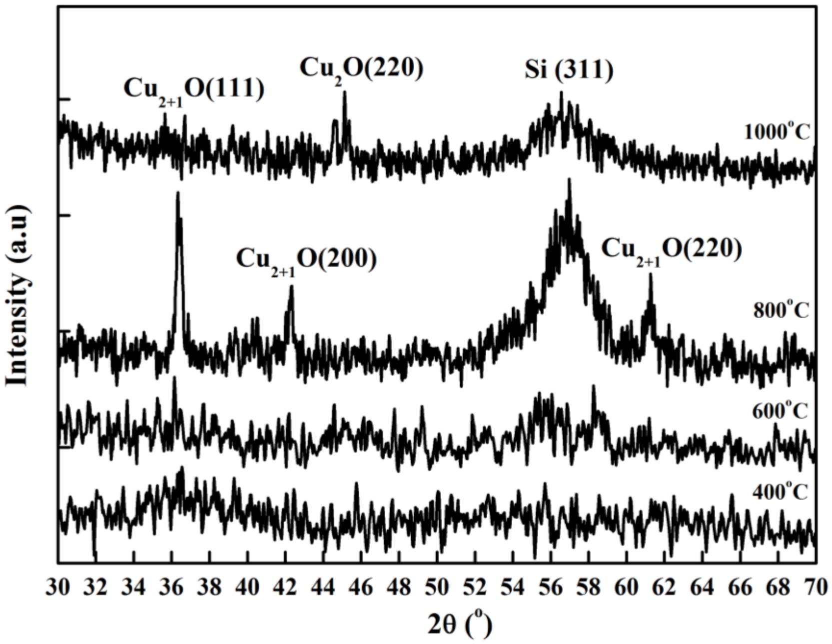

Figure 4.18: XRD spectra of Au/SiO_x films annealed at different temperatures.

Figure 4.18 presents the XRD spectra of the samples annealed at different temperatures. Surprisingly, there are no diffraction peaks of Au crystallites being observed. In the opposite, without using any copper sources, Cu-based crystallites did exist. $Cu_{2+1}O$ and Cu_2O diffraction peaks are observed on film annealed above 800 ^oC. It shows that a critical contamination occurs during the deposition process. It might be one of the factors resulting in the low deposition rate of this experiment. In addition, the absence of Au diffraction peak can be due to two reasons. Firstly, Cu is deduced to be easier in forming crystallite structure as compared to Au. Secondly, volume fraction of Au is very low in this work since the Au wires used for co-sputtering process are only 4 pieces (each of which was 2.5 mm in length and 1 mm in diameter). On the other hand, it is highly suspected that these copper sources come from the components inside the sputtering system. At lower temperatures, Cu atoms sputtered out from the copper components with less kinetic energy to form the Cu crystallites, leading to the non-existence of diffraction peaks on the samples until temperature is set above 600 ^oC.

As the temperature is increased to 800 °C, $Cu_{2+1}O$ (111), (200) and (200) diffraction peaks are found to appear at the 2θ of 36.4°, 42.3° and 61.3°, respectively. Besides that, diffraction peaks positioned at 56°, which correspond to crystalline Si with an orientation of (311) plane can also be observed. This can be attributed to the c-Si substrate effect. From Scherrer's equation *(Devadason & Muhamad, 2007)*, the estimated size of the Si nanocrystallites is about 4 nm. As the temperature is further increased to 1000 °C, the three diffraction peaks of $Cu_{2+1}O$ disappear. With the increase in annealing temperature, Cu contaminants transformed their cubic lattice structure to another structure, resulting in the appearance of Cu_2O diffraction peak, with the orientation plane of (200), at the 2θ of 44.7°.

(d) Ultraviolet-Visible-Near Infrared (UV-VIS-NIR)

The optical properties of the annealed samples deposited on quartz substrates were investigated using optical transmission and reflection spectroscopy due to the fact that quartz substrate is known to be completely transparent throughout the UV-VIS-NIR wavelength region. Figure 4.19 presents the transmittance and reflectance spectra of the annealed Au/SiO_x films prepared on the quartz substrate. It is observed that all the samples are very transparent in the near-infrared region. However, their transparency decreases towards the shorter wavelength region. Moreover, a very low reflection spectrum has been observed for the Au/SiO_x film annealed at higher temperature of 1000 °C. This is resulted from the growth of densely-packed SiO_x nanostructures distributed with some agglomerated Au NPs.

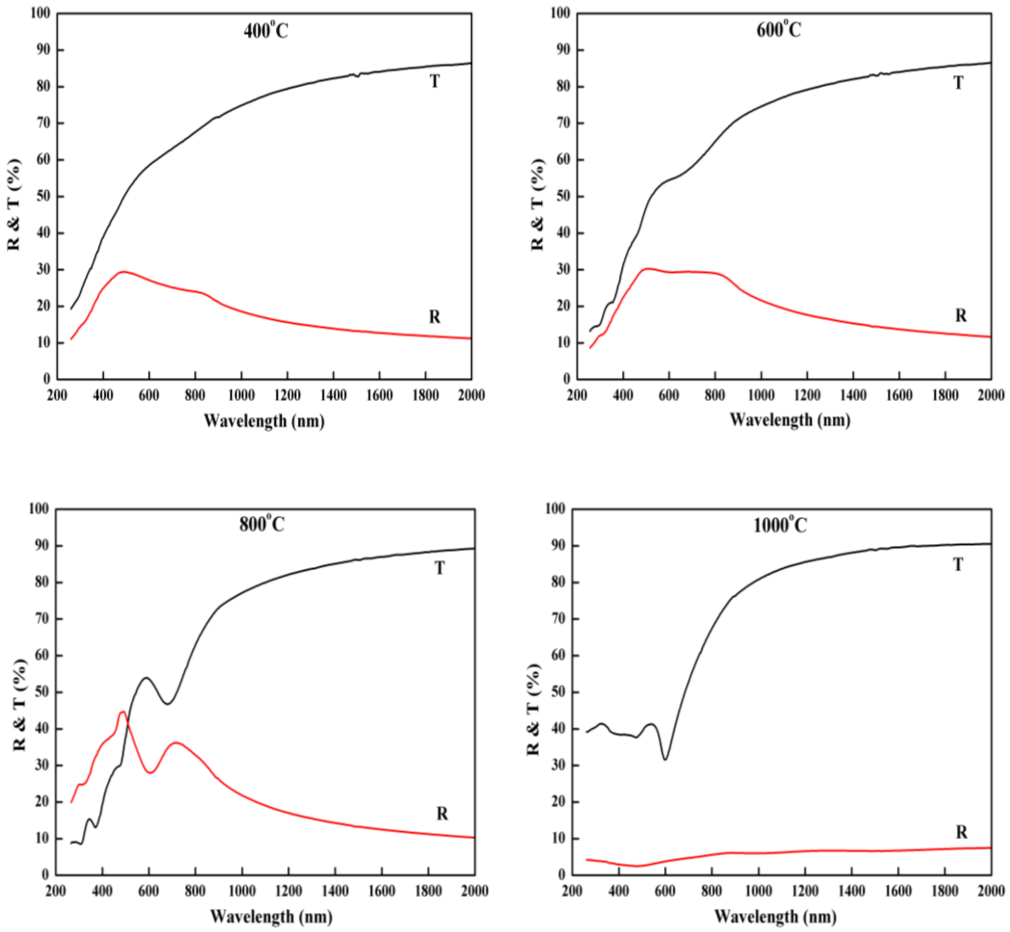

Figure 4.19: Optical transmittance and reflectance spectra of Au NPs in SiO$_x$ films annealed at different temperatures.

This can be clearly shown in the FESEM images of Au/SiO$_x$ films deposited on quartz substrate and annealed at 800 ^{o}C and 1000 ^{o}C (Figure 4.20). As compared to Figure 4.12(d), Figure 4.20 shows that the formation of NWs cannot be observed at 1000 ^{o}C due to the absence of silicon source from the quartz substrate following the SLS growth mechanism. On the other hand, bigger sizes of agglomerated Au NPs are observed. As for the sample annealed at 800 ^{o}C, the morphology of the film is similar to that of the film deposited on c-Si substrate [Figure 4.12(c)].

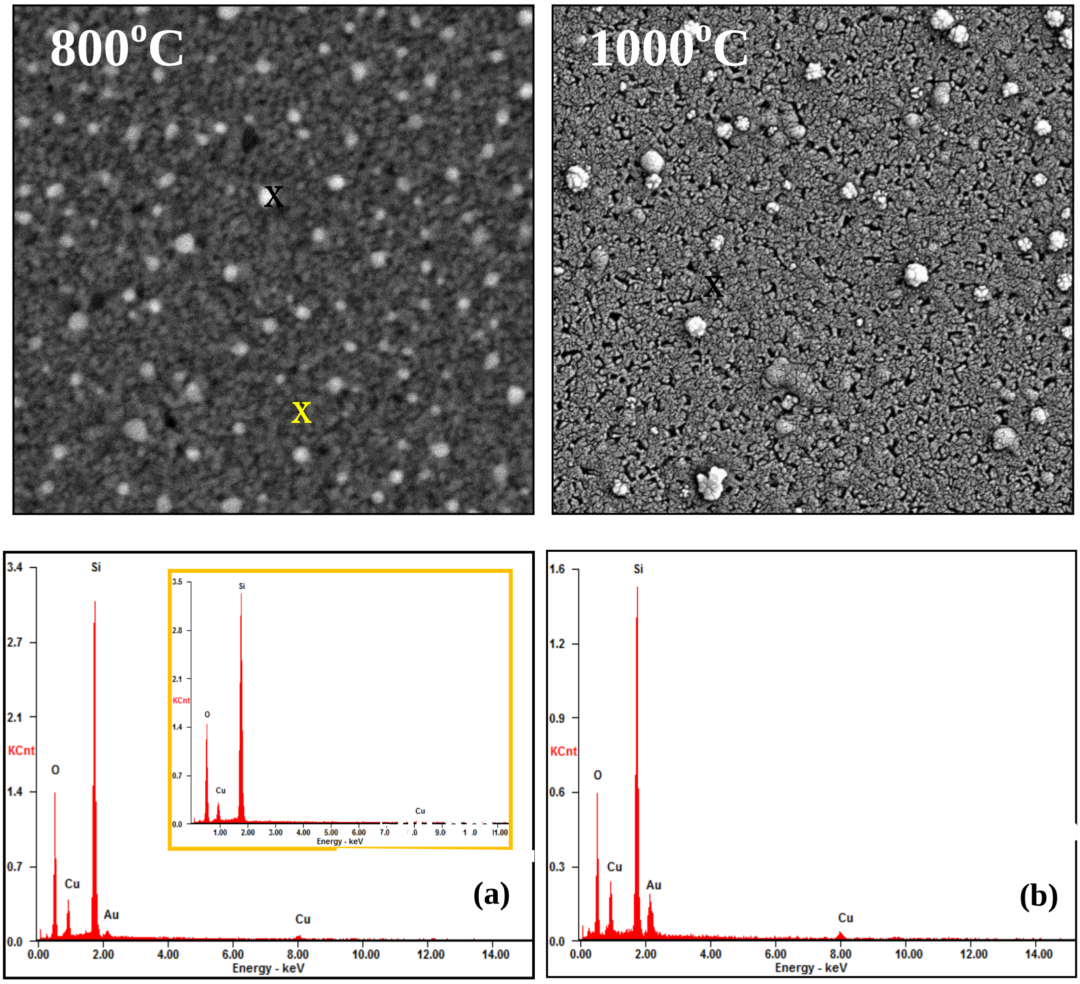

Figure 4.20: FESEM image of the Au/SiO$_x$ film deposited on quartz substrate and annealed at 800 ^{o}C and 1000 ^{o}C. Figure (a) and (b) shows the corresponding EDX analysis on the film annealed at 800 ^{o}C and 1000 ^{o}C, respectively.

EDX analysis has confirmed that the white dots consist of Au NPs after comparing the composition of the white dots and grey area (SiO$_x$ film). On the other hand, through EDX analysis, contamination resulting from copper (Cu) is shown to incorporate into the Au/SiO$_x$ film which correlates well with the results shown in XRD spectra. It is believed that these Cu sources come from the sputtering components inside the RF magnetron sputtering system.

For the investigation of surface plasmon resonance (SPR) induced by Au NPs, absorption coefficient, α of the samples annealed at different temperatures is calculated from both the transmittance and the reflection spectra using the following expression *(Al-Kuhaili, 2008)*, $T = (1 - R)e^{-\alpha d}$ (2)

$$\alpha = \frac{1}{d} ln\left(\frac{1-R}{T}\right) \tag{3}$$

where d is the sample thickness, as determined by the surface profiler. The thickness is uniform throughout the area from the measurement. Figure 4.21 shows the absorption coefficient, α, plotted against the wavelength of incident lights.

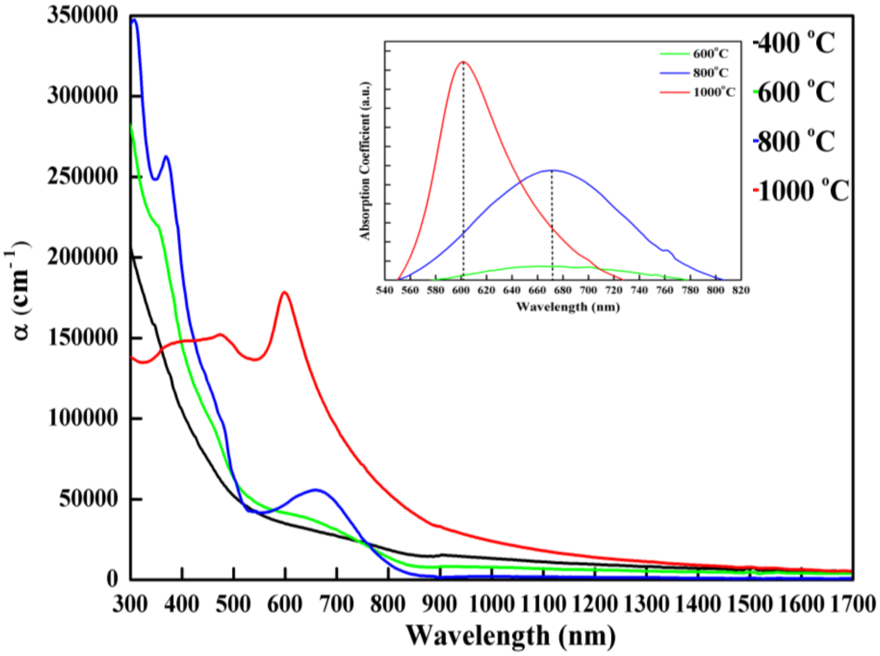

Figure 4.21: The optical absorption coefficient spectra of the Au NPs in SiO$_x$ films annealed at different annealing temperatures. The inset shows the fitted SPR absorption peak except 400 ^{o}C that does not show significant absorption peak.

For the sample annealed at 800 ^{o}C, a prominent peak at 380 nm appears in the UV region, indicating the 5*d* to 6*sp* inter-band transition of Au NPs. This is the result of the transitions of an electron from the occupied *d*-level state to an empty state in the conduction band above the Fermi level in a noble metal like Au *(Balamurugan & Maruyama,2005; Haridas et al,. 2008; Xie et al., 2010)*. It is found that significant SPR peak only starts to exhibit as Au/SiO$_x$ films are annealed above 400 ℃. Since it has been reported that NPs with a size of less than 2 nm does not exhibit an SPR peak *(Jung et al., 2008; Sangpour et al., 2007; Yu et al., 2005)*, the size of embedded Au NPs in SiO$_x$ film annealed at 400 ^oC is expected to be very small. This can be supported by the FESEM image discussed above, as shown in Figure 4.12 (a). Furthermore, low intensity of SPR peak positioned at 672 nm can be clearly observed at 600 ^oC. With an increase in annealing temperature to 800 ^oC, the peak position remains unchanged but the intensity of the SPR peak increases. SPR peak blue-shifts to around 600 nm, with further increase and narrowing in intensity and width of the peak, respectively, as the annealing temperature reaches 1000 ℃.

Since the intensity and position of SPR peak depend greatly on the size and shape of Au NPs, an increase in the intensity of the SPR peak is related to the increase of the size of Au NPs. On the other hand, larger size Au NPs is found to red-shift the SPR peak, as shown by the samples annealed from 400 to 800 ℃. However, besides the enlargement in size, Figure 4.20 shows that the inter-particle distance of the Au NPs in film annealed at 1000 ℃ also increases sharply due to the agglomeration of smaller particles into the bigger one. It has been known that increase in dipolar interaction or decrease in inter-particle distance between adjacent particles can widen and red-shift the SPR peak *(Serrano et al., 2010)*. Thus, the observed increase in intensity and blue-shift of SPR peak at 1000 ^oC can be related to the increase in size of agglomerated Au NPs and inter-particle distance of Au NPs, respectively.

4.3 Chemical Vapor Deposition (CVD) Method

4.3.1 Introduction

Since PVD techniques have been extensively studied for past decades, CVD techniques now become our interest to prepare Au/SiO$_x$ film due to its advantage of being simpler and feasible method. Additionally, the CVD system used for sample preparation is a homebuilt system that are flexibly in modification on the system in order to achieve higher efficiency for controlling the size of Au NPs. As compared to the "embedded IN" structure of Au/SiO$_x$ films, the "supported ON" structure of Au/SiO$_x$ films is observed to show more interesting results, as depicted in the previous sub-chapter. Therefore, Au ON SiO$_x$ films become the main focus for the rest of this work.

Hereby, the preparations of Au particles are carried out by using two different methods. Firstly, a thin layer of Au film was sputtered onto the surface of SiO$_x$ films, prepared by plasma-enhanced chemical vapor deposition (PECVD) technique, using DC sputter coater. SiO$_x$ films were deposited using different flow rate ratio of N_2O/SiH_4 varied from 5 to 40, resulting in the different composition percentage of silicon and oxygen in SiO$_x$ films. The flow rate of N_2O gas was varied from 10 to 80 sccm, while SiH_4 gas was fixed at 2 sccm. The rf power, substrate temperature, deposition pressure and deposition time were fixed at 100 W, 300 ^{o}C and 1.0 mbar and 1 hour, respectively, throughout the entire deposition process. The helium (He) gases were introduced into the system chamber to maintain the deposition pressure at 1.0 mbar without changing the pumping speed of rotary pump. The as-prepared Au/SiO$_x$ films were then post-thermal annealed for 1 hour at constant temperature of 800 ^{o}C using a conventional furnace. The effect of surrounding medium (SiO$_x$ film) on the growth of Au particles at constant annealing temperature was studied and presented in section 4.3.2. To conclude this sub-chapter, it was expected to obtain the optimal flow rate ratio of N_2O/SiH_4 for the preparation of SiO_x film which can be the most suitable surrounding medium for the growth of Au NPs.

Secondly, hot wire (tungsten filament) was used to replace the DC sputter coater to prepare the Au particles supported ON SiO_x film. This aims to promote the one-step preparation process where the evaporation of Au can be carried out just after the deposition of SiO_x film inside the system chamber. This can reduce the unwanted contamination during the removal of samples out of chamber for the subsequent Au sputtering process. However, hot wire evaporation technique can have the disadvantage of introducing the growth of bigger size and non-uniform shape of Au particles if the shutter is not attached below the hot wire to control the evaporation time of Au. After the shutter is assembled to the system, the problem is significantly resolved. Therefore, smaller size and uniform shape of Au particles can be realized. The results will be presented in chapter 4.3.3. Here, the role of SiO_x film in the growth of Au NPs prepared by hot wire evaporation technique will be studied first. After that, Au will be directly evaporated onto the SiO_x film being heated at certain temperature to investigate the influence of heated SiO_x film on the size of the Au NPs. To start with, a *p-Si (111)* and quartz substrate were put into the vacuum chamber followed by pumping down the chamber to base pressure of around 10^{-5} mbar. Prior to the deposition of SiO_x film, substrates were heated up to 300 ^{o}C. After deposition of SiO_x films for 1 hour, gases (SiH_4, N_2O) cleaning process is carried out. In previous work, we took the SiO_x film out in this stage for Au preparation using DC sputter coater. However, in this work, Au is evaporated using the hot wire just after the SiO_x film deposition inside the chamber by maintaining the substrate temperature at 300 ^{o}C and pressure in high vacuum condition. This will make the SiO_x film into a “heated” SiO_x film. After that, the as-prepared Au/SiO_x films were left heated continuously at 300 ^{o}C for 1 hour in high vacuum condition.

From the previous result shown in Figure 4.2, thermal annealing process that have been carried out at 400 ^oC are shown to be able to induce the growth of Au NPs. Thus, substrate temperature of 300 ^oC that have been adopted in this work is believed to have enough energy to induce the growth of Au NPs also. In addition, to study the annealing effect on the growth of Au NPs coated on the pre-heated SiO_x films, the samples were subsequently thermal annealed at low temperature of 200 ^oC, which is far lower than the annealing temperature used in research work discussed in Chapter 4.2.

4.3.2 DC-Sputtered Au Layer on SiO_x Film

4.3.2.1 Effect of Flow Rate Ratio of Nitrous Oxide/Silane Gases on the Growth of Au NPs

(a) Field Emission Scanning Emission Microscopy (FESEM)

Based on the previous experiment using physical vapor deposition (PVD) method, it was found that 800 ^oC is sufficient to initiate the growth of Au NPs *(Chan et al., 2011)*. Therefore, Figure 4.22 shows the FESEM images of the Au/SiO_x films annealed at constant temperature of 800 ^oC for one hour. As the flow rate ratio of N_2O to SiH_4, η is 5; the sample produces both large and small spherical-like Au particles that distributed evenly on the surface of SiO_x matrix with the average size of 40 to 280 nm. The amount of Au particles decreases but its particle sizes increase (200 to 600 nm) when η is increased to 20. In the FESEM image, one can see that one type of NPs is bright while the other type of NPs appears to be grayish. This is due to the NPs of different heights. Some of the particles have deformed into rod-liked particles due to the coalescence of the small particles into large particles as a result of chemical potential difference of the particles. Gibbs-Thomson effect stated that the potential difference of particles is inversely proportional to the size of particles *(Miotello et al., 2001)*. Besides that, the loss of the Au particles/dielectric matrix interaction also contributes to the loss of particles adhesion to the dielectric matrix and formation of large and isolated Au particles through particles coalescence.

However, very close-packed uniform size of Au NPs are observed as η = 30. These spherical NPs with size ranging from 15 to 70 nm have less agglomeration. With further increase in η up to 40, the film containing both large and small Au particles is observed. This is similar with the sample deposited at η = 5 but higher concentrations of small Au particles are observed with an average size of 40 to 240 nm. From the results, it is observed that agglomeration of Au particles can be effectively inhibited (as shown in Figure 4.22 (a) and (d)) when either the oxygen or silicon content in SiO_x film is dominant in terms of composition of the film. In this case, observation of bigger size of Au particles dispersing on film deposited at η = 20 can be deduced to be attributed to the fact that the oxygen nor silicon content is the dominant composition in films, allowing Au atoms to diffuse into the SiO_x film or aggregate with other Au atoms to form bigger size of Au particles. Nevertheless, it is believed that N_2O/SiH_4 with flow rate ratio of 30 is the optimal ratio to deposit the SiO_x film which can effectively inhibit the aggregation of Au particles and allow the formation of small Au NPs. The detailed analysis of the coalescence process of the Au particles in silicon oxide can be found in reference *(De Marchi et al., 2002; F. Ruffino et al., 2008; F. Ruffino & Grimaldi, 2010)*. However, the mechanism for the formation of small Au NPs on film prepared with η = 30 is not clear yet and certainly worth exploring in future work.

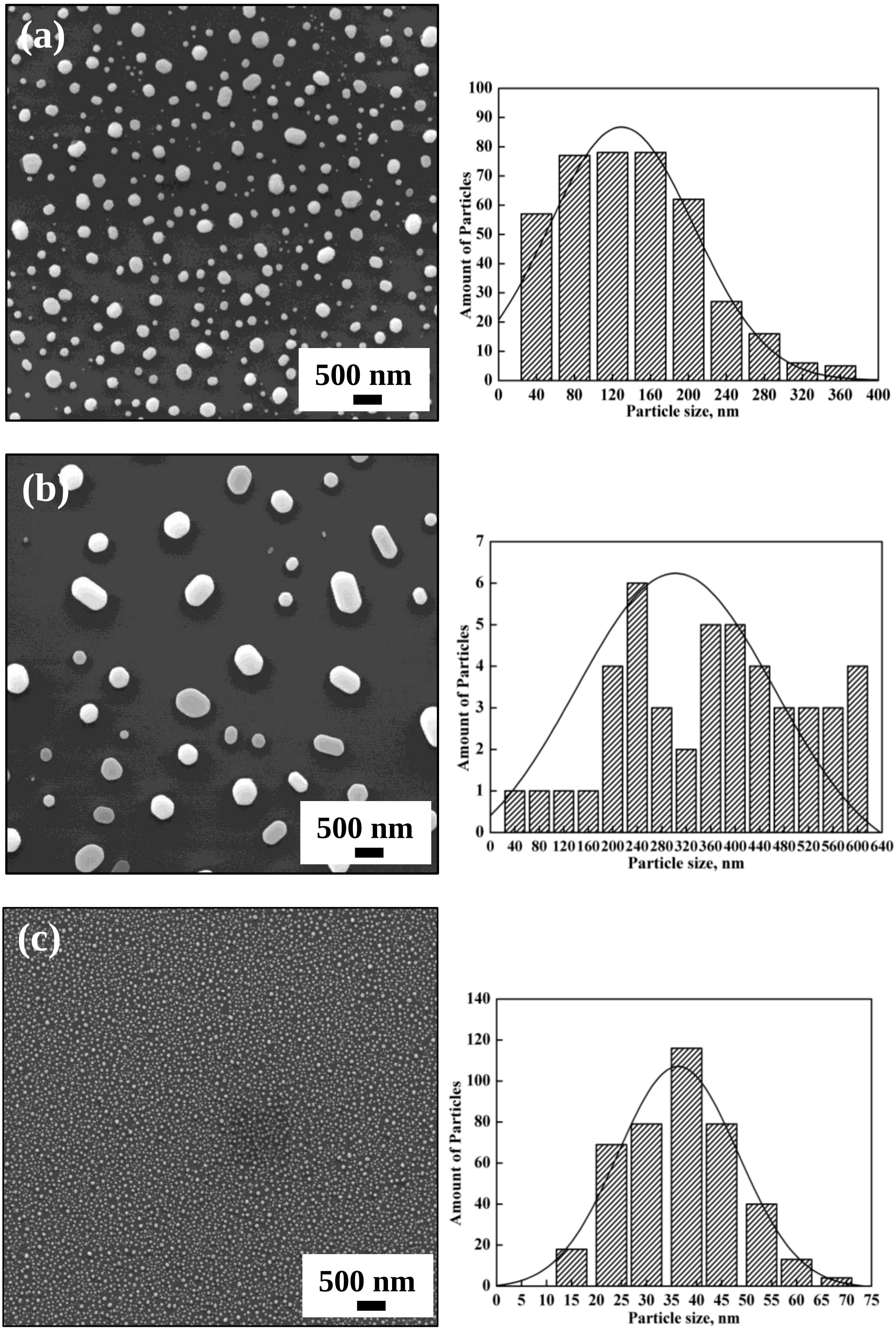

Figure 4.22: FESEM images of Au particles and its size distribution on annealed Au/SiO$_x$ films deposited at different N$_2$O/SiH$_4$ flow rate ratios of (a) 5, (b) 20, (c) 30 and (d) 40.

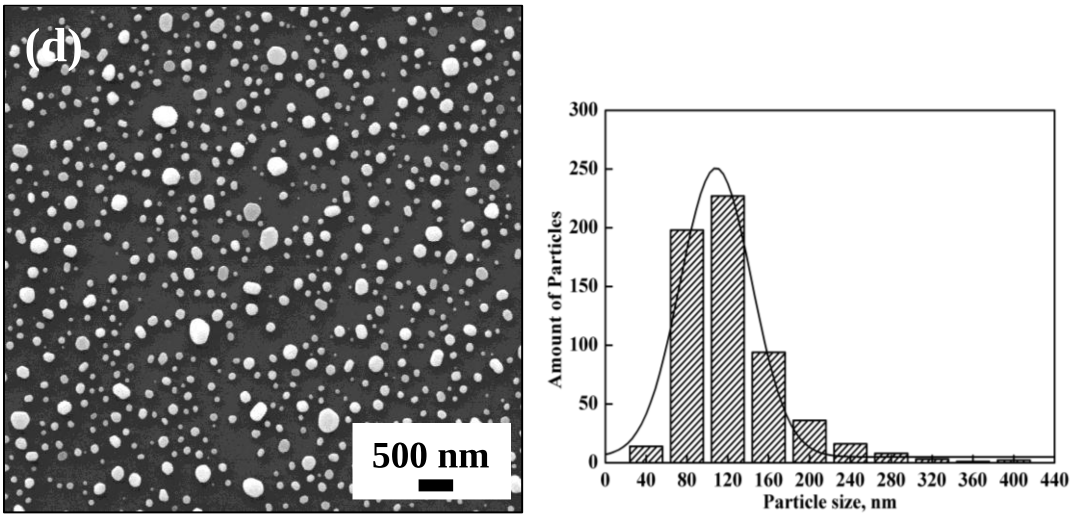

Figure 4.22, continued

(b) Fourier Transform Infrared (FTIR)

Figure 4.23 (a) presents the IR transmittance spectra of the as-deposited SiO_x films deposited at different N_2O/SiH_4 flow rate ratio (η). In this spectrum, three absorption peaks are observed at 460 cm^{-1}, 810 cm^{-1} and 1080 cm^{-1} which correspond to Si-O-Si rocking, bending and stretching vibrational modes respectively *(Kirk, 1988).* The characteristics of these absorption peaks show significant dependence on the η. Generally, SiH_4 molecules have higher dissociation rate as compared to N_2O molecules. However, it is observed that the dissociation rate of N_2O molecules increases as the total gas flow rate decreases at constant RF power. At $\eta = 5$, the intensity of the absorption peaks is significantly higher compared to the other samples due to the dissociation of N_2O molecules being more effective at lower total gas flow rate (10 sccm). Thus, chemical reaction between SiH_m and O radicals is more favourable to the formation of Si-O bonds. This result is different from the works reported by Chen and Morales group *(Chen et al., 2005; Morales-Sánchez et al., 2008).* They presented that SiO_x films deposited at low η produce silicon rich SiO_x film instead of oxygen rich SiO_x film. As the η increases, the samples tend to form stoichiometric SiO_2 film.

In our work, however, the SiO_x films deposited at low η are not dominated by silicon content. Different combination setting of the deposition parameters such as RF power, deposition pressure and substrate temperature lead to different composition of SiO_x film. With increase in η to 20 and 30, the intensity of the absorption peaks decreases due to the fact that the increase of total gas flow rate degrades the dissociation rate of N_2O molecules. Furthermore, the Si-O-Si bending absorption peak diminishes and the intensity of another two absorption peaks decreases with further increase in η to 40. This can be attributed to the higher total gas flow rate of N_2O (80 sccm) resulting in the inefficient N_2O dissociation process, leading to the low concentration of radical reactive species which are dissociated from N_2O gas like O, N and NO radicals. The dissociation mechanism of the SiH_4 and N_2O presented through infrared absorption peaks can be correlated to the growth rate of the films in the variation of η as shown in Figure 4.24. The overall growth rate of films is observed to be quite low in this work.

Figure 4.23(b) shows that the intensity of the absorption peaks decreases when the as-deposited SiO_x films are sputtered with a thin layer of gold onto its surface. Less concentration of SiO_x in the as-deposited Au/SiO_x film can be attributed to the fact that the characteristics of silicon oxide layer on the samples have been suppressed by the Au layer. Furthermore, the intensity and FWHM of the absorption peaks increases and narrow respectively as the Au/SiO_x films are annealed at 800 ^oC, as shown in Figure 4.23(c). This implies that the presence of Au particles has enhanced the structure order of SiO_x films apart from the incorporation of oxygen into the samples during thermal annealing process, leading to the decrease in FWHM (as shown in Figure 4.25(a)) and blue-shift of the stretching peak position (as shown in Figure 4.25(b)). This phenomenon can be further observed from the results of the change in peak position and FWHM presented in Figure 4.26. It is known from the literature that oxygen absorption during annealing process can lead to the blue-shift of the stretching peak position. Also, SiO_x films deposited at higher η, as discussed previously, are dominated by silicon content. Thus, the change in stretching peak position is observed to be the biggest at highest η of 40, as shown in Figure 4.26. The evidence points to the likelihood that more oxygen from air is absorbed into the film during the annealing process, leading to the tendency of stoichiometry SiO_2 film formation.

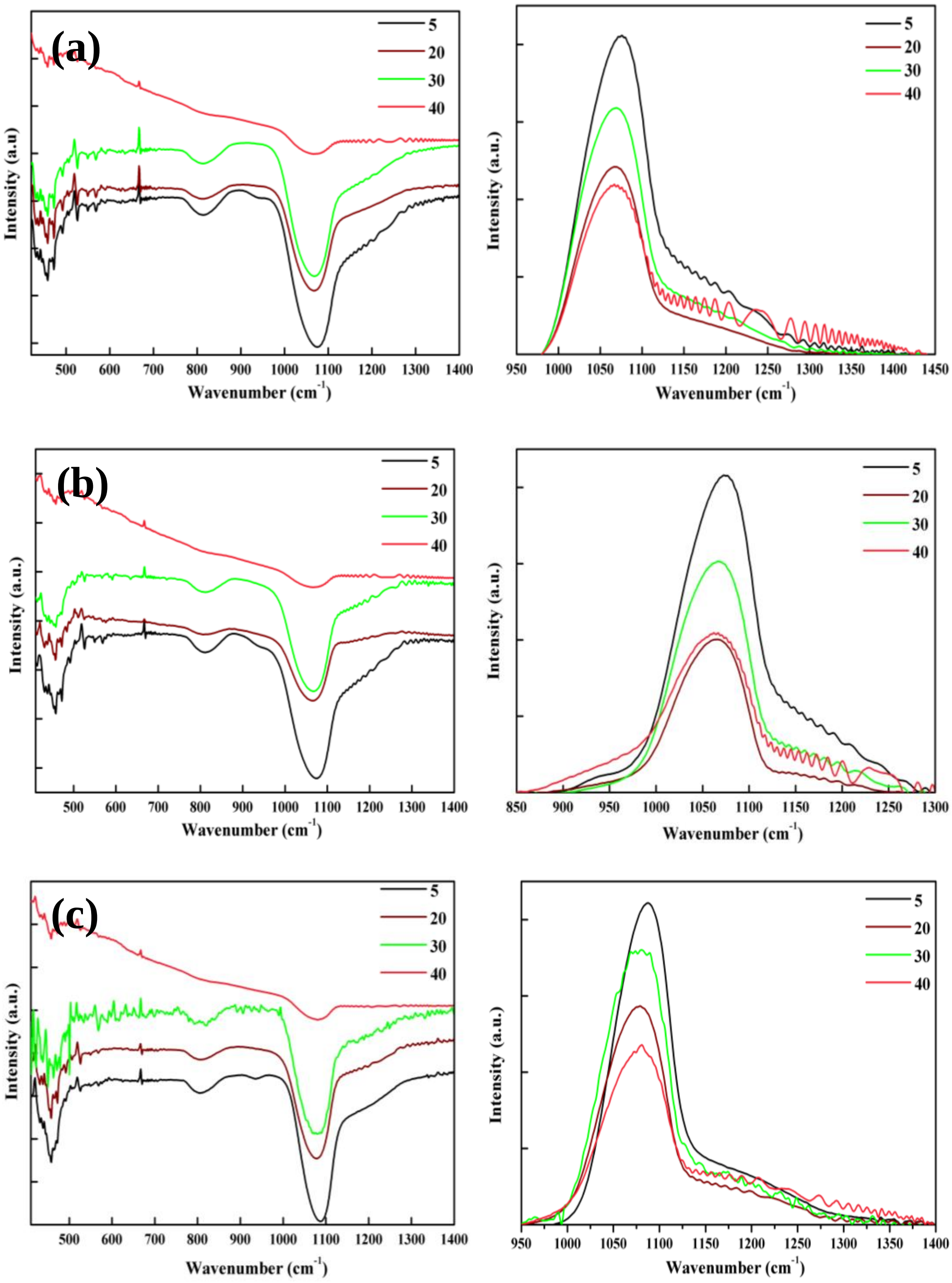

Figure 4.23: Infrared transmittance spectra of (a) SiO_x films, (b) as-deposited Au/SiO_x films and (c) annealed Au/SiO_x films deposited at different N_2O/SiH_4 flow rate ratios.

On the other hands, biggest change in FWHM is observed on the oxygen and silicon content dominant SiO_x film while the smallest change is observed on film prepared at η = 20. It appears that the structural order of SiO_x film is more easily enhanced by the Au particles on silicon or oxygen content dominant films after annealing process. However, the detailed mechanism behind this phenomenon still remains unknown. Thus, it is advised that care should be taken on the effect of Au NPs on the structural order of the SiO_x film in future.

In general, it is known that the oxygen content increases as the peak position of stretching mode shifts to lower wavelength. Thus, the as-deposited SiO_x film prepared at lowest η in this work has highest O/Si atomic ratio. It correlates with the results of depth profiling analysis, measured by using Auger electron spectroscopy (AES), which indicated that the x of SiO_x film prepared at η of 5, 20, 30 and 40 are 0.68, 0.47, 0.61 and 0.38 respectively.

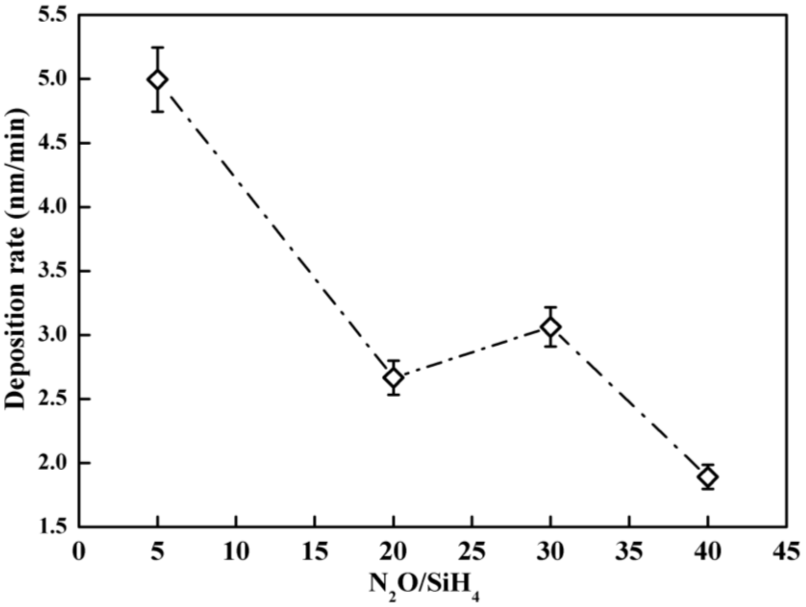

Figure 4.24: Variation of deposition rate of SiO_x films deposited as a function of N_2O/SiH_4 flow rate ratio.

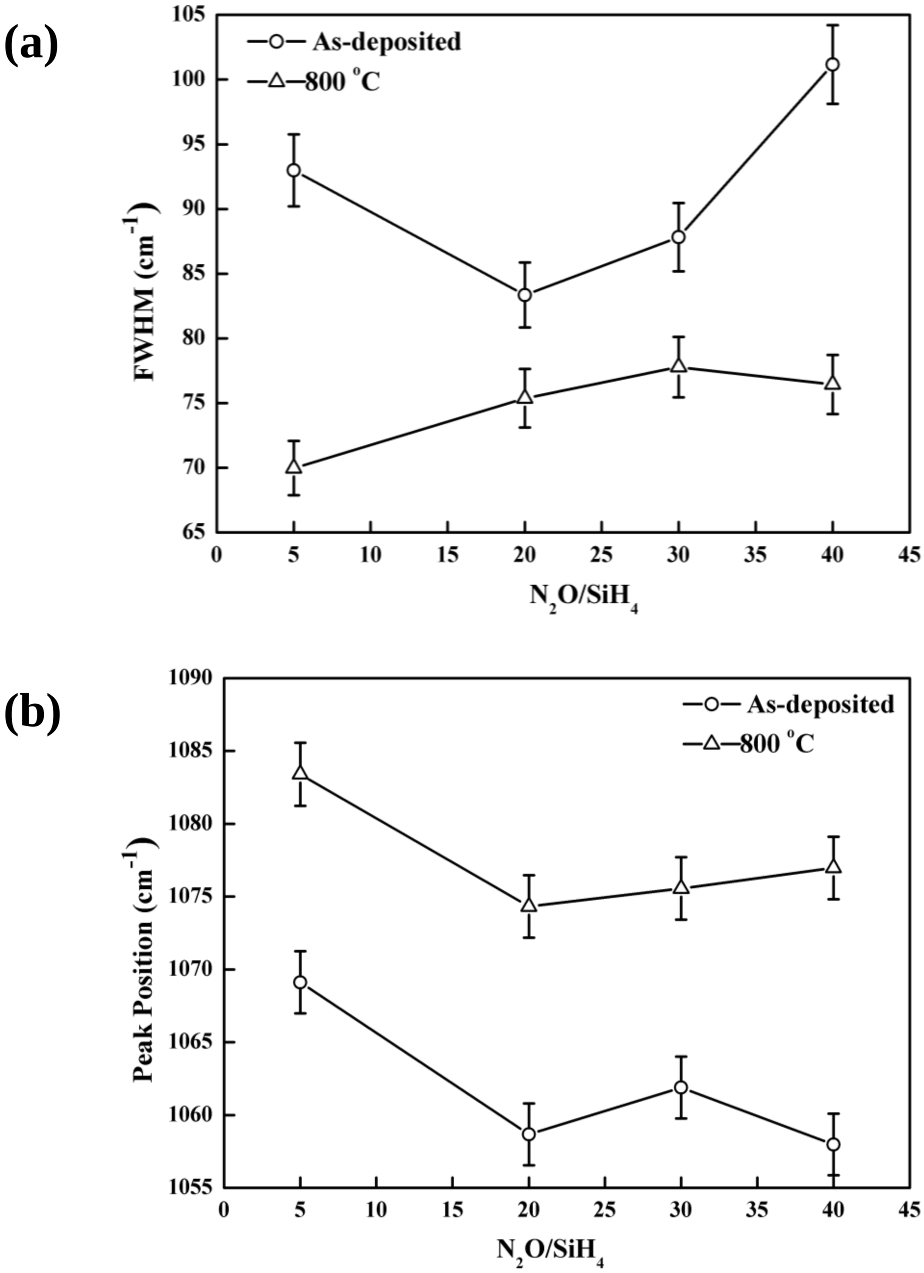

Figure 4.25: Variations of (a) full-width at half-maximum (FWHM) and (b) peak position of the Si-O-Si stretching modes for the as-deposited and annealed Au/SiO$_x$ films.

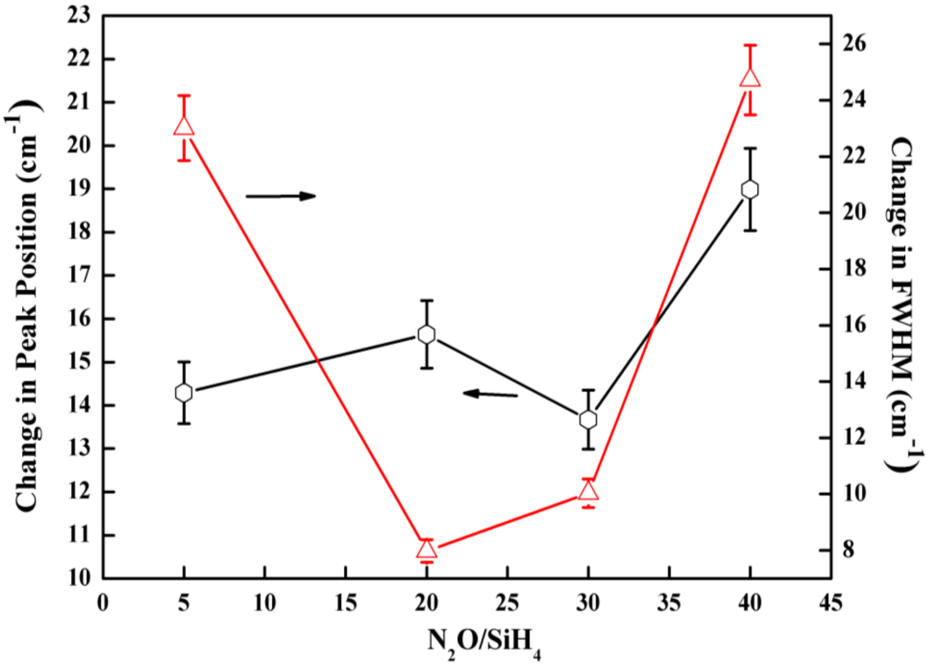

Figure 4.26: Variations of change in stretching peak position and FWHM

(c) X-ray Diffractometry (XRD)

XRD spectra of the as-deposited and annealed Au/SiO$_x$ films are presented in Figure 4.27. All the as-deposited Au/SiO$_x$ films show broad Au diffraction peaks at 38.2 ^{o}, 44.4 ^{o}, 64.6 ^{o} and 77.5 ^{o} corresponding to Au (111), Au (200), Au (220) and Au (311) crystalline planes, respectively. This indicates that the samples are polycrystalline in nature, whereas, the SiO$_x$ films are amorphous in structure since there no SiO$_x$ crystalline peaks have been observed from the spectra. Furthermore, all the Au diffraction peaks of the samples become sharper and increase in intensity after thermal annealing process, indicating the improvement of crystallinity and increment in crystallite size of the Au particles.

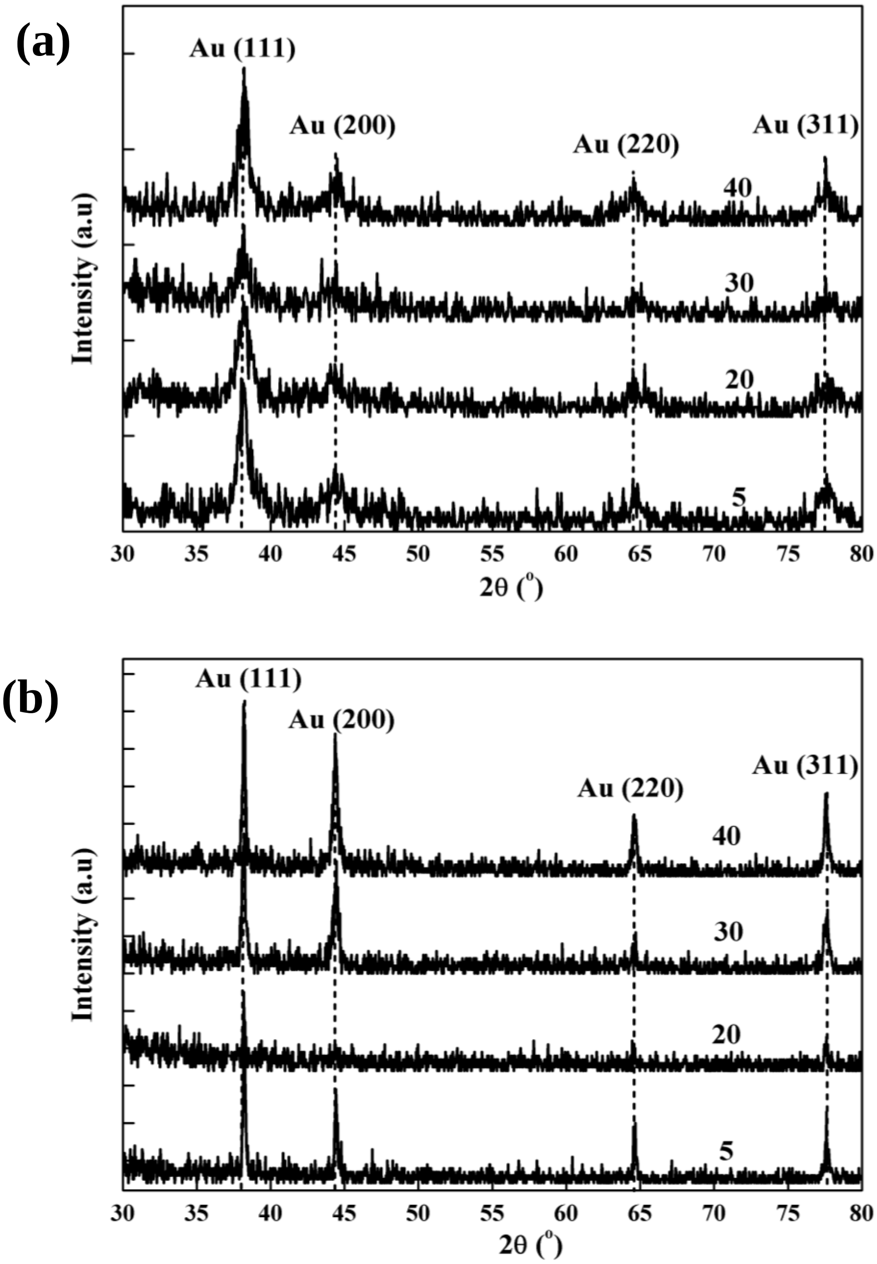

Figure 4.27: XRD spectra of (a) as-deposited Au/SiO$_x$ films and (b) annealed Au/SiO$_x$ films deposited at different N_2O/SiH_4 flow rate ratios.

The average Au crystallites size was estimated using Scherrer equation *(Devadason and Muhamad, 2007),*

$D = (0.9\ \lambda)/\ (B \cos \theta)$

where λ is the X-ray wavelength, θ is the Bragg diffraction angle and B is the full-width at half-maximum (FWHM). The estimated average crystallite sizes are tabulated in Table 4.1.

The results clearly demonstrate that the Au crystallites size enlarge after annealing process and differ with the SiO_x films prepared at different η. It supports the results of FESEM image shown in Figure 4.22.

Table 4.1: Crystallites sizes of Au formed on the surface of the as-deposited Au/SiO_x films and Au/SiO_x films annealed temperature of 800 ^{o}C.

N_2O/SiH_4 flow rate ratios		**Crystallite size (nm)**			
		Au(111)	**Au(200)**	**Au(220)**	**Au(311)**
As-prepared samples	5	11.5	5.8	8.7	7.7
	20	8.6	9.9	6.0	4.7
	40	10.4	7.0	8.1	8.0
	30	11.0	10.6	6.1	8.1
Annealed samples	5	45.6	39.4	45.6	27.2
	20	63.6	85.5	48.7	61.1
	30	29.5	18.3	24.6	24.0
	40	37.1	21.1	28.1	32.0

(d) Ultraviolet-Visible-Near Infrared (UV-VIS-NIR)

In order to understand the characteristic of SPR peak induced by Au particles, the transmittance and reflectance spectra of the as-prepared Au/SiO_x films deposited at different η on quartz substrates and its annealed Au/SiO$_x$ films at 800 ^{o}C are obtained using spectrophotometer and presented in Figure 4.28.

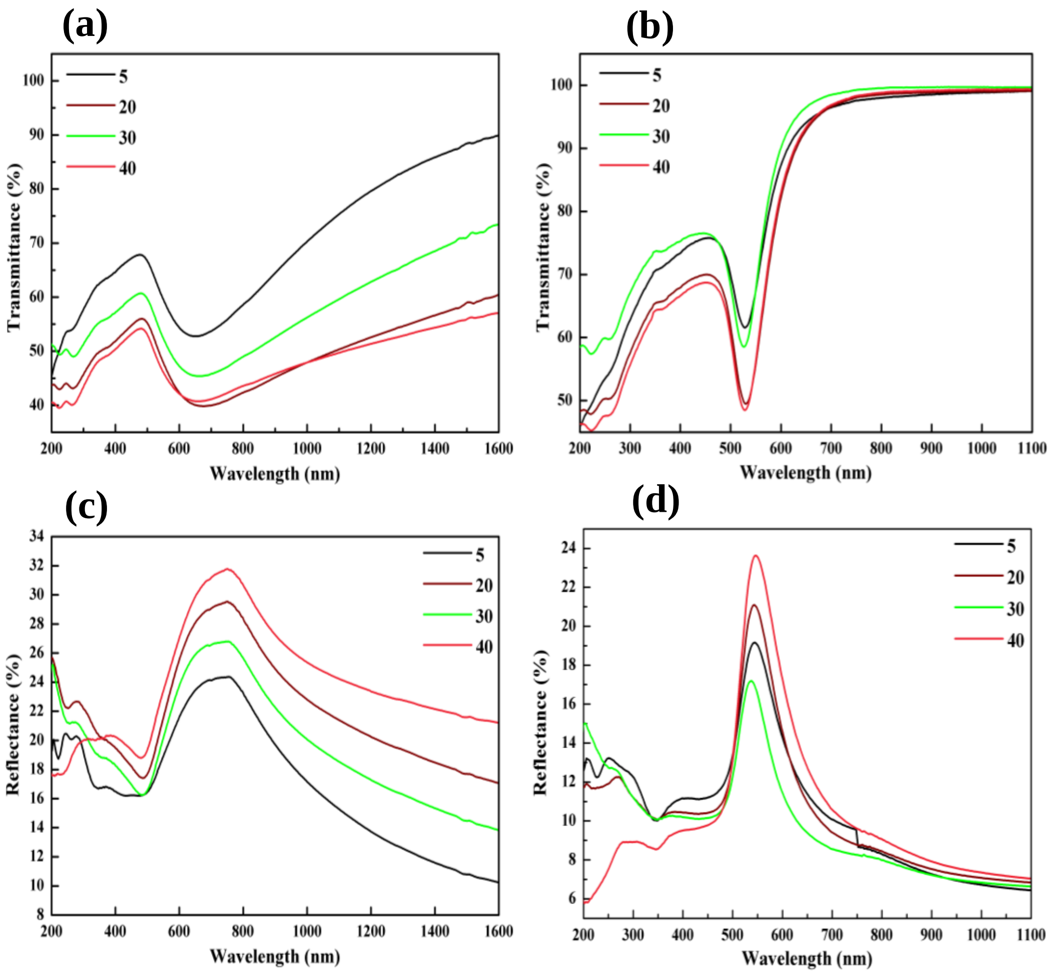

Figure 4.28: Transmittance and reflectance spectra of (a) & (c) as-deposited Au/SiO$_x$ films and (b) & (d) annealed Au/SiO$_x$ films deposited at different N$_2$O/SiH$_4$ flow rate ratios.

The absorption coefficient, α of the films were determined from both the transmittance and reflection spectra, as presented in Figure 4.29, using the expression *(Al-Kuhaili 2008)* $T = (1-R)e^{-\alpha d}$, where $\alpha = \frac{1}{d} ln\left(\frac{1-R}{T}\right)$ and d is the thicknesses of the samples which were determined from d is the thicknesses of the samples which were determined from depth profiling.

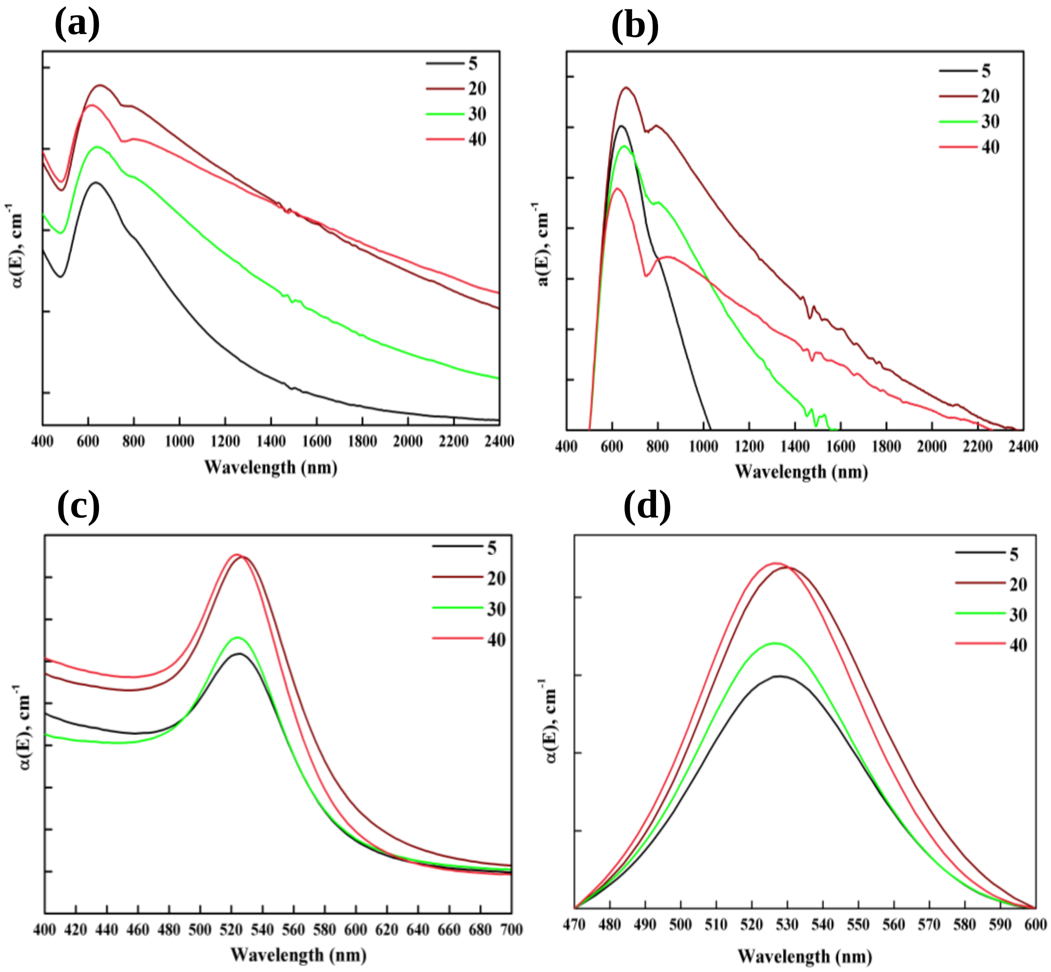

Figure 4.29: Absorption coefficient spectra and fitted SPR peak of (a) & (b) as-deposited Au/SiO$_x$ films and (c) & (d) annealed Au/SiO$_x$ films deposited at different N$_2$O/SiH$_4$ flow rate ratios.

It is observed that all the as-deposited Au/SiO$_x$ films exhibit SPR peaks at around 600 to 650 nm, as shown in Figure 4.29(a). These SPR peaks blue-shift and become narrowed and increased in intensity after thermal annealing process at 800 ^{o}C for one hour. This phenomenon can be attributed to the formation of Au particles from continuous Au films. It is also known from the literature that the bigger size of Au particles appearing on the film might lead to higher intensity of the SPR peak compared to the smallest size of Au particles, for instance, observed on the film deposited at η = 30. However, it is interesting to observe that the annealed samples deposited at η = 40 and 5 have the highest and lowest intensity of SPR peak respectively, which is inconsistent with the FESEM image shown in Figure 4.22.

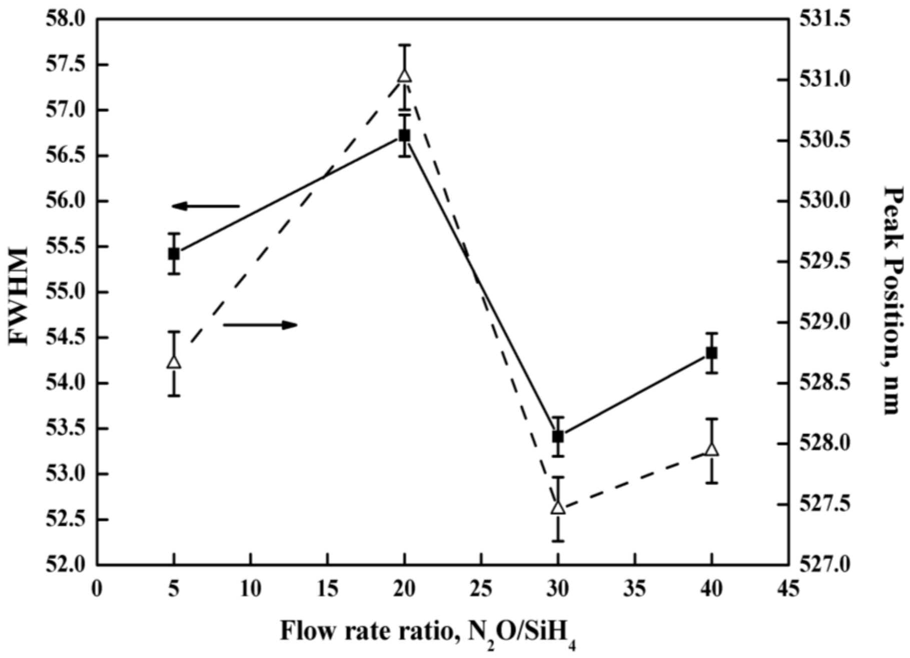

Figure 4.30: Variation of FWHM and peak position of SPR peak of annealed Au/SiO_x films as a function of N_2O/SiH_4 flow rate ratios.

In order to investigate this phenomenon in detail, we fitted the SPR peak and plotted the graph of FWHM and peak position of SPR peak against flow rate ratio of N_2O to SiH_4, as shown in Figure 4.30. Apparently, FWHM and peak position of the SPR peaks correlate very well with the size of Au particles. It indicates that the narrower the FWHM of the SPR peak, the smaller the Au particles. Apart from that, bigger size of Au particles will lead to the red shift of the SPR peak. In our work, therefore, it is likely that FWHM and peak position instead of intensity of the SPR peak is the dominant factor to correlate with the size of particles.

4.3.3 Hot Wire Evaporated Au Layer on SiO_x Film

4.3.3.1 Role of SiO_x Film to the Growth of Au NPs

(a) Field Emission Scanning Emission Microscopy (FESEM)

Based on the results shown in the previous sub-chapter, it is known that the optimal flow rate ratio of N_2O to SiH_4 is 30 for the deposition of SiO_x films, which can be used to effectively inhibit the agglomeration of Au NPs. Therefore, SiO_x film fabricated with flow rate ratio of 30 was coated with Au using hot wire evaporation technique. In general, the problem of inefficient evaporation process due to uncontrollable evaporation time of Au could result in the drop of larger size of Au droplets towards the surface of substrates when the Au wire starts to melt. In order to address this problem, minor modification on the hot wire evaporation technique was made. A shutter was fitted to the homebuilt chamber to control the evaporation time of the Au. Using this improved technique, the role of SiO_x film that serve as dielectric matrix in the growth of Au NPs was studied. Also, further comparison will be made between samples of Au on SiO_x film and Au on bare silicon substrate.

To start with, Au is evaporated onto the surface of bare silicon substrate and SiO_x films and the FESEM images are presented in Figs. 4.31(a) and (b) respectively. It appears that agglomeration of Au NPs can be prevented effectively as Au NPs are supported ON the surface of SiO_x film. The size of Au NPs is observed in the range from 1.9 to 77 nm. For the Au evaporated on the surface of bare silicon substrate, Au is miscible with silicon and a multitude of Au_xSi_y compounds is believed to be produced by thermal reaction since the higher annealing temperature of 800^{o}C is applied *(Mohapatra et al., 2008)*. It has been known that metals, like Au, tend to diffuse into the silicon substrate with surface energy depending on the structure of silicon and interface between silicon and metal *(Bruno et al., 2010a; Mohapatra et al., 2008)*. It is reported that the surface energy for silicon is (0.78 J/m^2) lower than SiO_x (1.5 J/m^2) *(Bruno et al., 2010)*. Thus, the higher formation energy of particle nuclei on SiO_x than on c-Si inhibits further Au NPs nucleation. Thus, it is widely accepted that SiO_x may acts as a good diffusion barrier to refrain Au nucleation.

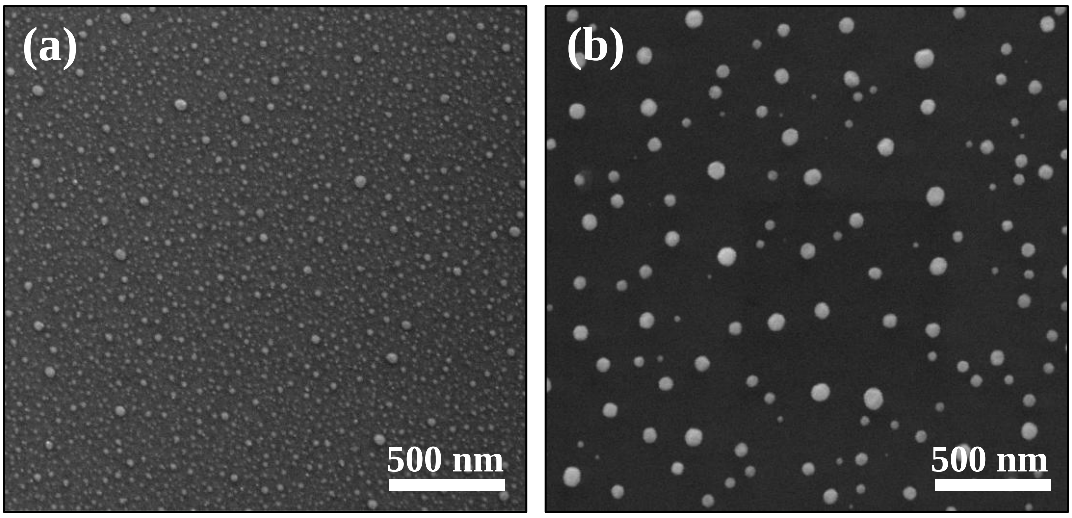

Figure 4.31: FESEM image of (a) annealed Au/Si film and (b) annealed Au/SiO$_x$ film.

(b) Fourier Transform Infrared (FTIR)

The IR spectra of Au/Si and Au/SiO$_x$ film are shown in Figures. 4.32 (a) and (b) respectively. It has been known that there are three regions of absorption bands which can be identified at 460 cm^{-1}, 816 cm^{-1} and 1080 cm^{-1} corresponding to the rocking, bending and stretching vibrational modes of the Si-O-Si band, respectively *(Kirk, 1988)*. For the as-deposited Au/Si film, there are no vibrational modes of the Si-O-Si band can be observed since the composition of this sample consists of Au and silicon only. As the as-prepared Au/Si film is post-thermal annealed at 800 ^{o}C for 1 hour in N$_2$ ambient, Si-O-Si stretching peak can be observed. It is highly probable that oxygen incorporation occurs during the annealing process since the tube furnace is not in vacuum condition.

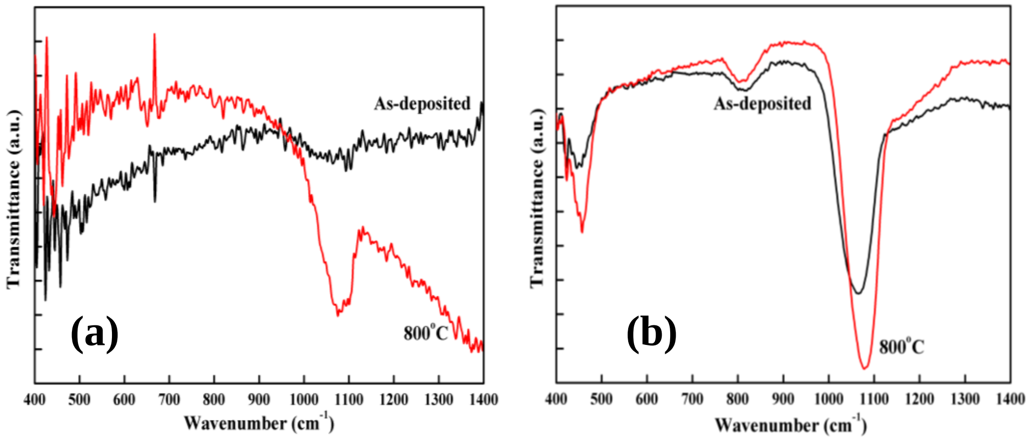

Figure 4.32: IR spectra of (a) as-deposited and annealed Au/Si film and (b) as-deposited and annealed Au/SiO$_x$ film

For as-deposited Au/SiO$_x$ film, sharp rocking, bending and stretching peak can be clearly observed. These Si-O-Si absorption peaks are found to increase in intensity and narrow in FWHM after annealing process. The position of Si-O-Si stretching peak tends to shift to higher energy, indicating the increase in amount of oxygen content in the samples. From the previous discussion, oxygen content can come from SiO$_x$ or air. Si-O is easier to form at higher annealing temperature. On the whole, incorporation of oxygen content can contribute to the increase in intensity and narrow in FWHM of the Si-O-Si absorption peak, respectively, besides the blue-shift of the Si-O-Si stretching peak position.

(c) X-ray Diffractometry (XRD)

Figure 4.33 presents the XRD spectra of as-prepared and annealed Au/Si films and annealed Au/SiO$_x$ film. It appears that there is no Au diffraction peak observed on the as-prepared and annealed Au/Si films. This result implies that Au film supported ON silicon substrate is difficult to grow into the crystallite structure even though higher annealing temperature is applied. It is results from the fact that the Au atoms have not coalesced enough due to the formation of Au-Si alloy decorated with only a few pure

Au nanocrystallites, which are too small to be detected. In addition, there is also not any Au diffraction peak observed on the as-prepared Au/ SiO_x film, which is not shown here. Au diffraction peak with orientation plane of (111) and (311) can be clearly observed after thermal annealing process at 800 °C is carried out. It appears that SiO_x film, which is a diffusion barrier, prevents the Au from diffusing into the silicon substrate, leading to the formation of pure Au crystallites instead of Au-Si alloy. By comparing the peak intensity of Au (111) and Au (311), we know that the Au crystallites have a favorable texture structure along the <111> direction.

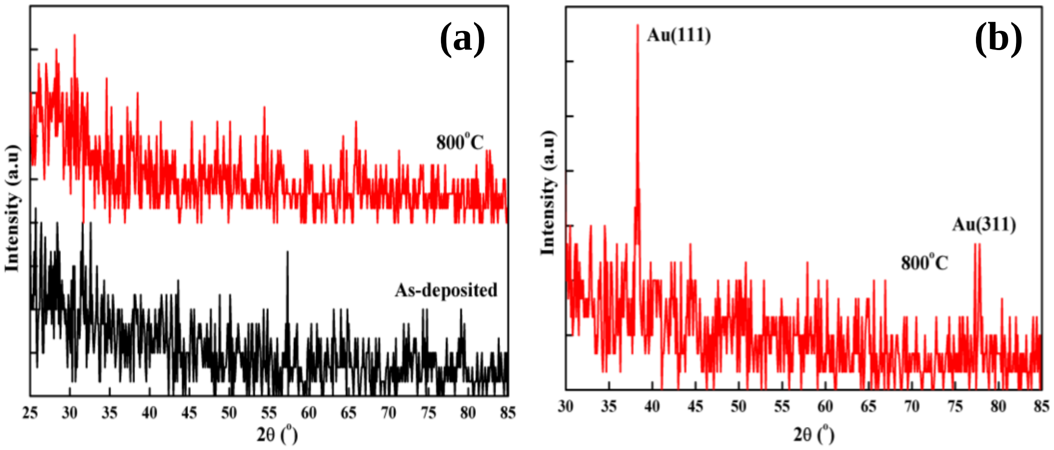

Figure 4.33: XRD spectra of (a) Au/Si film and (b) Au/SiO_x film

(d) Ultraviolet-Visible-Near Infrared (UV-VIS-NIR)

Figure 4.34 displays the blue-shift in position and narrow in full width at half maximum (FWHM) of the SPR peak after thermal annealing process. As Au is evaporated onto the silicon substrate at room temperature, Au layer exists. Thus, a very broad SPR peak is observed at around 600 nm. After thermal annealing process at 800 °C for 1 hour, there are two prominent peaks observed. Noble metal is known to exhibit inter-band (*d* band to *s-p* conduction band) transition at shorter wavelength and intra-band (free electron) transition at longer wavelength. Thus, absorption peak located at

UV region, which is around 280 nm and VIS region, which is around 520 nm can be related to *5d* to *6sp* inter-band transition and surface plasmon resonance (SPR) effect of Au NPs, respectively *(Shin et al., 2003; Xie et al., 2010)*. FWHM of SPR peak becomes narrower and tends to blue-shift to lower wavelength as the size of Au NPs enlarges after being annealed at high temperature.

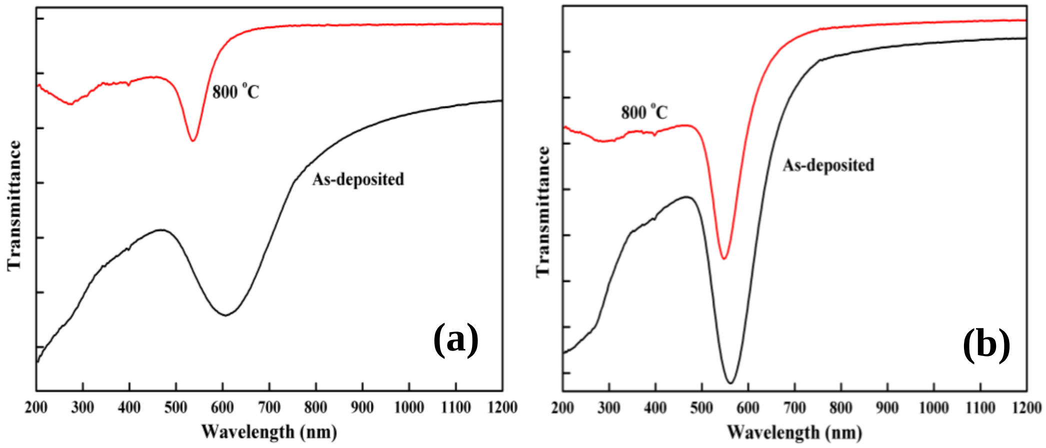

Figure 4.34: Optical transmittance spectra of (a) as-deposited and annealed Au/Si film and (b) as-deposited and annealed Au/SiO$_x$ film

For Au supported ON SiO$_x$ film as shown in Figure 4.34(b), a high intensity of SPR peak can be clearly observed to locate at around 580 nm for as-deposited Au/SiO$_x$ films. It appears that SPR effect is very strong in this work. SiO$_x$ film acts as a good diffusion barrier here to prevent Au from diffusing into silicon substrate, resulting in the formation of pure Au layer on surface of SiO$_x$ film. After thermal annealing process, absorption peak at UV region can be observed at around 280 nm but with a lower intensity if compared to the Au/Si film. It is believed that intra-band transition is the dominant transition in Au/SiO$_x$ film, as seen from the higher intensity of SPR peak in VIS region. SPR peak is found to become narrower and tend to blue shift to around 550 nm as the size of Au NPs becomes bigger. From these discussions, it is safe to say that the weak Au-SiO$_x$ chemical interactions allow the investigation of the morphology of Au NPs as a function of the processing condition. At the same time, the peak position and intensity of SPR peak can be well tuned by controlling the size and distribution of Au NPs for some practical uses.

4.3.3.2 Effect of Heated SiO$_x$ film on the growth of the Au NPs

(a) Field Emission Scanning Emission Microscopy (FESEM)

Using shutter to control the evaporation time of Au and its size and distribution has been proven to be successful. Therefore, effect of the heated SiO$_x$ film on the growth of Au NPs is studied to obtain better control on the size of Au NPs. Figure 4.35 presents the FESEM image of the as-prepared and annealed Au/SiO$_x$ film on quartz substrates. It shows a relatively uniform size distribution of Au NPs supported ON the SiO$_x$ films. The size of Au NPs ranges from around 5.2 to 10.8 nm. Due to the advantage of this proposed technique, smaller sizes of Au NPs with narrow size distribution can be easily obtained through this one-step process [the whole fabrication process of Au/SiO$_x$ film was carried out in the same vacuum chamber without taking out the SiO$_x$ film for Au evaporation using DC sputter coater]. Since the as-prepared Au/SiO$_x$ films were continuously heated at 300 ^{o}C in vacuum condition for 1 hour just after the Au evaporation, the effect of air contamination can be reduced to the minimum. Thus, the as-prepared Au/SiO$_x$ films will not be easily oxidized. It has been mentioned earlier that SiO$_x$ film can effectively block the agglomeration of Au NPs. Therefore, without the excess oxide appearing on the Au film, Au atoms have more mobility and energy to aggregate with each other to form nanosized Au particles easily. Besides that, heater rod is used to be the heating element in this work. Heater rod is inserted between the substrate holder and holder stand, as shown in Figure 3.11. Thus, this heating technique is quite different from conventional thermal annealing technique using tube furnace. Heating technique using heater rod can be considered as direct heating. Unlike thermal annealing technique using tube furnace where the heat or energy is transferred from all directions, the heat or energy is transferred to the samples from the bottom when heater rod is used. Therefore, the heat or energy gained by the samples will be more concentrated and straightforward. In addition, the effect of vacuum condition results in the inefficiency of heat or energy dissipation to the surrounding environment. This situation can promote the growth of Au NPs even with lower temperature.

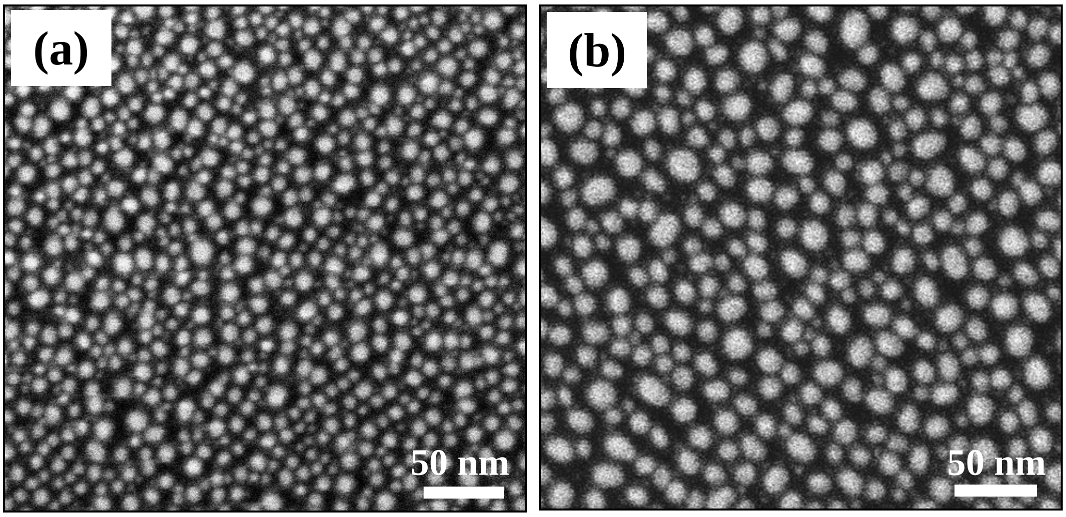

Figure 4.35: FESEM image of (a) as-prepared Au on SiO_x films heated at 300 ^oC and (b) sample after thermal annealing at 200 ^oC for 1 hour.

The as-prepared Au/SiO_x films were then taken out of the vacuum chamber and put into a tube furnace for thermal annealing process at 200 ^oC in nitrogen ambient for 1 hour. The FESEM image of the annealed sample is presented in Figure 4.35 (b). It is interesting to note that the size of Au NPs has become relatively larger. The sizes of Au NPs range from around 5.3 to 17.2 nm. Compared to previous thermal annealing process where the minimum annealing temperature adopted to induce the growth of Au NPs was 400 ^oC, results shown here provide a lower thermal annealing temperature process to promote the growth of bigger size Au NPs with uniform size distribution. It may be reasonable to suppose that Au NPs gain the required energy from annealing temperature to promote its size. In this work, it has been proven that we can use the PVD method instead of conventional chemical method to produce the smaller size of

Au NPs besides controlling its size precisely using simple thermal annealing technique. By doing so, we can apply it in many industrial fields which require plasmonic technology such as optoelectronic and solar cell.

(b) Fourier Transform Infrared (FTIR)

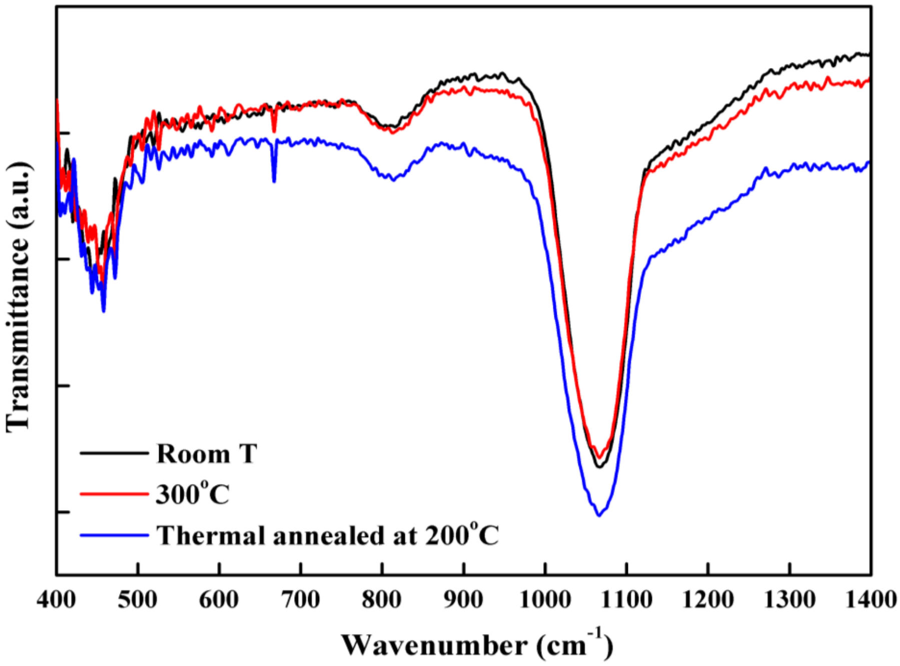

Figure 4.36: IR spectra of as-prepared Au on SiO$_x$ films prepared at room temperature and heated at 300 ^{o}C. The latter sample was then annealed at 200 ^{o}C.

The IR spectra shown in Figure 4.36 are in exceptionally good agreement with the FESEM results. Three regions of absorption bands can be identified at 460 cm^{-1}, 816 cm^{-1} and 1080 cm^{-1}, which correspond to the rocking, bending and stretching vibrational modes of the Si-O-Si band, respectively *(Kirk, 1988)*. The FWHM and intensity of these absorption vibrational peaks become slightly broader and decreased, respectively, after thermal annealing process was carried out. It appears that the oxygen content of the as-prepared samples has increased during thermal annealing process at 200 ^{o}C.

At higher temperature, oxides from SiO$_x$ or air become easier to bond to Si, resulting in the broadening of FWHM of Si-O-Si stretching peak. To have a good comparison, a reference sample, where the Au was evaporated on the SiO$_x$ film at room temperature without any continuous substrate heating, was used. Apparently, the IR spectrum of the reference sample is almost the same as the spectrum of as-prepared Au/SiO$_x$ films prepared at substrate temperature of 300 ^{o}C. It can be attributed to the fact that the parameters used to deposit SiO$_x$ films in this work are always the same, leading to the same structural characteristic. Besides that, Au evaporation and continuous heating process afterwards were carried out in a high vacuum condition. In this way, the oxygen incorporation into the samples can be reduced to the minimum. As mentioned previously, the suppression of Au film on the oxide characteristic of SiO$_x$ film can be clearly observed through the change in FWHM and intensity of Si-O-Si absorption peak. However, in this work, thickness of the Au film evaporated is very thin, ranging from 10 to 15 nm. Thus, the effect of suppression of Au film can be neglected here since it has no effect on Au/SiO$_x$ films prepared at room temperature and substrate temperature of 300 ^{o}C, as shown in Figure 4.36.

(c) X-ray Diffractometry (XRD)

Figure 4.37 presents the XRD spectra of as-prepared Au on SiO$_x$ films prepared at room temperature and heated at 300 ^{o}C and annealed Au on SiO$_x$ film heated at 300 ^{o}C. It appears that no Au diffraction peak is observed on the Au on SiO$_x$ film prepared at room temperature. It may be recognized that only Au film is formed on the surface of SiO$_x$ film since the heating process is not carried out yet. Au atoms do not gain enough energy and mobility to coalesce due to temperature-dependent diffusion. When the Au, however, is evaporated onto the SiO$_x$ film heated at 300 ^{o}C, Au crystallites with the size of 5.5 nm are ready to form. The size of Au crystallites can be estimated using Scherrer's equation,

$$D = (0.9\ \lambda)/\ (B \cos \theta)$$

where λ is the X-ray wavelength, θ is the Bragg diffraction angle and B is the full-width at half-maximum (FWHM).

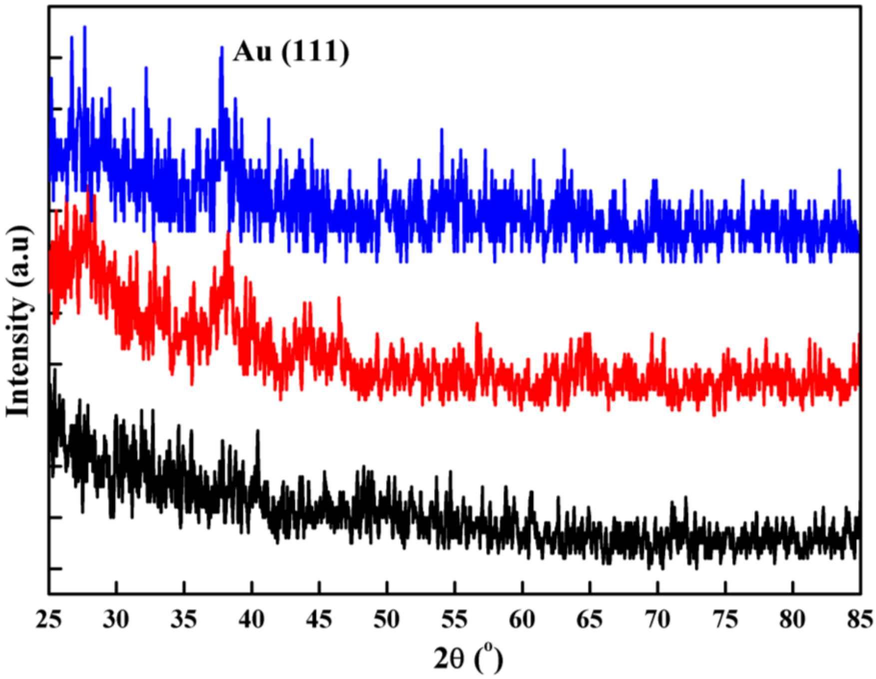

Figure 4.37: XRD spectra of as-prepared Au on SiO_x films prepared at room temperature (black line) and heated at 300 °C (red line) and annealed Au on SiO_x film heated at 300 °C (blue line).

As seen from Figure 4.37, only diffraction peak of Au with orientation of (111) can be observed. It has been known from the literature that (111) surface energy of fcc metals such as Au is the lowest as compared with both (100) and (110) planes *(Qiu et al., 2004)*. Thus, Au nuclei in (111) orientation should be nucleated at the initial stage of film growth as they have lower energy which is the sum of surface energy, interfacial energy and volume free energy *(Qiu et al., 2004)*. Thus, it may be reasonable to indicate that (111) is the most favorable orientation for the Au crystallites to grow under moderate temperature in this work. As the sample is subsequently thermal annealed at 200 °C for 1 hour in N_2 ambient, the intensity of Au (111) diffraction peak is observed to increase with the narrower of FWHM of the peak as discussed previously, indicating that the enlargement of grain or crystallite size is temperature-dependent. The size of the Au crystallites is found in the range of 7.7 nm. It is observed that the grain or crystallite size obtained from Scherrer equation is always smaller than the actual one. It can be attributed to the fact that the formula does not involve peak broadening where the stress in film is considered *(Yu et al., 2005)*.

(d) Ultraviolet-Visible-Near Infrared (UV-VIS-NIR)

The optical properties of the Au/SiO$_x$ prepared under different conditions are investigated by the optical transmission and reflection spectroscopy. The transmittance and reflectance spectra of the as-prepared Au on SiO$_x$ films prepared at room temperature and heated at 300 ^{o}C and annealed Au on SiO$_x$ film heated at 300 ^{o}C are presented in Figure 4.38. It is clearly observed that the transparency and reflectance of the samples in the near-infrared region decrease and remain almost constant, respectively, as the Au is evaporated onto the films prepared at higher temperature. It can be ascribed to the formation of Au NPs having characteristics of high absorption due to the induced SPR effect *(Liao et al., 2003; F. Ruffino & Grimaldi 2010; Sangpour et al., 2007; Yu et al., 2005)*. For the Au on SiO$_x$ film prepared at 300 ^{o}C followed by thermal annealing at 200 ^{o}C for 1 hour, the size of Au NPs becomes larger. At the same time, transparency of the sample in the near-infrared region becomes even lower. This may imply that bigger size of Au NPs can greatly enhance the absorption of EM wave. The transmittance of these three samples can be clearly seen in Figure 4.39.

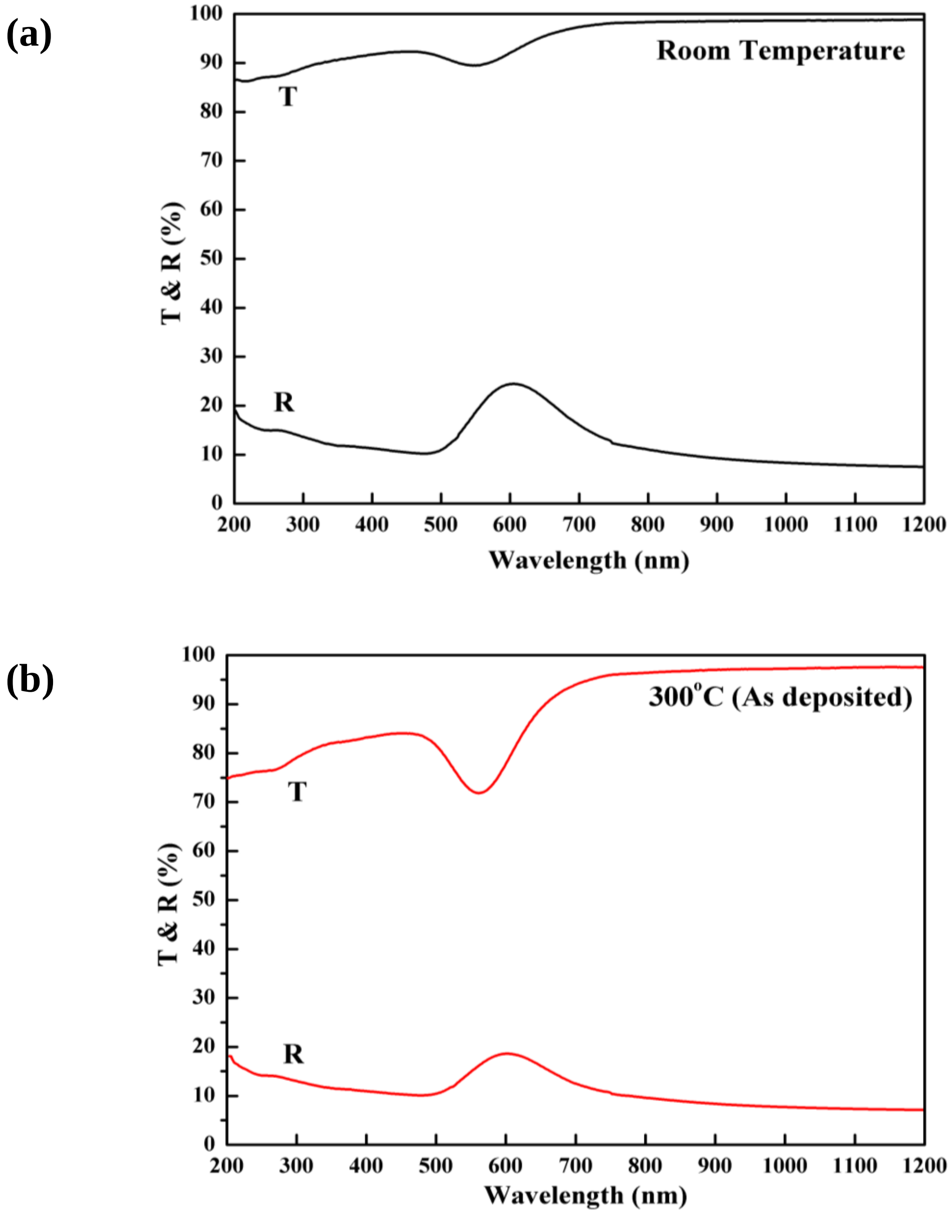

Figure 4.38: Optical transmittance and reflectance spectra of (a) as-prepared Au on SiO_x film prepared at room temperature, (b) as-prepared Au on SiO_x film heated at 300 ^{o}C and (c) annealed Au on SiO_x film heated at 300 ^{o}C.

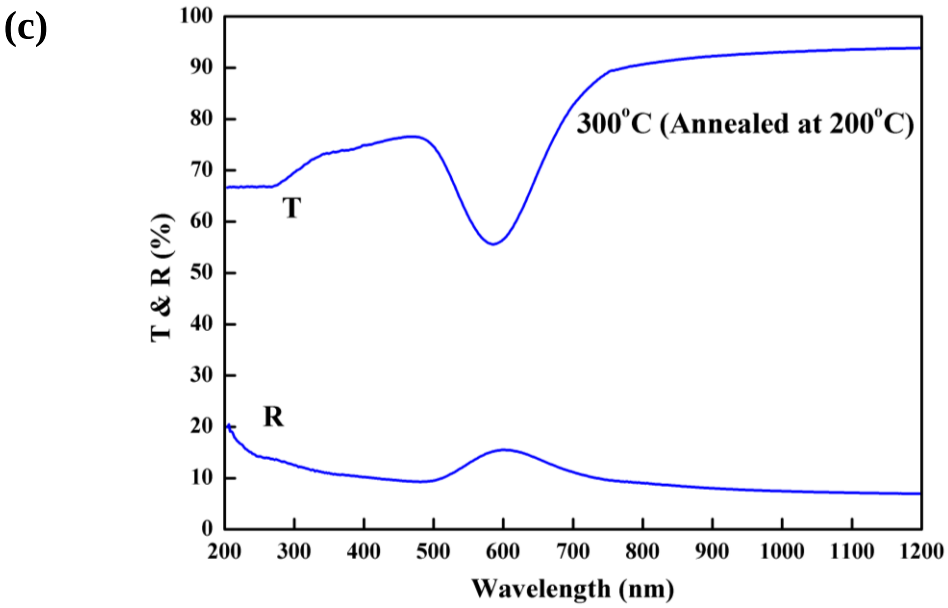

Figure 4.38, continued

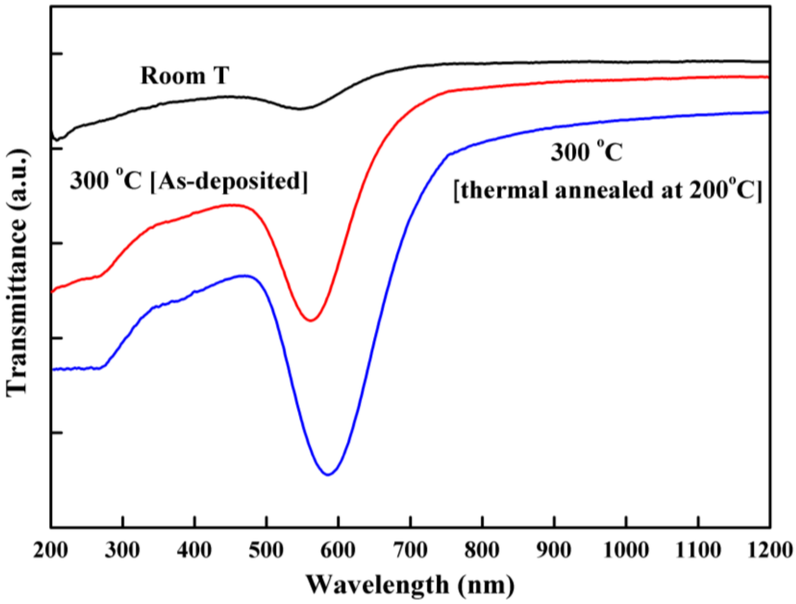

Figure 4.39: Optical transmittance spectra of as-prepared Au on SiO_x film prepared at room temperature, as-prepared Au on SiO_x film heated at 300 ^oC and annealed Au on SiO_x film heated at 300 ^oC.

To study the effect of surface plasmon resonance (SPR) attributed by Au NPs in details, the absorption coefficient of the annealed samples can be plotted against wavelength, as shown in Figure 4.40. The absorption coefficient, α, can be calculated from both transmittance and reflection spectra using the following expression *(Al-Kuhaili, 2008)* $T = (1-R)e^{-\alpha d}$

where $\alpha = \frac{1}{d} ln\left(\frac{1-R}{T}\right)$ and d is the sample thickness, which was determined by the surface profiler.

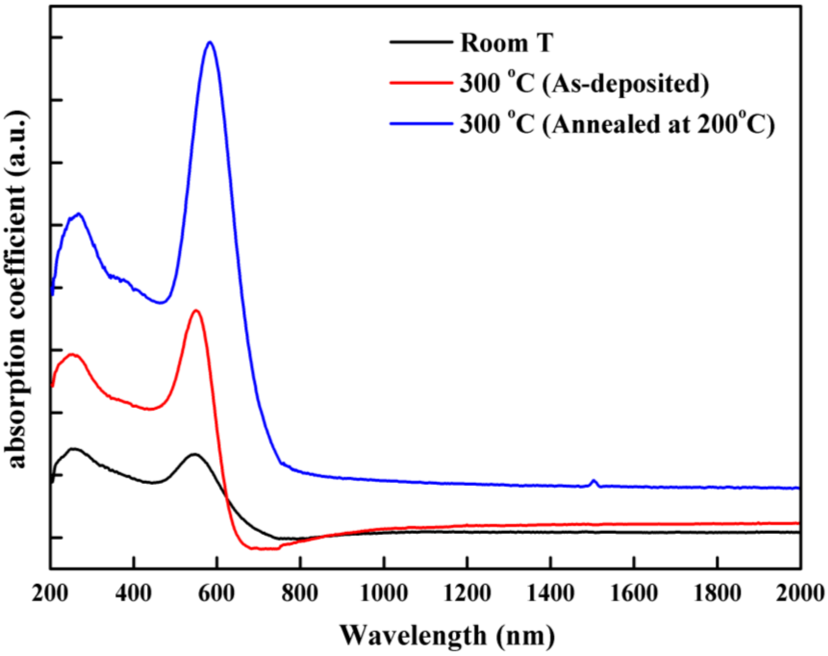

Figure 4.40: Graph of absorption coefficient against wavelength for as-prepared Au on SiO_x film prepared at room temperature, as-prepared Au on SiO_x film heated at 300 °C and annealed Au on SiO_x film heated at 300 °C.

In Figure 4.40, a prominent peak at around 240 to 270 nm can be observed in UV region for these three samples. The intensity of the absorption peak is found to increase with the substrate temperature and thermal annealing process. This absorption peak corresponds to the *5d* to *6sp* inter-band transition of Au NPs. It can be reasoned that the gold’s *5d* electrons are excited to the 6*sp* band and many of the excited electron are at high energy level when the Au NPs absorb UV irradiation *(Bruno et al., 2010; Mohapatra et al., 2008)*. In addition, the well-known surface Plasmon (SP) peak is observed at around 580 nm in visible region. It is known from the other works that the 6*sp* electron gains energy and migrates to higher intra-band energy level as the Au NPs absorb visible light through surface Plasmon resonance (SPR) effect. The Plasmon, soon after the light irradiation, heats the electron gas to an elevated temperature (about 400 to 2000 K) within a time scale of the order of 100 fs or less through electron-electron collision *(Zhu et al., 2009)*. During the process, gold electron gas obeys the Fermi-Dirac distribution at an elevated temperature. It is also interesting to mention that the graph of absorption coefficient against wavelength correlate very well with the absorption data directly obtained from the UV-VIS-NIR spectrophotometer as shown in Figure 4.41.

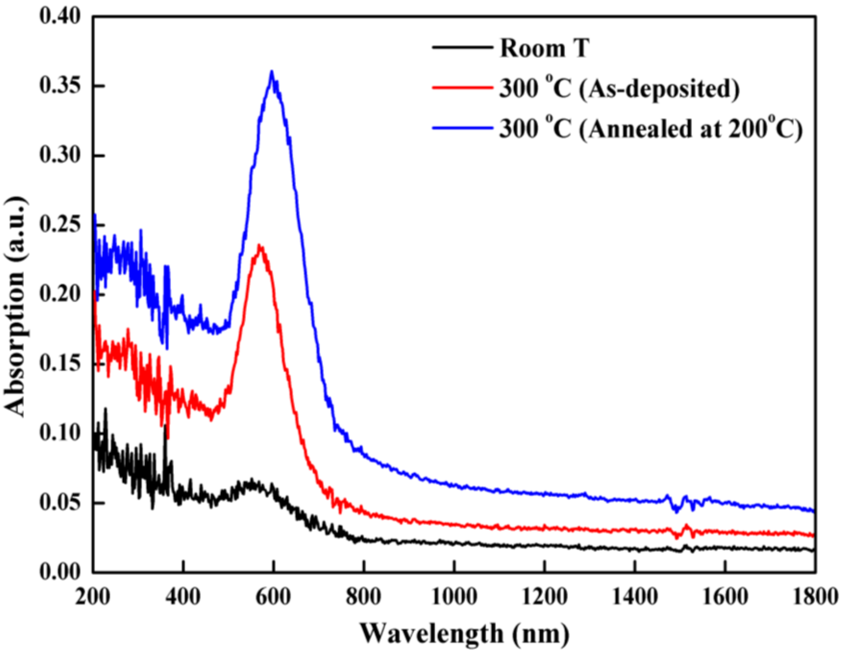

Figure 4.41: Absorption spectra of as-prepared Au on SiO_x film prepared at room temperature, as-prepared Au on SiO_x film heated at 300 °C and annealed Au on SiO_x film heated at 300 °C.

The observation in Figure 4.41 highlights the red-shift in position and increase in intensity of the SPR peak. As Au is evaporated onto the SiO_x film at room temperature, Au atoms do not have enough kinetic energy to coalesce into NPs, resulting in the formation of Au layer only. According to the previous work reported, Au NPs smaller than 2 nm in dielectric matrix are unable to exhibit SPR peak *(Jung et al., 2008; Sangpour et al., 2007; Yu et al., 2005)*. It is also known from the literature that the SPR effect induced by metal NPs can be influenced by four factors, which are size, shape, and concentration of metal NPs, and dielectric function of surrounding materials *(F. Ruffino et al., 2008; F. Ruffino & Grimaldi 2010; Yu et al., 2005)*.

Thus, it is thought that the intensity of the SPR peak is also dependent on the size of Au NPs. As the size of Au NPs enlarges, the intensity of SPR peak becomes higher. It can be seen from the FESEM image of Au evaporated onto the film heated at 300 ^{o}C. In this case, Au atoms have enough energy and mobility to aggregate to form Au NPs. The as-prepared Au NPs on SiO_x film heated at 300 ^{o}C are then thermal annealed at 200 ^{o}C for 1 hour. The position of the SPR peak is found to red-shift to 600 nm besides the observation of higher intensity of SPR peak. This is consistent with FESEM image shown in Figure 4.35. Thus, it can be said that larger size of metal NPs with broader size distribution leads to an average SPR response. In general, the position, intensity and FWHM of the SPR peak are greatly dependent on the size and distribution of the Au NPs. Precise control on these parameters is of paramount importance for the control of structural and optical properties of Au NPs supported ON or embedded IN the dielectric matrices.

CHAPTER 5

CONCLUSION AND FUTURE WORKS

5.1 Conclusion

As a conclusion, Au/SiO$_x$ nanocomposite films have been successfully synthesized using physical vapor deposition (PVD) and chemical vapor deposition (CVD) techniques followed by the characterization onto the structural and optical properties of Au/SiO$_x$ films. Firstly, SiO$_x$ films were fabricated using the RF magnetron sputtering system followed by coating the Au onto the surface of SiO$_x$ films using DC sputtering system. This "supported ON" structure of Au/SiO$_x$ film demonstrated the agglomeration of a uniform dispersion of elongated and island-like Au particles within the SiO$_x$ matrix at low annealing temperature of 400 ℃. The size and shape of these Au particles increased and changed from island-like to spherical-like, respectively, as the annealing temperature increased. We observed the growth of closely packed nanowires at annealing temperature of 1000 ^{o}C. The growth of nanowires follows the solid-liquid-solid (SLS) mechanism. Nevertheless, more close-packed and aligned nanowires were observed on the film as the annealing temperature was further increased beyond 1000 ^{o}C. From FTIR spectra, we observed the increase of oxide characteristics of samples with annealing temperature by analyzing the vibrational modes of Si-O-Si bands that appear in the spectra. With the absorption peaks at1088 cm^{-1} and 1200 cm^{-1}, we can even deduce that the outer layer of the nanowires is coated with oxide, as compared with the results of Kirk published in 1988. This showed that the nanowires grown at 1000 ^{o}C are SiO$_x$ nanowire. Furthermore, we can observe the appearance of Au crystallites from XRD spectra and the crystallinity of Au/SiO$_x$ films increases as the temperature is increased up to 1000 ℃. Surface Plasmon resonance

(SPR) absorption peak of these Au NPs is located in range of 580 and 735 nm, as observed from optical spectra. We can conclude that the position and width of the SPR peaks are strongly dependent on the size and shape of the Au particles.

For a better comparison of the structural effects of Au/SiO$_x$ films towards the structural and optical properties, we successfully prepared SiO$_x$ films embedded with Au by co-sputtering silicon and gold target in Argon and oxygen ambient by using RF magnetron sputtering system alone. This has resulted in the "embedded IN" structure of Au/SiO$_x$ films. From FESEM images, there are no particles found on the surface of films at temperature of 400 °C. Au particles start to appear and distribute uniformly on the surface at 800 °C. Similar to the sample of Au on SiO$_x$ films, we observed the growth of closely packed nanowires at 1000 °C. However, the growth of these nanowires was degraded at a higher temperature beyond 1000 °C. In addition, oxide characteristic exhibited by the Au in SiO$_x$ films were not obvious although the samples had been annealed up to a higher temperature of 800 °C. Nevertheless, we can deduce that the outer layer of the nanowires is coated with oxide with the observation of absorption peaks at1088 cm^{-1} and 1200 cm^{-1} at 1000 °C. From XRD spectra, we did not observe any sharp diffraction peaks of Au with increasing temperatures from 400 to 1000 ^{o}C. We believed that the contribution from substrate to the diffraction has protruded to that of the contributions from Au/SiO$_x$ films. As for optical properties, we observed no SPR peak at 400 ^{o}C but they started to appear at 672 nm at 600 ^{o}C. Furthermore, SPR peak blue-shifted to 600 nm at 1000 ^{o}C. Below 1000 ^{o}C, we observed an increase in intensity of SPR peak with unchanged peak position. It was due to the increase in uniformity of the Au NPs. It supported the statement that SPR peaks are strongly dependent on the structural properties of the Au particles.

Here, we observed that the structural and morphological properties of Au NPs supported ON SiO$_x$ films were more interesting in addition to the ease in control as compared to that of Au NPs embedded IN SiO_x films. We also switched our SiO_x preparation method to homebuilt plasma enhanced chemical vapor deposition (PECVD) system due to its advantages of low cost, simplicity and feasible. Preparation of Au remained unchanged by using DC sputtering method. Furthermore, a thin layer of gold (Au) was sputtered onto the surface of silicon oxide, SiO_x ($0.38< x< 0.68$) films which was deposited at different N_2O/SiH_4 flow rate ratios of 5 to 40 prior to the annealing process at constant temperature of 800 ^oC. FTIR spectra demonstrated the intensity and full-width at half-maximum (FWHM) of Si-O-Si and stretching peaks were significantly dependent on the N_2O/SiH_4 flow-rate ratio. The films deposited at low and high N_2O/SiH_4 flow rate ratio were dominated by the oxygen and silicon content respectively. The size and concentration of Au particles distributed on the surface of SiO_x films were dependent on the N_2O/SiH_4 flow-rate ratio. Higher concentrations of Au NPs were distributed evenly on the surface of the film deposited at N_2O/SiH_4 flow-rate ratio of 30. Crystallinity and crystallite sizes of Au were enhanced after thermal annealing process. Appearance of surface plasma resonance (SPR) absorption peaks at 524 nm for all samples was observed as a result of the formation of Au particles. The annealing process improved SPR peaks for all the as-deposited films. We also observed that the narrower the FWHM of the SPR peak, the smaller the Au particles. Larger size of Au particles will lead to the red shift of the SPR peak. In our work, it was likely that FWHM and peak position instead of intensity of the SPR peak was the dominant factor to correlate with the size of particles.

In addition, a new technique called plasma enhanced chemical vapor deposition assisted with hot wire evaporation technique was proposed and adopted to prepare Au NPs on SiO_x successfully. This new technique is a one-step process where the SiO_x deposition and evaporation of Au can be carried out in the same vacuum chamber, which in turn can reduce unnecessary contamination occurred during the removal of samples from vacuum chamber to DC sputter coater. First, SiO_x film with optimal flow rate ratio of 30 is deposited using PECVD system. Without taking out the samples, evaporation of Au onto the SiO_x surface using hot wire evaporation technique was carried out without using the shutter to control the evaporation time of Au. We observed the non-uniform size of Au particles with broader size distribution on the Au/SiO_x films annealed at 800 ^{o}C. The size of Au particles ranged from 40 to 500 nm. Therefore, we modified the system by assembling the shutter to control the evaporation time of Au and study the role of SiO_x in the growth of Au NPs. According to the result, it was widely accepted that SiO_x may act as a diffusion barrier for further Au nucleation. The weak Au-SiO_x chemical interactions also allow the study of Au NPs precisely by eliminating other unwanted factors exhibited by surrounding medium.

Finally, the effects of heated SiO_x film on the growth of Au NPs have been successfully studied. We observed the reduction of oxide characteristics during the Au evaporation process in vacuum conditions with further increase in substrate temperature from room temperature up to 300 ^{o}C. However, Si-O-Si characteristics become obvious after the thermal annealing process. Narrower size distribution of Au NPs was obtained after Au on SiO_x film prepared at 300 ^{o}C was further annealed at 200 ^{o}C in N_2 ambient with atmospheric pressure. Size of Au crystallites was measured at around 5.2 to 10.8 nm and 5.3 to 17.2 nm for as-deposited (300 ^{o}C) and annealed sample (300 ^{o}C), respectively. From optical spectra, we found that the FWHM of SPR peak become narrower as size of Au NPs increased or inter-particle distance of Au NPs increased due to broader size distribution.

5.2 Future Works

In future, the results of this work are potentially to be adopted in plasmonic solar cell application. This study is well-complement to the effort of researcher worldwide in the preparation of 2D nanostructured composite system in thin film technology. It is believed that with the appropriate synthesis design, 1-D metal dielectric nanocomposite film can also be achieved. By combining the intriguing properties exhibited by NWs and NPs, high quality advanced materials can be obtained. Yi-Jen Wu *et al.* had anticipated that future vertical nanoplasmonic devices made by plasmonic nanocavity can be achieved and optimized. His endeavor in the study of Au/Ga_2O_3 peapod nanowires *(Y.-J. Wu et al., 2010)* was become one of the dominant example of nanoplasmonic device. In addition, it has been reported that performance of organic photovoltaic device (OPVs) can be enhanced with Au NPs blended into the anodic buffer layer of the OPVs such as PEDOT: PSS *(J.-L. Wu et al., 2011).* However, effects of the size and shape of Au NPs on the performance of OPVs have yet to be explored and investigated in detail. It might be an advantage for us to adopt the results in this study into the findings of other researchers. On the other hand, thin film solar cell is speculated as a potential option to help in reducing the production cost of solar cell significantly. However, efficiencies of thin films solar cells are still low as compared to that of wafer-based silicon solar cells due to their poor light absorption *(Atwater, 2011).* Recently, S. Pillai *et al.* (2007) has reported that their group has found the NPs can be used to enhance the absorbance of silicon solar cell *(Pillai et al., 2007).* By taking consideration that major work in low dimensional materials research centre (LDMRC) under University of Malaya is a silicon- and carbon-based group, current study and effort in the processing of Au NPs have possibilities to be incorporated into the Si-based optoelectronic device to investigate the enhancement in electrical and optical performance.